UNIVERSITÀ DEGLI STUDI DI PADOVA

Dipartimento di Scienze Chimiche

Corso di Laurea Magistrale in Scienze dei Materiali

Mo-Based perovskites for an active proton conducting SOEC: a Carbon-Free approach to ammonia synthesis.

Relatore: Prof.ssa Antonella Glisenti

Controrelatore: Prof.ssa Chiara Maurizio

Laureando Matteo Giantin

Matricola 1220453

ANNO ACCADEMICO 2022/2023

1. INTRODUCTION

The United Nations Paris Agreement, a legally binding international treaty on climate change, aims to hold global warming well below 2 °C above pre-industrial levels and pursue efforts to limit warming to 1.5 °C. Leveraging artificial neural networks trained on climate model output[1], it has been possible through spatial pattern of historical temperature observations to predict the time until critical global warming threshold are reached. The predicted estimate for the 1.5°C global warming threshold is between 2033 and 2035.

This computed forecast it's just a data-driven approach to report the existing evidence of increasing risks to natural and human systems around the world.

In order to invert the trend of the long-term change in the average weather patterns it is necessary to act on human activities. Particularly it becomes a must the reduction of fossil fuel burning and demand, which increases heat-trapping greenhouse gas levels in Earth's atmosphere, causing land and ocean temperature increases; rising sea levels; ice loss at Earth's poles and in mountain glaciers as well as frequency and severity changes in extreme weather[2].

To achieve this fundamental step forward, the research of novel technologies and alternative methods to generate, transfer and convert power are needed and one of the paths that lead to this goal is the development of future society around new carbon-free, clean and renewable energy sources.

'Developing around' means that just researching a new fuel as energy source or a way to produce it, it's not really enough to rush into the future. Not only because fossil fuels are used to produce and power most of everyday items, but also because they became an important part of our society, with a production and distribution well established, and an availability which is taken for granted as well as an answer to every energetic request. Anyway the progress is made by a movement towards higher stages, a gradual and continuous transformation from good to better[3], so with the aim in mind it is necessary to take steps into the right path.

Renewable energy is produced from sources like the sun and wind that are naturally replenished and do not run out, in contrast with the fossil fuels like coal and oil that are extracted from finite sediments. The natural phenomena can be used as generators of electricity, heat and the main types of clean renewable energy that are getting a growing attention are bio, geothermal, marine, solar, wind and hydropower[4]. The attention gained is justified considering the multiple advantages provided by these sources, first of all they are spread equally worldwide, giving the possibility to every country to produce its own power in an environmentally friendly way, expanding the energy access even to the most remote ones. Letting anyone produce its own energy implies more job creation throughout renewable energy industries, making them affect also the economical and national aspects of a country.

As nothing is black or white, the main point in favour to non-renewable energy compared to the renewable one is the simplicity in storage because it is already in storage as extracted. Furthermore clean sources have discontinuity in power supply, for example the wind doesn't

blow always at the same speed and solar energy can be collected only during day time while not always at the same rate, so the storage problem in exponentially enhanced[5].

Considering these characteristic drawbacks, it becomes of primary importance to create a complementary system to work alongside the energy production, to effectively store the energy coming from the renewable sources. The nowadays most common and category spread energy harvesting device are lithium-ion batteries (LIBs). As world has grown to appreciate and depend on the power and convenience brought by these devices, their manufacturing and disposal have increasingly become a subject of political and environmental concern[6,7]. On the manufacturing side, depending on how the country commissioned for the battery production harvest energy, the greenhouse gas emissions for a battery pack can go up to 272 Kg CO_2 eq/kWh. This value is calculated considering the greenhouse gas emission intensity of electricity, that is determined per country, expressed as g CO_2 eq / kWh, which consider all potential primary energy sources for electricity generation, type of plant, conversion efficiencies and own electricity consumption in the power plant. The calculation considers all carbon equivalent emissions, associated with the combustion and supply of the fuels used for electricity production[8]. Taking into account LIBs components of electrical vehicle (EV), the International Energy Agency (IEA) estimates that the world currently has enough capacity to recycle 180,000 metric tons of dead EV batteries a year and that all of the EVs put on the road in 2019 will eventually generate 500,000 metric tons of battery waste[9]. These data are just a hint of how the current LIBs pathway does not seem like the only solution for an environmentally friendly future.

1.1 Alternative Pathways: Hydrogen and Ammonia

As an alternative to fossil energy sources, LIBs and as a new way to achieve carbon neutrality, hydrogen is considered one of the most promising fuels for the future[10]. Not as a primary source of energy but as energy vector, it can be produced from a wide range of technical process, both from renewable, biomass, and non-renewable, fossil fuels, sources. As downside not even the biomass methodology has a neutral carbon footprint, 0.670 g CO_2 eq / kWh are emitted to produce Hydrogen from a 2.53 x 10^6 Kg of biomass, because of the steam reforming endothermic equilibrium reaction, in which the hydrogen is obtained through a catalysed reaction between hydrocarbons and steam:

$$C_nH_m + nH_2O \leftrightarrows nCO + \left(n + \frac{1}{2m}\right)H_2 \quad (1\text{-}1)$$

Following this reforming process, the methane steam reforming is the most feasible, but it can be done also with Bio-Oils, Methanol, Ethanol and other basic hydrocarbons, that, depending on the availability, can be categorized with different hydrogen yields but will always be non-neutral in terms of carbon emissions.

There are also some carbon free processes that can be used, for example the Thermochemical Water Splitting, which consists in the complete decomposition of water. In a single step it can only be obtained at high temperatures (above 2000°C), while in multiple ones the temperatures can be significantly lowered involving the contribution of a metal oxide catalyst, a perovskite for example[11]. Considering again the drawback side of things, the energy needed to reach the target temperature is certainly a

major one, and none of the just described methodologies takes into account two hydrogen concerns, i.e., the storage and transportation.

Effective methods to store hydrogen are essential to enable its widespread utilization, particularly for industrial use where a constant feedstock input is required. As an elemental molecule its main problem is the low volumetric density, 0,0899 kg/m^3 in gas state, that can be enhanced by condensation in its liquid state, but the former solution requires a temperature of -253 °C and allows to reach a density of 70 kg/m^3, a fifteenth of water's one. Not even the compression seems like a valuable solution, it allows only lower densities (7-27 kg/m^3) and considering the sensitiveness of H_2 to detonation can result in a dangerous approach to the storage problem. The combination of this two solutions, the cryogenic gas tank, able to store twice the hydrogen than the single applications, has recently been used in a BMW prototype[12], but it present some problems in hydrogen losses in the car ambient and uncontrolled evaporation of the liquid H_2.

To overcome the presented problems several carbon free chemicals containing hydrogen in good amounts have been considered, among which the most prominent ones are water and ammonia.

The choice of ammonia as a possible hydrogen vector is defined according to its physical and chemical characteristics: one mole of NH_3 contains 1.5 mol of H_2 which is 17.8 % by weight, in density terms is 108 kg/m^3 of hydrogen in liquid ammonia at 20 °C and 8.6 bars[13], a value four times higher than the one for pressurized hydrogen, and better in density as well as in more favourable conditions than the cryogenic ones for liquid hydrogen. Further comparison with liquid hydrogen showed that it has some remarkable advantages, making it closer to gasoline from the point of view of a transportation fuel. For example, has a valid octane rate (110-130)

so it can withstand high compression in combustion engines without detonating, it's safer than other fuels because it can be detected by nose in concentrations around 5 ppm and has a narrow flammability range therefore its generally considered non-flammable presenting no explosion danger when properly transported. The comparison with different fuels is summarized in *Table 1*[13–19].

	Pressure [atm]	Temperature [°C]	Heating Value [MJ/kg]	Energy density [GJ/m3]	Specific energetic cost [$/GJ]
Gasoline	1	25 °C	44.34	30.93	29.1
Ethanol	1	25 °C	26.84	21.07	15-20
Methanol	1	25 °C	19.90	15.61	37.5
Lithium-Ion Batteries	1	25 °C	0.72	1.08	151
H_2 compressed and gasfied	300	25 °C		2.46	28.2
H_2 Cooled and liquefied	1	-253 °C	120	8.5	
NH_3 compressed and liquefied	300	25 °C		11.65	13.3
NH_3 cooled and liquefied	1	-33 °C	18.6	12.69	

Table 1-1 list of fuels and their properties [13–19]

As expected, the mean better values are assigned to gasoline in terms of storage conditions compared to energetic values, hydrogen stands up in energy vs weight table because is the lightest molecule on earth. On the other side ammonia has the lowest LHV (Lower Heating Value, Mj/kg), comparable to alcohols, which introduce its main practical issues of poor

ignition quality and low flame speed, about an order of magnitude lower with respect to conventional fuels and alcohol. Another downgrading aspect that must be considered dealing with ammonia combustion is the strong polarity of ammonia that significantly affects its oxidation kinetics[16]. Reason why oxidative conditions can lead to another possible drawback of ammonia: the emission of NO_x fuels.

This possibility must be taken into account not only dealing with ammonia in its fuel usage, but also during its synthetic pathway.

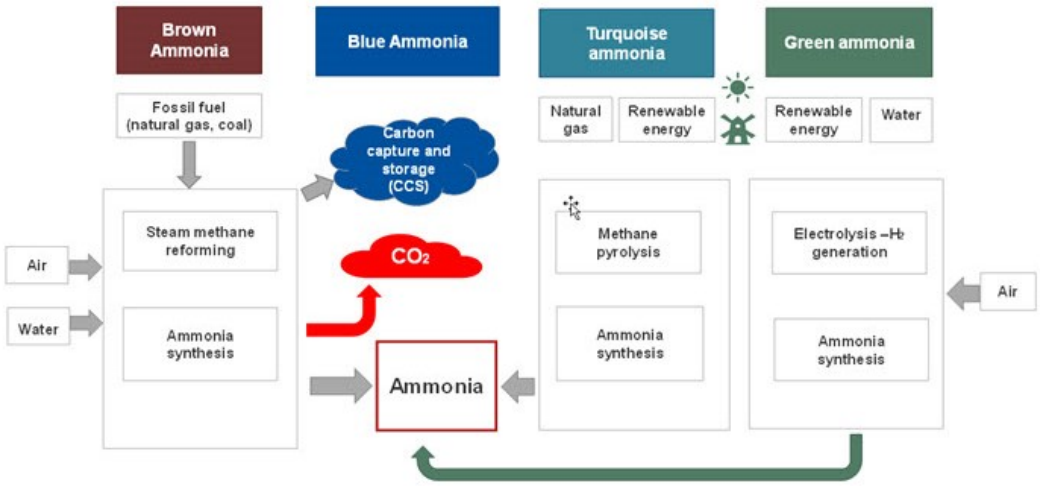

Figure 1-1 Synthetic pathways of ammonia, categorising it by colours.

As shown in *Figure 1* there are multiple ways to obtain ammonia, but the two colours that contains 90% of the nowadays production are *brown* and in low case percentage *blue*. The technique providing these two colours is the Haber-Bosch, a high energy consumption (over 30 GJ per ton of NH_3) and high greenhouse gas emission (2.16 kg CO_2 eq per kg NH_3) method. Even though this process was a life changing discovery in 1910, leading to the ammonia production from atmospheric nitrogen (N_2) by a reaction with hydrogen (H_2) using an iron metal catalyst under high temperatures and pressures, it needs to be exchanged with something else to support the

future of our planet; a new pathway that leads to the production of *green* ammonia.

Considering ammonia to be a promising fuel for sustainable energy conversion and storage, alongside the nowadays demand of it as fertilizer and chemical reagent, the necessity to have a *green* way to produce ammonia is what has been researched in this master thesis work.

The main challenges to overcome in ammonia synthesis to describe it as a *green* product are to make sure that no NO_x can affects the synthetic process and to perform a completely carbon-free process. The solution of choice to solve them both is through a proton conducting Solid Oxide Electrolytic Cell (H-SOEC), researching on an electrode material capable to work in reversible ways to design a symmetric and stable device.

1.2 Fuel and Electrolysis Cells Overview

Fuel Cells (FCs) are electrochemical devices that convert chemical energy contained in the fuel into electrical energy, with high efficiency, long-term stability, fuel flexibility and low environmental impact[20]. Electrolysis Cells (ECs) vice versa convert electrical energy into chemical one to provide it in the formation of a less thermodynamically stable molecule.

Several different types of FCs and ECs have been developed through years, all of them composed of two electrodes divided by an electrolyte. The two electrodes, cathode and anode, can be named also oxygen and fuel electrode in FC mode, and vice versa in EC respectively. The devices are generally divided into five major categories, *Table 1.2*[21–24], split up according to electrolyte physical states and material types. The former one is the

material responsible for the ionic transfer (charge carrier) between the two electrodes and must be electron insulating to avoid possible unwanted short circuits inside the device. As it is shown in *Table 1-2* molten carbonate fuel cells are assumed as insufficient in electrolysis because in this mode CO_2 is involved in the cathode reaction, which implies CO_2 must be added to oxygen electrode and transfer as carbonate through the electrolyte, increasing the complexity of the system and possibly leading to lower overall efficiency[21].

Abbreviation	Name	Electrolyte
PEMFC/PEMEC	Polymer/Proton Electrolyte Membrane Cell	Semipermeable membrane to protons (H^+) but impermeable to gasses to avoid short circuit.
PAFC/PAEC	Phosphoric Acid Cell	Highly concentrated or pure liquid phosphoric acid (H_3PO_4) saturated in SiC matrix, transfer H^+.
AFC/AEC	Alkaline Cell	Porous matrix saturated with aqueous alkaline solution (e.g., KOH), transfer OH^-.
MCFC	Molten Carbonate Cell	Liquid sodium and potassium carbonate supported by ceramic matrix (e.g., $LiAlO_2$), transfer CO_3^{2-}.
SOFC/SOEC	Solid Oxide Cell	Solid oxide ceramic material that conducts ions of choice (e.g., OH^- or H^+) must have very low electronic conductivity.

Table 1-2 Summary of most studied fuel cells divided by electrolyte materials[21–24].

Depending on the operating mode and the type of ion that has been designed as charge carrier, anode and cathode are subject to different reactions[25,26]:

Fuel Cell

Anode	Cathode
$H_2 \rightarrow 2H^+ + 2e^-$	$O_2 + 4H^+ + 4e^- \rightarrow 2H_2O$
$H_2 + O^{2-} \rightarrow H_2O + 2e^-$	$O_2 + 4e^- \rightarrow 2O^{2-}$
$2NH_3 \rightarrow N_2 + 6H^+ + 6e^-$	

Electrolysis Cell

Anode	Cathode
$2H_2O \rightarrow O_2 + 4H^+ + 4e^-$	$2H^+ + 2e^- \rightarrow H_2$
$2O^{2-} \rightarrow O_2 + 4e^-$	$H_2O + 2e^- \rightarrow H_2 + O^{2-}$
$H_2 \rightarrow 2H^+ + 2e^-$	$N_2 + 6H^+ + 6e^- \rightarrow 2NH_3$

These reactions occur respectively at anode and cathode of devices in *Table 1-2*, but in each one in different conditions. PEMC, PAC and AC work at an operative temperature between 40 and 220°C both in fuel and electrolysis mode where the alkaline ones are the mostly used and more commercially available in this range of temperatures. However, is generally considered that in this range of application polymer electrolyte membrane cells are more likely to succeed in achieving widespread commercial application, because AFC require a source of very pure hydrogen as fuel and the nature of the electrolyte is corrosive. The drawback with low temperature devices is much more noticeable in electrolysis because in order to achieve acceptable production rates, even with the more studied and thermodynamically easier hydrogen synthesis, high voltages are needed causing heat production despite the endothermic process.

Depending on the researched product, increasing the temperatures causes the increment also in production rates, to the point where the cell can be considered self-cooled, being the process endothermic, even at lower voltage values. This happens because in most electrolysis reactions the equilibrium shift toward the right side of the equation at higher temperatures, but a minimum voltage is required: the so-called reversible voltage, E_{rev}, which is determined by the Gibbs free energy, thereby a function of both temperature and pressure[21], better analysed in the next chapter of this work.

Solid oxide cells are suited to work at higher temperatures and on alternative fuels in a reversible way using an inorganic solid oxide as electrolyte, reason why those are subject of this work and will be described in detail from paragraph 1.4.

1.3 ECs and FCs Thermodynamics[21,26,27]

1.3.1 ECs Thermodynamics

In the examination of thermodynamics, the device is assumed to be ideal, so a reversible one where anode and cathode are separated by the electrolyte without side reactions, short circuits, etc.

Taking as example the electrolysis of H_2O (*Figure 1-2*[28]), the process becomes increasingly heat consuming with temperature increase. This total energy demand can be provided for the most by heat at high temperatures, allowing the possibility to use the Joule heat, the heat produced by an electric current which passes through a conductor, thanks to the internal resistance of the device.

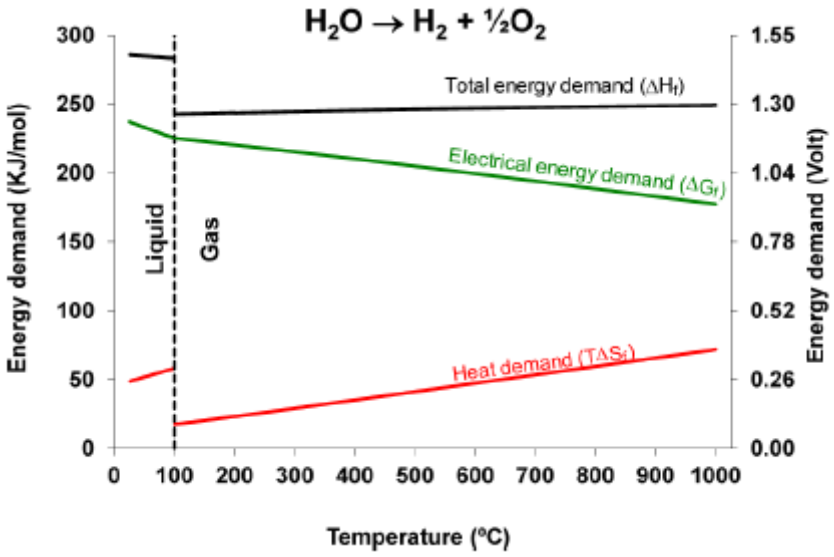

Figure 1-2 Thermodynamics of H_2O electrolysis atmospheric pressure[28].

The total energy demand for the process is related to the product enthalpy of formation, in this model case H_2O, which can be divided into the two energies provided by the device:

$$\Delta H_f = \Delta G_f + T\Delta S_f$$

(1-2)

Where ΔG_f is the fraction of electrical energy and $T\Delta S_f$ the fraction of heat energy. Being the process endothermic the device will self-cool, compromising the performances, if no heat is supplied. The change in enthalpy during the electrolysis process, in an isothermal transition, is proportional to the value of thermoneutral voltage E_{tn}:

$$E_{tn} = \frac{1}{nF}\Delta H_f$$

(1-3)

Where n is the number of electron involved in the process (in this case 2) and F is the Faraday constant (96485 C/mol). For example, at 25°C the E_{tn} value is 1.48, but in SOFC range temperature for an oxide ion conducting electrolyte, 850°C, it decreases to 1.29 V. These are just standard values

reported to provide an order of magnitude while real values have to be calculated for every local condition, even though the overall reversible thermodynamics remains the same.

The theoretical value of the electromotive force E_{rev} (or minimum voltage required for splitting the molecule) is expressed by the Nernst equation, which provides a relationship between the standard potential E^{θ}_{rev} (also described as OCV: Open Circuit Voltage) at the variation of partial pressures of reactant and products. The former ones define the reaction coefficient Q which at standard conditions is equal to 1 for all reactants and products. The complete Nernst equation is:

$$E_{rev} = \frac{1}{nF}\Delta G_f^{\theta} - \frac{1}{nF}\ln Q$$

(1-4)

With:

$$E_{rev}^{\theta} = \frac{1}{nF}\Delta G_f^{\theta}$$

(1-5)

Where ΔG_f^{θ} is the standard Gibbs free formation energy and, as expected, if in standard conditions $E_{rev}=E^{\theta}_{rev}$. As seen in *Figure 1-2* working at high temperatures reduces substantially the reversible potential, furthermore in SOCs devices it slightly increases the impinging frequency (related to the chance of for collision of gas with electrochemically active sites of electrode) and also the ionic conductivity. The impinging frequency could be further improved working in pressurised devices which is not the case of this work but can be a starting point for further improvement. In any case higher temperatures increase the overall cell kinetics[29].

1.3.2 ECs Efficiency[21,30,31]

According to literature there are two ways to define the efficiency of an electrolysis cell. The first one is based on the LHV, so the low heating value, which if a lossless process is considered can only reach the maximum of 85%. This description is mostly considered inadequate since theoretical lossless operation are awarded with the 100% efficiency.

The other one is based on the amount of energy needed to split the reactants, so on the higher heating value (HHV), or, as presented in the previous paragraph, the standard formation enthalpy. This thermodynamic value is divided by the energy consumption of the device W, consisting of both electrical and heat contribution, used to produce one mole of the product.

$$\eta = \frac{HHV}{W} = \frac{HHV}{electricity + heat + loss} = \frac{HHV}{UnF + heat + loss}$$

(1-6)

Once defined U as the cell voltage, considering inputting all the needed heat throughout the Joule effect so by the applied potential, is possible to exclude the heat variable from the equation. To do so it is necessary to work at values above the thermoneutral potential E_{tn} and *eq. 1-6* can be rewritten as follow:

$$\eta_{at\ or\ above\ E_{tn}} = \frac{\Delta H_f^\theta}{UnF + loss} = \frac{E_{tn}^\theta nF}{UnF + loss} = \frac{E_{tn}^\theta}{U + L'}$$

(1-7)

$$L' = \frac{loss}{nF}$$

(1-8)

This description implies that once applying the thermoneutral potential it is a matter of cell design defining a cell as lossless or not.

Avoiding electrical, heat and gas leaks through the cell means the theoretical capability of working close to 100% efficiency. In practice, SOECs have been shown as devices that operate at electrical efficiencies exceeding 95%[32].

As shown the description does not consider any conversion efficiency of gasses because a cost-efficient synthesis gas production is usually to consider more important that the higher conversion rates. For example, the already mentioned alkaline cells nowadays have an efficiency of 78-87% in order to optimise the production economy rather than the production efficiency.

1.3.3 FCs Efficiency[26,27,33]

Even though this project is focused on ammonia synthesis, its necessary to give a description of fuel cell mode efficiency for a better understanding of a possible reversible device.

In this case the thermodynamical efficiency is defined as the reversible Gibbs free energy over the reversible enthalpy of the chemical reaction, so strongly dependent on the working temperature.

$$\eta_G = \frac{\Delta G_r}{\Delta H_r}$$

(1-9)

On the other hand, since in this case the electrical efficiency is measured in conversion from chemical to electrical energy:

$$\eta_V = \frac{V}{\Delta E_{rev}}$$

(1-10)

Where V is the voltage obtained experimentally and comes out from the difference between the electromotive force (see *eq. 1-4*) and the product between the intensity current I and the total resistance R_{tot}:

$$V = \Delta R_{rev} - R_{tot} I$$

(1-11)

With R_{tot} being the sum of all resistances in the cell: R_o or the ohmic resistance and R_j a term that takes into account other factors such as polarization and electronic transfer. If the former term is negligible with respect to the ohmic resistance (if $R_0 \gg R_j$), the voltage efficiency can be rewritten as:

$$\eta_V = 1 - \frac{R_0 I}{\Delta E_{rev}}$$

(1-12)

In reversible conditions, the only energy loss by the system is the heat loss towards the environment due to the negative entropy ($T\Delta S$). To have this condition the work produced when the fuel cell supplies an electric current I is:

$$W = EI$$

(1-13)

In this case the cell potential and its related efficiency decreases in increasing of current as a consequence of the following phenomena:

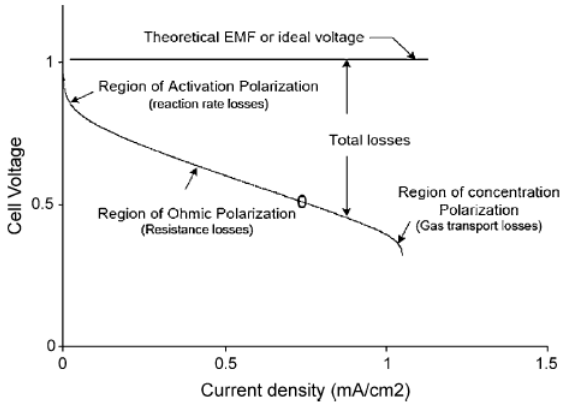

Figure 1-3 typical fuel cell polarization curve.

- Activation polarization E_λ^{act}: at low current level the ohmic loss becomes less significant whereas the increase in output voltage is due to the mixed potential at electrodes, generated by chemical reactions. This is the reason why measured OCV are lower than actual reversible voltage (E_{rev}).
- Ohmic polarization E_λ^{ohm}: the linear region in which as the current density increases the voltage drops due to the ohmic nature.
- Concentration polarization E_λ^{conc}: at very high current densities the voltage falls significantly because of gas exchange efficiency.
- Nernst loss E_λ^{Nernst}: mass transport losses, due to non-reacting diffusion in the gas diffusion layer and to reacting diffusion at the electrode layers.

The resultant total loss can be obtained by the following relation:

$$E_\lambda = E_\lambda^{act} + E_\lambda^{ohm} + E_\lambda^{conc} + E_\lambda^{Nernst}$$

(1-14)

So, the performance of a fuel cell can be optimised thermodynamically and electrically. The fuel processing, management and the temperature control, influence the thermodynamical efficiency. Electrical efficiency depends on the various losses over the cell in general.

Even if there exist losses and dissipation so that a completely reversible process from fuel cell to electrolysis one is still a long way to go, the single mode devices have high efficiency, as previously described, and the solid oxide itself is suitable for reversibility operations in SOFC and SOEC mode.

1.4 Solid Oxide Electrolysis Cells

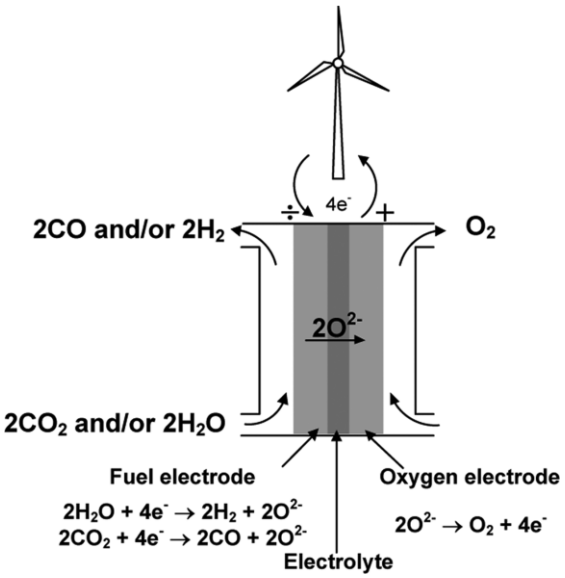

Figure 1-4 Working principle of a solid oxide electrolysis cell (SOEC).

The research over solid oxide cells began on the fuel cell mode, but in the early 1980s the reversibility of the process for this type of devices was demonstrated for both H_2O and CO_2[34]. Initially a slightly lower performance was observed in electrolysis mode and the difference was stated to be in the slower diffusion of H_2O over H_2, but a more recent study suggested that the lower performances can be caused by an increase conversion resistance in electrolysis mode as well as a local temperature decrease due to the endothermic nature of the process[35]. As described before, nowadays SOEC can achieve technical efficiencies of 100% thanks to advantageous thermodynamics reaction and kinetics. The principle of steam electrolysis consists of H_2O electrochemically reduced to H_2 at the negatively charged fuel electrode, leaving as a product a flow of oxide ions through the electrolyte and to the positive charged electrode where they will be oxidized to molecular oxygen in an oxygen ion-conducting electrolysis cell.

1.4.1 SOECs Configuration and Designs

The cells configuration and design where initially mainly tubular (*Figure 1-5*), later improved as microtubular, but, even if this kind of design is still performed, nowadays the majority of SOECs reported are planar. The reason for this change is to optimize production costs, current densities and fuel distribution, giving up a few in terms of mechanical stability, quick start-up capability, and improved thermal cycling[36]. The challenges of planar cells extend when considering sealing requirement and contact issues. Reason why different designs, based on the supportive component of the device, are researched and industrially manufactured (*Figure 1-5*):

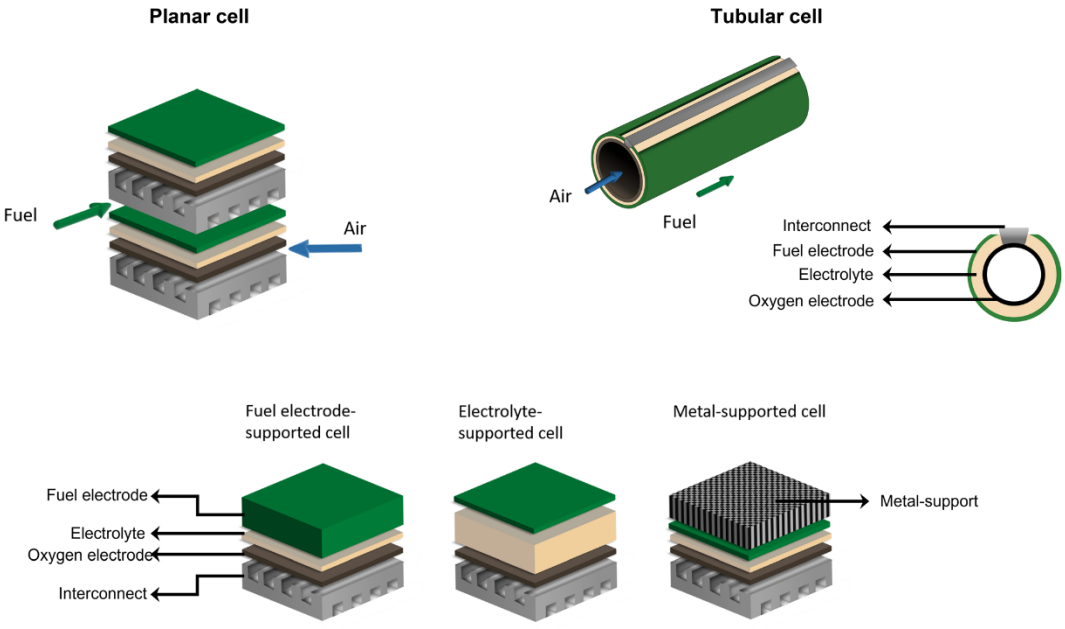

Figure 1-5 Planar and tubular cell designs with schematic representation of the three different support types[36].

- Electrolyte-supported cells: the design subject of this work. Characterized by an electrolyte thickness higher than electrodes. Typical values from literature are around 50-250 μm (increased to 1000 μm in this work for setup necessities) for the

electrolyte layer and 5-80 μm for electrodes. The benefits of this design come in a mechanical way, resulting in a better robustness and an already active production in industrial scale. On the other hand, the drawbacks are the higher ohmic resistances, which leads to lower power densities, and higher operative temperature, features that reflects also on the materials of choice.

- Electrode-supported: in this case the thicker layer is the porous electrode allowing a further distinction on fuel (cathode in SOEC) and oxygen (anode in SOEC) electrode. This design allows to reduce significantly the electrolyte layer to 2-20 μm, whereas the supportive layer goes from 250 to 1000 μm and the other electrode from 5 to 80 μm. This option allows much lower ohmic resistances so the possibility to work even at lower temperatures. The drawback of this design is the lower redox stability, resulting in higher sensitivity for damage caused by the redox cycle[37].
- Metal-supported cell[38]: this design is used to keep all the solid oxide thicknesses of the device as small as possible, attaching both electrodes with the electrolyte in between on a metallic support of ~1000 μm. This design is reported to be the best in terms of performance, allowing the other designs' advantages and neglecting the disadvantages, adding better performance even in mixed gas compositions. The possible drawbacks are the complex operating conditions, for example gas distribution, and more challenging adherence between components. This

type of devices is commercial in SOFC mode but still in development in SOEC[36].

1.4.2 SOECs Components[21,36]

This section provides a description of the three SOEC's components working principle and brief considerations over the effective materials state-of-art that will be better introduced in the proton-conductive SOECs paragraph.

ELECTROLYTE

Electrolyte is the component that separates the two electrodes, reason why it must be stable in both oxidizing and reducing conditions. Density wise it has to be as thigh as possible to prevent reactant from both sides to mix, allowing better ion conductivity at the operating temperature. Another fundamental quality is a negligible electric conductivity to avoid current leakage and short circuits inside the cell. All these characteristics depend on temperatures, material properties and thickness. The cell design can influence the material choice regarding thermal expansion properties, for example a stable material in wide temperature range prevents delamination of the device.

The state-of-art materials choice in case of an oxide ions conduction are the stabilized zirconia, for example 3YSZ (3% mol-partially stabilized) or scandia-ceria-stabilized ScCeSZ are typically used for their mechanical stability in electrolyte based SOECs. In the other configurations 8YSZ (8% mol) is the materials of choice because exhibits numerous vacant interstitial

sites for better ion conductivity. In any case electrolyte materials are still in research and development phase.

OXYGEN ELECTRODE

Generally higher degradation has been observed for SOEC compared to SOFC operation due to the different oxygen activity, defined as Oxygen Evolution Reaction (OER) for SOEC and Oxygen Reduction Reaction (ORR) for SOFC.

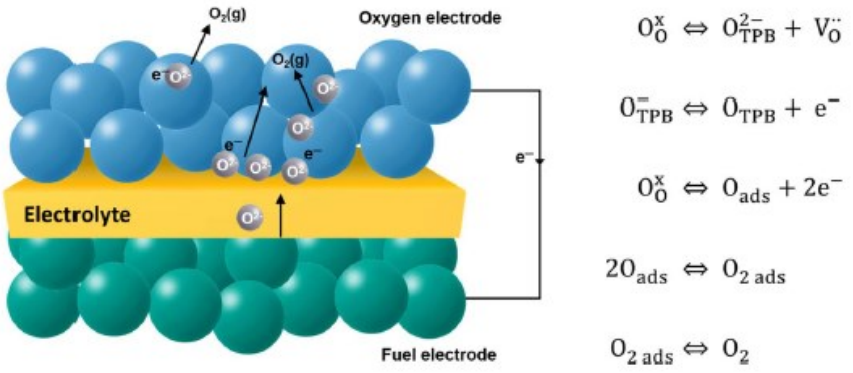

Figure 1-6 Schematic description of the oxygen evolution reaction (OER)[36].

The differences are due to the larger pO_2 gradient which requires the oxygen electrode to meet several criteria in electrolysis mode, such as an excellent catalytic activity for the oxygen evolution and a high chemical stability in an oxidizing environment, without the formation of resistive phases with the electrolyte. Regarding the activity and stability of the electrode, they are considered in the following description for O_2, keeping the focus on the hydrolysis reaction, but are to be considered on the inlet reactant at the specific electrode.

In *Figure 1-6* the OER is schematically represented. Following the reaction, the oxygen ion has to be first received at the TPB from where it will be exchanged between electrolyte-electrode surfaces and the charge

transfer process happens. Then the removed electron must follow the applied circuit and two half oxygen molecules, still adsorbed on the porous electrolyte, must be transported through the bulk and recombine in molecular oxygen as gas. The just mentioned Triple-phase boundary (TPB) is the reaction site of fuel cells, and the name derives from the three phases that must be in contact: ceramic, metal and reactant (gas). Consequently, there are three requirements that need to be met in this area: catalytic activity by the metal, ionic conductivity by the ceramic material, and the electrical conductivity to collect and transfer electrons to the external circuit.

A model proposed to calculate the chemical reaction contribution[39] (or chemical resistance) R_{chem} consider, among processes of OER, that two are to be considered rate-limiting steps: the surface exchange, determined by the surface exchange coefficient (k^*), and the surface transport, determined by the oxygen self-diffusion coefficient (D^*). These two parameters are in relation with microstructural parameters, such as tortuosity (τ), porosity (ε) and oxygen surface concentration (C). Taking into account the charge transfer resistance these processes represent the total impedance that can be measured from the device, according to:

$$Z = R_{electrolyte} + z_{interface} + z_{chem} \quad (1\text{-}15)$$

When the surface exchange and solid-state diffusion dominate, the total cell impedance can be rewritten as

$$Z = R_{chem} \quad (1\text{-}16)$$

$$R_{chem} = \frac{RT}{2F^2}\sqrt{\frac{\tau}{(1-\varepsilon)aC^2k^*D^*}} \quad (1\text{-}17)$$

Where F is the Faraday constant and T is temperature; relation describing the resistance of this process as directly proportional to the temperature and optimised with better exchange/diffusion coefficients and electrode porosity. The exchange parameter is influenced by the compatibility of electrode with the other cell component materials.

High chemical stability and ionic conductivity under oxidizing conditions, in case of hydrolysis, are needed to ensure good oxygen ion transport through the electrode as well as high conversion rate, resulting in low ohmic cell resistance. More generally, the materials used in this component can be divided in n-type and p-type conductors. For hydrolysis in oxide ions conduction the p-type are the suited ones because the oxygen excess is required to generates holes. On the other hand, an n-type conductor is not stable in oxidizing condition because it requires oxygen deficiency to create electrons[40].

To match all this conductibility requirements MIEC (Mixed Ionic-Electronic Conducting) single-phase perovskite oxides have increasingly become a field of study. These materials present advantageous properties improving the rate limiting steps of the reaction supported by the electrode, so a faster ion diffusion and improved surface exchange kinetics, due to the extension of the TPB to the whole material surface being every molecule a metal ceramic oxide. The specific description of these materials is provided in chapter 2 of this work. Device wise, being the TPB extended, the parameters defining the component chemical resistance must be added with the electrode thickness, or more specifically the penetration depth *d*: a parameter that considers thickness respectfully of the volume-specific area.

The state-of-art materials for oxide ions conductive SOECs are perovskites ((a) in *Figure 1-8*) LSCF and LSC (respectively

$La_{1-x}Sr_xCo_{1-y}Fe_yO_{3-\delta}$ and $La_{1-x}Sr_xCoO_{3-\delta}$) which exhibit good performances and durability in SOEC applications at high temperatures. Newer perovskites-based materials currently researched are double perovskites (b) e.g., $Sr_2Fe_{1.5}Mo_{0.5}O_{6-\delta}$, as well as Ruddlesden-Popper phases (c) such as $La_2NiO_{4+\delta}$ or $Sr_2RuO_{4+\delta}$. Being still under investigation, no long-term measurements have been recorded, but Ruddlesden-Popper phases of lower order present a decomposition issue at temperatures over 600°C, despite the good catalytic activity.

FUEL ELECTRODE

The fuel electrode, as the oxygen one, must fulfil several requirements to achieve sufficient performances. The theoretical description and requirements are the same of oxygen electrode; so high chemical and thermomechanical stability, made of catalytic active materials, with good ionic and electronic conductivity. In this case what change is the reaction environment and the reaction itself that this component must meet (*Figure 1-7*).

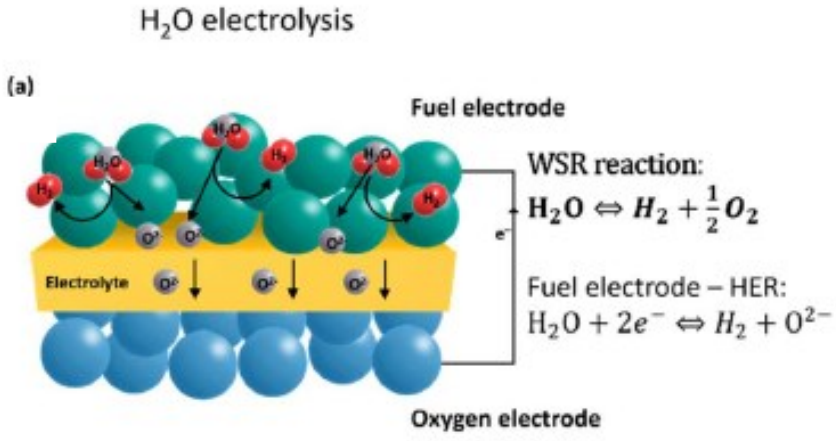

Figure 1-7 Schematic description of the water splitting reaction (WSR)[36].

Continuing the description with hydrolysis, the water splitting reaction (WSR) into half molecule of oxygen and hydrogen has to be catalysed by the active materials inside this component, in which the hydrogen evolution reaction (HER) is included.

The environment of stability is a humid/mixed gas ambient depending on researched electrolysis, so there can be fractions of reducing agents H_2 as well as carbon-containing molecules if carbon dioxide electrolysis is researched.

The state-of-art materials for the fuel electrode in SOECs are cermets, so Ni-YSZ or Ni-GDC, generally produced by wet impregnation or infiltration, which exhibits sufficient performance and stability. The drawback of these materials is the agglomeration/coarsening and migration of Ni, which leads to progressive lower catalytic activity due to the reduction of active TBP sites, being cermets non MIEC.

To overcome challenges of longevity and cost, new perovskites (MIEC) fuel electrodes are researched both in single and double perovskite configuration, such as $La_{0.75}Sr_{0.25}Cr_{0.5}Mn_{0.5}O_{3-\delta}$ (LSCM), $La_{0.2}Sr_{0.8}TiO_{3+\delta}$ (LST) and double perovskites as $Sr_2Fe_{1.5}Mo_{0.5}O_{6-\delta}$[36].

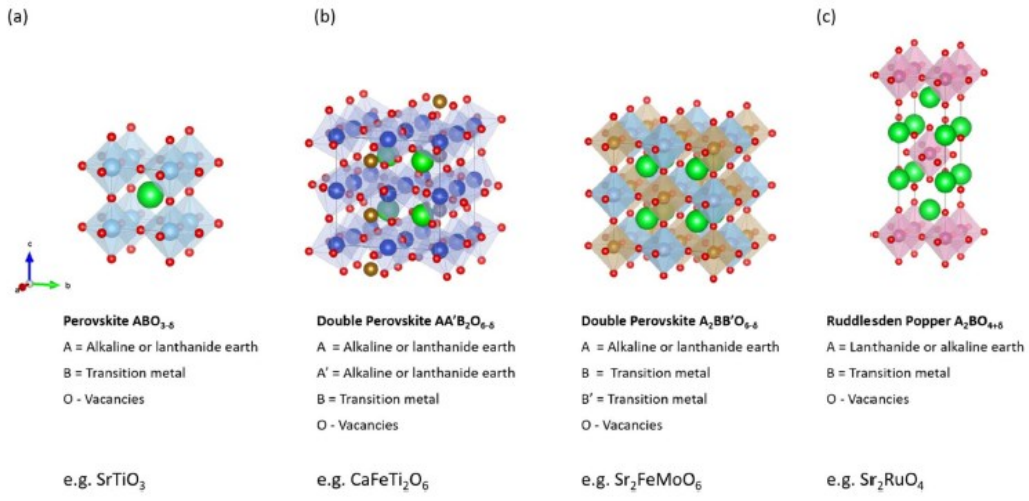

Figure 1-8 Materials researched for oxygen and fuel electrode[36].

1.5 Proton Conducting SOEC[21,41,42]

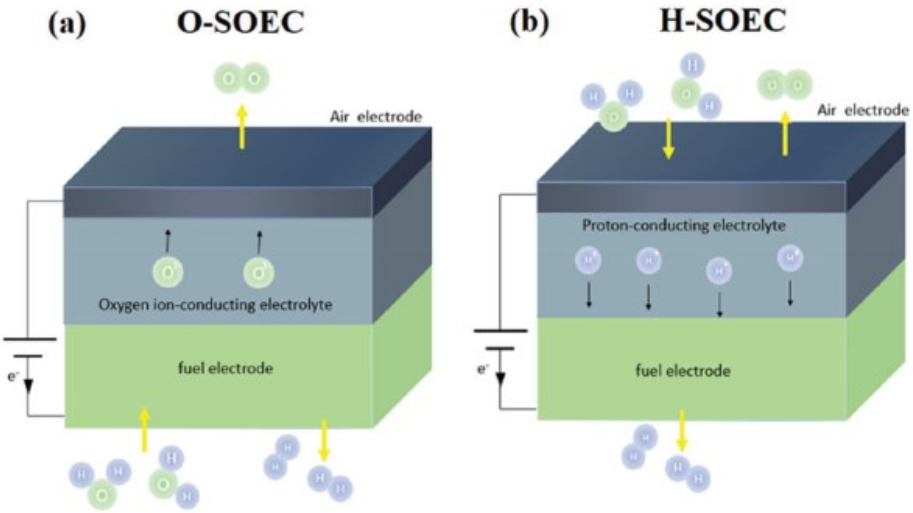

Figure 1-9 Schematic of oxygen ion conducting SOEC (a) and proton conducting SOEC (b)[42].

In *Figure 1-9* a difference between the O-SOEC (a) and H-SOEC (b) is displayed. The main difference between the two configurations stands in the conducted ion, which result in differences not only in working principle, but also in necessities of design and configuration of the cell.

As displayed ions migration in H-SOEC goes from the air (oxygen) electrode to the fuel electrode if the same voltage is applied, this results in one of the major advantages of this different configuration: the gas separation. With H-SOECs is possible to achieve high purity synthesis of dry hydrogen, methane or ammonia at the fuel electrode side of the device, allowing the material choice in a bigger range due to less restrictive stability necessities.

Another advantage of H-SOECs is the lower activation temperature of the conductive process, already at ~400°C the protonic ions conductivity is activated, resulting in mitigation of material degradation and better temperature choices respectively the product researched.

The third concept that make this type of device more suitable for future perspective is the concept of reversibility, that can be achieved just applying potential values higher than the open circuit potential (OCP) to work in electrolysis mode and lower to switch to the fuel cell one. The whole device can be so called R-SOC, reversible SOC. This consideration is also supported by the configuration choice of the planar cell that for H^+ conduction is better, both in SOFC and SOEC mode, if the device design is fuel electrode supported, rather than O^- conduction that requires opposite designs to reach the best results.

As said, in this case reactant at the electrode environment are different and so the materials, particularly the electrolyte, requires a permeability to only protons, without impurities of oxygen ions or electronic conductions. The development of this high temperature proton-conducting materials sees as the most intensively studied ABO_3 perovskites oxides (A= Ba, Sr; B=Ce, Zr), where the protonic peculiarity is reached thanks to a Y-doping (generally between 10 and 20%wt) in the B site of the structure, because the substitution of a tetravalent atom with a trivalent one.

$$Y_2O_3 \rightarrow 2Y'_{Ce} + 3O_o^X + V_o^{\cdot\cdot}$$

(1-18)

$$H_2O + V_O^{\cdot\cdot} + O_o^X \Leftrightarrow 2OH^{\cdot}$$

(1-19)

Considering Y-doped $BaCeO_3$: every two yttrium atoms an oxygen vacancy is generated where a water molecule can be adsorbed and form protons that binds to oxygen ions as hydroxide defects. These protons now bonded to the perovskite structure, can hop between oxygen atoms breaking and forming new bonds. For this reason, a water rich environment is beneficial.

Barium rather than strontium in the A site of the perovskite structure showed better protonic conductivity and sinterability, but lower stability in high H_2O-containing conditions, reason why $BaZrO_3$-based oxides are researched and proven to be more chemically stable but with lower sinterability and higher grain boundary resistance. To meet all the requirements the most common strategy adopted are $BaCe_{1-x}Zr_xO_{3-\delta}$ solid solutions, even if it just partially solve the problem of high-water-percentage stability[43]. For this reason, the best improvements in nowadays H-SOEC electrolyte materials are made on the manufacturing side of the problem, for example with thin films applications.

Electrodes on the other hand needs to respect the same theoretical conditions as in O-SOEC, so chemical stability and compatibility with the electrolyte material. Moreover, a good catalytic activity and minimal polarization resistances to maximize performances, alongside good ionic and electronic conductivity.

The similar requirements result also in similar materials researched, it's not yet possible to define state of art materials because proton conductive solid oxide cells are not commercially available. The aim for electrodes is the definition of cermets, single-phase perovskites (ABO_3), double perovskites ($AA'BB'O_6$) or Ruddlesden-Popper structures ($A_{n+1}B_nO_{3n+1}$) that match all the just presented necessities. For example, at the air electrode (oxygen in O-SOEC) $Ba_{0.5}Sr_{0.5}Co_{0.8}Fe_{0.2}O_{3-\delta}$ shows good catalytic activity but decomposes after heat-treatment in H_2O-Air. Instead at the fuel electrode Ni-based composite cermets can meet the requirements of H-SOEC, generally obtained through infiltration or wet impregnation, and the micro structurization is researched for further optimization as well as the previously defined materials.

1.6 Ammonia Synthesis in H-SOEC

As discussed in the *Alternative pathways* subchapter, the Haber-Bosch process is the predominant route for nowadays ammonia synthesis. Among the new researched processes, the electrochemical one benefits of zero emission of carbon dioxide, mild operating conditions and the capability to store renewable electricity in chemical bonds[44].

The process in a solid oxide proton conducting electrolysis cell takes place at the cathode side of the device (fuel electrode):

$$N_2 + 6H^+ + 6e^- \rightarrow 2NH_3$$

(1-20)

Where the nitrogen reduction reaction (NRR) has to compete with the hydrogen evolution reaction (HER):

$$2H^+ + 2e^- \rightarrow H_2$$

(1-21)

While on the anode side of the device the following reaction provides the protons to the device ($H_2(g)$ serves to express the reducing environment):

$$3H_2O + H_2(g) \rightarrow 6H^+ + O_2 + 6e^- + H_2(g)$$

(1-22)

The challenges facing electrochemical NRR mainly come from the two following aspects. Firstly, N_2 high bonding energy, high ionization potential and ultralow solubility in water that limit the reaction both thermodynamically and kinetically. Secondly the already mentioned competition between NRR and HER, which can both occur from a thermodynamic point of view having similar equilibrium potential, but kinetically ammonia formation is strongly disadvantaged. These difficulties

triggers the research of new catalyst materials and innovative configuration of the electrolytic cell[44,45].

The NRR is generally described as a three steps process:

(1) Adsorption of N_2 on the catalyst (2) Dissociative or associative breaking of nitrogen-nitrogen triple bond (*Figure 1-10*) with consequent hydrogenation (3) Desorption of the generated ammonia.

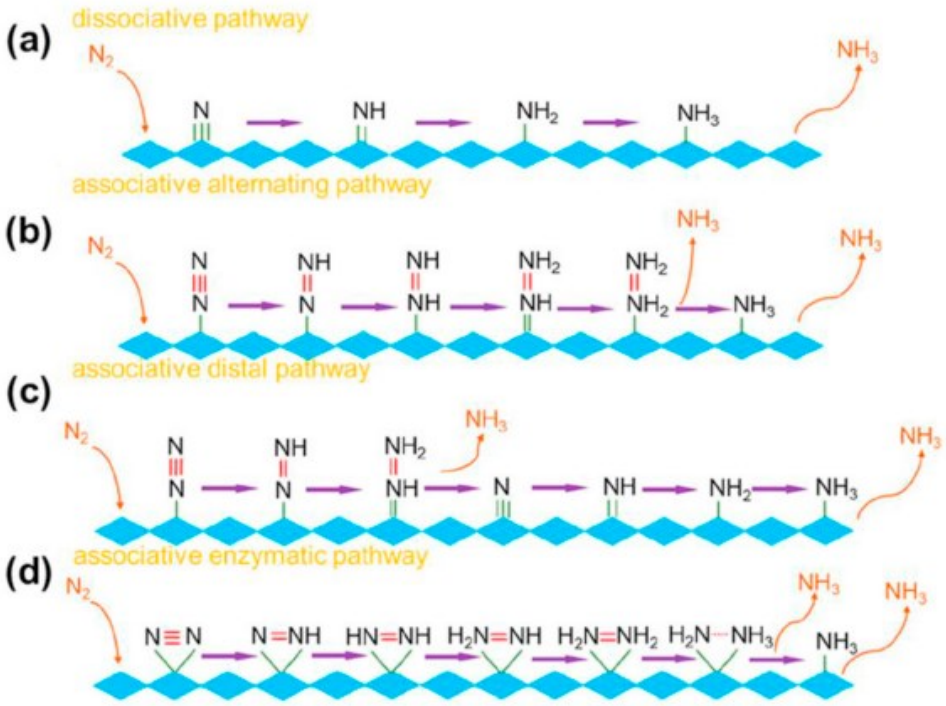

(1-23) Schematic diagram of possible mechanism for electrochemical NRR[44].

Considering the three defined steps the rate-limiting one is the step 2. For example, the Haber-Bosch process is supposed to work in a dissociative way (a), and it takes two to five atoms of Fe catalyst to break a nitrogen molecule, meanwhile hydrogen atoms simultaneously replace the broken bond. Kinetically wise, the dissociative way just described is the most favourable one but requires the high pressures and temperatures of the Haber-Bosch process to break the nitrogen molecule in a single step. In

milder conditions of electrochemical synthesis, the direct triple bond breaking is not favoured, reason why the others three mechanisms are proposed. (b)/(c) The associative alternating and distal pathways see the N_2 adsorbed in an end-on mode way and only then the hydrogenation takes place on both atoms. In the enzymatic pathway (d) the hydrogenation is also alternated between the two nitrogen atoms as for (b), but the N_2 adsorption on the catalyst goes in a side-on mode.

The research for catalytic materials for this process, once overcome environment stability, needed conductivities and electrolyte affinity, goes toward a compound that can possibly catalyse most of the possible associative pathways.

Not a plentiful literature is present when dealing with H-SOEC for ammonia synthesis, but the currently researched materials for cathode catalysis are: Ni-BZCY72 cermets[46], that reached a value of produced an ammonia flow at 620°C of $4.1x10^{-9}$ mol/s·cm^2; $Pr_{0.6}Ba_{0.4}Fe_{0.8}Cu_{0.2}O_{3-\delta}$ in an O-SOEC with CGO electrolyte, which at 400 °C produced $1.83x10^{-9}$ mol/s·cm^2 ammonia flow[47]; $3.0x10^{-10}$ mol/s·cm^2 flow of ammonia reached by a multicomponent material LSCrF-GDC[45].

In this master thesis work the materials of choice for electrode applications resulting from multiple consideration, better described in the following chapter, are double perovskites structures $BaSrFe_{1.5}Mo_{0.5}O_{6-\delta}$ and $BaSrCo_{0.2}Mo_{1.8}O_{6-\delta}$.

1.7 References

(1) Diffenbaugh, N. S.; Barnes, E. A. Data-Driven Predictions of the Time Remaining until Critical Global Warming Thresholds Are Reached. **2023**, *120* (6).

(2) Shaftel, H. *What Is Climate Change?*. Climate Change: Vital Signs of the Planet. https://climate.nasa.gov/what-is-climate-change.

(3) *Progress (Stanford Encyclopedia of Philosophy)*. https://plato.stanford.edu/entries/progress/.

(4) *Renewable Energy | Department of Energy*. https://www.energy.gov/eere/renewable-energy.

(5) *International Business, Trade and Institutional Sustainability*; Leal Filho, W., Borges De Brito, P. R., Frankenberger, F., Eds.; World Sustainability Series; Springer International Publishing: Cham, 2020. https://doi.org/10.1007/978-3-030-26759-9.

(6) Baum, Z. J.; Bird, R. E.; Yu, X.; Ma, J. Lithium-Ion Battery Recycling─Overview of Techniques and Trends. *ACS Energy Lett.* **2022**, *7* (2), 712–719. https://doi.org/10.1021/acsenergylett.1c02602.

(7) Philippot, M.; Alvarez, G.; Ayerbe, E.; Van Mierlo, J.; Messagie, M. Eco-Efficiency of a Lithium-Ion Battery for Electric Vehicles: Influence of Manufacturing Country and Commodity Prices on GHG Emissions and Costs. *Batteries* **2019**, *5* (1), 23. https://doi.org/10.3390/batteries5010023.

(8) European Commission. Methodology for Determining Greenhouse Gas Emissions Savings from Renewable Liquid and Gaseous Transport Fuels of Non-Biological Origin and from Recycled Carbon Fuels, 2023.

(9) *As electric vehicles take off, we'll need to recycle their batteries*. Environment. https://www.nationalgeographic.com/environment/article/electric-vehicles-take-off-recycling-ev-batteries.

(10) Martino, M.; Ruocco, C.; Meloni, E.; Pullumbi, P.; Palma, V. Main Hydrogen Production Processes: An Overview. *Catalysts* **2021**, *11* (5), 547. https://doi.org/10.3390/catal11050547.

(11) Rambhujun, N.; Salman, M. S.; Wang, T.; Pratthana, C.; Sapkota, P.; Costalin, M.; Lai, Q.; Aguey-Zinsou, K.-F. Renewable Hydrogen for the Chemical Industry. *MRS Energy Sustain.* **2020**, *7* (1), 33. https://doi.org/10.1557/mre.2020.33.

(12) Der bivalente V12-Motor des BMW Hydrogen 7. The Bi-Fuel V12 Engine of the New BMW Hydrogen 7, 2022.

(13) Zamfirescu, C.; Dincer, I. Ammonia as a Green Fuel and Hydrogen Source for Vehicular Applications. *Fuel Process. Technol.* **2009**, *90* (5), 729–737. https://doi.org/10.1016/j.fuproc.2009.02.004.

(14) Hu, Z.; Yin, Z.; An, Y.; Pei, Y. Ammonia as Fuel for Future Diesel Engines. In *Diesel Engines - Current Challenges and Future Perspectives [Working Title]*; IntechOpen, 2023. https://doi.org/10.5772/intechopen.1002059.

(15) *Comparisons - NH3 Fuel Association*. https://nh3fuelassociation.org/comparisons/.

(16) Tornatore, C.; Marchitto, L.; Sabia, P.; De Joannon, M. Ammonia as Green Fuel in Internal Combustion Engines: State-of-the-Art and Future Perspectives. *Front. Mech. Eng.* **2022**, *8*, 944201. https://doi.org/10.3389/fmech.2022.944201.

(17) Fang, H. Challenges with the Ultimate Energy Density with Li-Ion Batteries. *IOP Conf. Ser. Earth Environ. Sci.* **2021**, *781* (4), 042023. https://doi.org/10.1088/1755-1315/781/4/042023.

(18) *Li-ion battery pack prices rise for first time to $151/kWh | EV Markets Reports*. https://evmarketsreports.com/battery-pack-prices-rise-for-first-time-to-151-kwh/.

(19) [From the Report: ICF Canada, Clean Fuel Standard; Supply & Demand Implications. Availability of Biofuels: Clean Fuel Standard Supply and Demand Implications, 2020.

(20) *Solid oxide fuel cell - Wikipedia*. https://en.wikipedia.org/wiki/Solid_oxide_fuel_cell.

(21) Ebbesen, S. D.; Jensen, S. H.; Hauch, A.; Mogensen, M. B. High Temperature Electrolysis in Alkaline Cells, Solid Proton Conducting Cells, and Solid Oxide Cells. *Chem. Rev.* **2014**, *114* (21), 10697–10734. https://doi.org/10.1021/cr5000865.

(22) *Proton-exchange membrane fuel cell - Wikipedia*. https://en.wikipedia.org/wiki/Proton-exchange_membrane_fuel_cell.

(23) *Phosphoric acid fuel cell - Wikipedia*. https://en.wikipedia.org/wiki/Phosphoric_acid_fuel_cell.

(24) *Molten carbonate fuel cell - Wikipedia*. https://en.wikipedia.org/wiki/Molten_carbonate_fuel_cell.

(25) Xu, Q.; Guo, Z.; Xia, L.; He, Q.; Li, Z.; Temitope Bello, I.; Zheng, K.; Ni, M. A Comprehensive Review of Solid Oxide Fuel Cells Operating on Various Promising Alternative Fuels. *Energy Convers. Manag.* **2022**, *253*, 115175. https://doi.org/10.1016/j.enconman.2021.115175.

(26) Lucia, U. Overview on Fuel Cells. *Renew. Sustain. Energy Rev.* **2014**, *30*, 164–169. https://doi.org/10.1016/j.rser.2013.09.025.

(27) Zhu, H.; Kee, R. J. Thermodynamics of SOFC Efficiency and Fuel Utilization as Functions of Fuel Mixtures and Operating Conditions. *J. Power Sources* **2006**, *161* (2), 957–964. https://doi.org/10.1016/j.jpowsour.2006.05.006.

(28) *NIST Chemistry WebBook*. https://webbook.nist.gov/chemistry/.

(29) J.E. O'Brien; X. Zhang; G.K. Housley; K. DeWall; L. Moore-McAteer. *High Temperature Electrolysis Pressurized Experiment Design, Operation, and Results*; INL/EXT-12-26891, 1056004; 2012; p INL/EXT-12-26891, 1056004. https://doi.org/10.2172/1056004.

(30) Bierschenk, D. M.; Wilson, J. R.; Miller, E.; Dutton, E.; Barnett, S. A. A Proposed Method for High Efficiency Electrical Energy Storage Using Solid Oxide Cells. *ECS Trans.* **2011**, *35* (1), 2969–2978. https://doi.org/10.1149/1.3570297.

(31) Sun, X.; Chen, M.; Jensen, S. H.; Ebbesen, S. D.; Graves, C.; Mogensen, M. Thermodynamic Analysis of Synthetic Hydrocarbon Fuel Production in Pressurized Solid Oxide Electrolysis Cells. *Int. J. Hydrog. Energy* **2012**, *37* (22), 17101–17110. https://doi.org/10.1016/j.ijhydene.2012.08.125.

(32) Barbi, G.; Mari, C. High Temperature Water Electrolysis: Cathodic Behaviour of Pt/Yttria Stabilized Zirconia (Ysz) Interface. *Solid State Ion.* **1982**, *6* (4), 341–351. https://doi.org/10.1016/0167-2738(82)90020-0.

(33) Kirubakaran, A.; Jain, S.; Nema, R. K. A Review on Fuel Cell Technologies and Power Electronic Interface. *Renew. Sustain. Energy Rev.* **2009**, *13* (9), 2430–2440. https://doi.org/10.1016/j.rser.2009.04.004.

(34) Isenberg, A. Energy Conversion via Solid Oxide Electrolyte Electrochemical Cells at High Temperatures. *Solid State Ion.* **1981**, *3–4*, 431–437. https://doi.org/10.1016/0167-2738(81)90127-2.

(35) Ebbesen, S. D.; Mogensen, M. Kinetics of Oxidation of H 2 and Reduction of H 2 O in Ni-YSZ Based Solid Oxide Cells. *ECS Trans.* **2013**, *50* (49), 167–182. https://doi.org/10.1149/05049.0167ecst.

(36) Wolf, S. E.; Winterhalder, F. E.; Vibhu, V.; De Haart, L. G. J. (Bert); Guillon, O.; Eichel, R.-A.; Menzler, N. H. Solid Oxide Electrolysis Cells – Current Material Development and Industrial Application. *J. Mater. Chem. A* **2023**, *11* (34), 17977–18028. https://doi.org/10.1039/D3TA02161K.

(37) Wehrle, L.; Schmider, D.; Dailly, J.; Banerjee, A.; Deutschmann, O. Benchmarking Solid Oxide Electrolysis Cell-Stacks for Industrial Power-to-Methane Systems via Hierarchical Multi-Scale Modelling. *Appl. Energy* **2022**, *317*, 119143. https://doi.org/10.1016/j.apenergy.2022.119143.

(38) Tucker, M. C. Progress in Metal-Supported Solid Oxide Fuel Cells: A Review. *J. Power Sources* **2010**, *195* (15), 4570–4582. https://doi.org/10.1016/j.jpowsour.2010.02.035.

(39) Adler, S. B.; Lane, J. A.; Steele, B. C. H. Electrode Kinetics of Porous Mixed-Conducting Oxygen Electrodes. *J. Electrochem. Soc.* **1996**, *143* (11), 3554–3564. https://doi.org/10.1149/1.1837252.

(40) Kozuka, H.; Ohbayashi, K.; Koumoto, K. Electronic Conduction in La-Based Perovskite-Type Oxides. *Sci. Technol. Adv. Mater.* **2015**, *16* (2), 026001. https://doi.org/10.1088/1468-6996/16/2/026001.

(41) Bi, L.; Boulfrad, S.; Traversa, E. Steam Electrolysis by Solid Oxide Electrolysis Cells (SOECs) with Proton-Conducting Oxides. *Chem Soc Rev* **2014**, *43* (24), 8255–8270. https://doi.org/10.1039/C4CS00194J.

(42) Lei, L.; Zhang, J.; Yuan, Z.; Liu, J.; Ni, M.; Chen, F. Progress Report on Proton Conducting Solid Oxide Electrolysis Cells. *Adv. Funct. Mater.* **2019**, *29* (37), 1903805. https://doi.org/10.1002/adfm.201903805.

(43) Hakim, M.; Yoo, C.-Y.; Joo, J. H.; Yu, J. H. Enhanced Durability of a Proton Conducting Oxide Fuel Cell with a Purified Yttrium-Doped Barium Zirconate-Cerate Electrolyte. *J. Power Sources* **2015**, *278*, 320–324. https://doi.org/10.1016/j.jpowsour.2014.12.046.

(44) Wu, T.; Fan, W.; Zhang, Y.; Zhang, F. Electrochemical Synthesis of Ammonia: Progress and Challenges. *Mater. Today Phys.* **2021**, *16*, 100310. https://doi.org/10.1016/j.mtphys.2020.100310.

(45) Li, R.; Liu, X.; He, G.; Hu, P.; Zhen, Q.; Liu, J. L.; Bashir, S. Green Catalytic Synthesis of Ammonia Using Solid Oxide Electrolysis Cells Composed of Multicomponent Materials. *Catal. Today* **2021**, *374*, 102–116. https://doi.org/10.1016/j.cattod.2021.03.029.

(46) Vasileiou, E.; Kyriakou, V.; Garagounis, I.; Vourros, A.; Manerbino, A.; Coors, W. G.; Stoukides, M. Electrochemical Enhancement of Ammonia Synthesis in a BaZr0.7Ce0.2Y0.1O2.9 Solid Electrolyte Cell. *Solid State Ion.* **2016**, *288*, 357–362. https://doi.org/10.1016/j.ssi.2015.12.022.

(47) Lan, R.; Alkhazmi, K. A.; Amar, I. A.; Tao, S. Synthesis of Ammonia Directly from Wet Air at Intermediate Temperature. *Appl. Catal. B Environ.* **2014**, *152–153*, 212–217. https://doi.org/10.1016/j.apcatb.2014.01.037.

2. MATERIALS

The macro-category of materials used in this master thesis work are perovskites, a big half of the vast majority of catalyst used in modern chemical industry i.e., mixed metal oxides. The choice is driven by the research of better performances, catalytic activity, stability and mixed conduction at the electrode side of a proton conducting solid oxide electrolysis cell. In order to fully understand the possible variables and capabilities of these compounds a chemical structure and performance analysis is provided.

2.1 Perovskites Structures

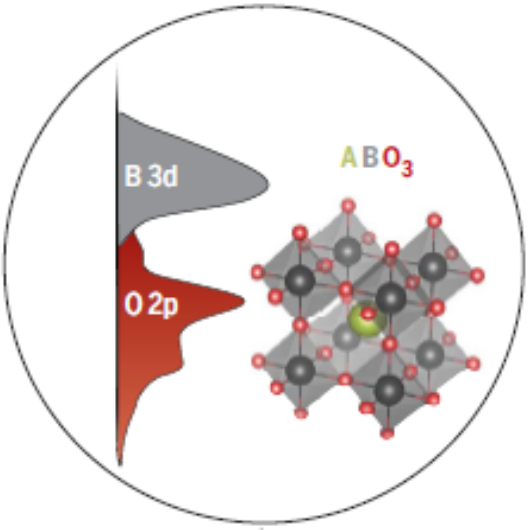

Figure 2-1 Ideal Electronic (left) and Chemical (right) structure of ABO3 perovskites with the respective dos contribution of (O 2p) and B (3d) orbitals[2].

Originally discovered by the Russian mineralogist Lev Perovski from the calcium titanate ($CaTiO_3$), perovskites materials have the general

formula ABO_3 (*Figure 2-1*) and the ideal structure is cubic with space group Pm3M-Oh[1], in which the transition metal ions in the B-site stand in the centre of octahedra whose corners composed of oxygen atoms are shared. The larger A-site cation stands in the centre of the cubic structure composed by B-site metals and has 12-fold coordination with oxygen atoms positioned in the centre of the cubic sides[2].

Ideally the B-O distance is equal to a/2 (with 'a' the cubic parameter) while the A-O distance is $a/\sqrt{2}$ so the following relation between ionic radii holds:

$$r_A + r_O = \sqrt{2}(r_B + r_O) \quad (2\text{-}1)$$

However, if the structure is not perfectly ideal the disparity introduced in this relation is described by the Goldschmidt tolerance factor (t):

$$t = (r_A + r_O)/\sqrt{2}(r_B + r_O) \quad (2\text{-}2)$$

The structure can be described as cubic in a t range $0.89<t<1.0$ but in most cases different distortion of the structure appears. If t deviates from this range the crystal structure can assume all possible symmetries. The most typical and important examples are summarised in the following points[3]:

- *Tetragonal type*

  If A is larger $t>1$ the B-O bond is distorted, increasingly with the difference between A and B radius, and a tetragonal structure is observed with crystallographic space group P4mm, e.g., $BaTiO_3$.

- *Rhombohedral type*

  This distortion causes the Z (number of atoms in the unit cell) to change from 1 to 2. However, it can be considered as a small distortion and can sometimes be described as a face centred pseudo cubic cell, e.g., $LaAlO_3$.

- *Orthorhombic type*

  The crystal group change to Pbnm and Z to 4. This is due to the change related pseudo cubic parameter, consequence of a low volume A-site cation that to keep the 12-fold site coordination with O force the Oh structure to tilt about the pseudo cubic axes to achieve the lowest energy level for the crystal. Considering the Goldschmidt factor this distortion take place for values lower than the cubic range and is the more common one, e.g., $GdFeO_3$.

Moving forward from the parental base structure ABO_3, more complex oxides with perovskite like structure $AB_{0.5}B'_{0.5}O_3$ have often served as reference materials for the study of physical properties[4]. Among these oxides in the 1950s, searching for ferroelectric and piezoelectric materials, ordered double perovskites, $A_2BB'O_6$, became of technological interest and have kept it high to these days for SOFC and SOEC application. From a structural point of view the simple cubic perovskite undergoes a distortion arising from three mechanisms: cations displacement within the BO_6 octahedra and distortion and tilting of these octahedra. Woodward[5] described the space group of ordered double perovskites as an $Fm\bar{3}m$ with a 2a cell parameter when present ideal cubic configuration.

For this type of materials it is important to denote different magnetic behaviours depending on the constituents cations, in particular for

Sr_2FeMoO_6 magnetoresistance, ferrimagnetic and half metallic behaviour have been established due to the mixed valences of Fe and Mo[4,6]. Conversely, Sr_2CoMoO_6 shows antiferromagnetic behaviour because Mo keeps the +6 oxidation state, leaving Co as the only paramagnetic cation[4].

This particular electronic and magnetic properties are to be owed to the flexible electronic structure of the perovskite oxide family, of which the density of states is represented in *Figure 2-1*, that allows, not only in double perovskites but also in general ones, to own the fundamental property of ionic proton or oxygen conductivity[2].

2.2 Protonic Conduction in Perovskites[1,7–9]

The proton conductivity is the primary and fundamental property researched in the electrolyte material for H-SOEC applications. The general formula defined to design a proton conductive perovskite is $AB_{1-x}M_xO_{3-\delta}$, where M is a trivalent dopant used to replace a tetravalent one B site to create oxygen vacancies, fundamental characteristic to obtain any ions mobility in perovskites. These vacancies generation is described by the following equation:

$$2B_B^x + O_O^x + M_2O_3 \leftrightarrow 2M_B' + V_O^{\cdot\cdot} + 2BO_2$$

(2-3)

Where the concentration of vacancies generated ($[V_O^{\cdot\cdot}]$) is equal to the concentration of the dopant M ([M(III)]) inside the compound. The formation of protons that can then be diffused inside the material follows this reaction:

$$H_2O + V_O^{\cdot\cdot} + O_O^X = 2OH_O^{\cdot}$$

(2-4)

So, protons formation occurs as hydroxide radical defect and the mechanism proposed for the migration includes fast rotation and reorientation of the proton, in the vicinity of oxygen ion followed by the transfer to the next ion. A visual description of this hopping mechanism is presented in *Figure* 2-2.

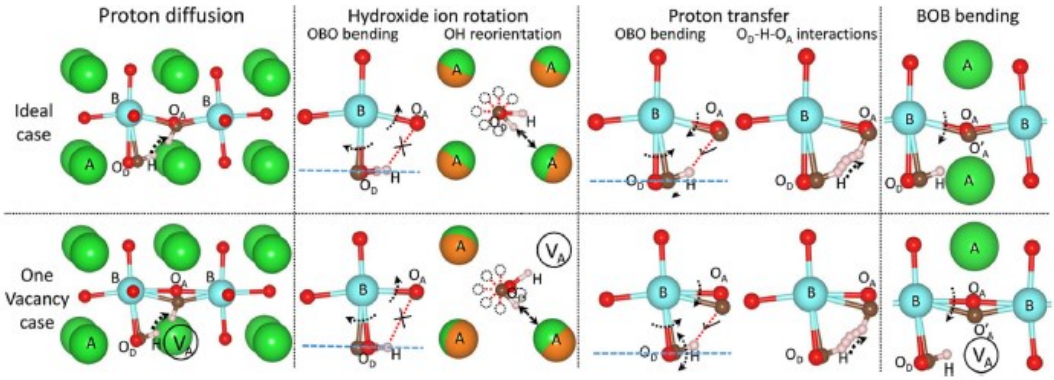

Figure 2-2 Schematic representation of proton diffusion process. In the upper row for a non-doped material and a doped one, presenting oxygen vacancies, in the lower row. Red balls represent the initial position, brown balls the final one[9].

As presented in the previous chapter dealing with proton conducting electrolytes, the state-of-art materials are yttrium doped barium cerate or barium zirconate materials; these are different for sintering and grain size properties. In this work the orthorhombic symmetric BCY10[10] ($BaCe_{0.9}Y_{0.1}O_3$) has been chosen as protonic conductor electrolyte, even if the total conductivity increases with increasing doping till Y^{3+} 20% mol, to have a more stable and easily manufacturable protonic conductor in the device, since the protonic conduction is not considered the rate limiting step in ammonia synthesis. Moreover, BCY10 present the researched low operating temperatures (300-1000 °C) and promising conductivity in the necessary wet hydrogen but also in dry nitrogen atmosphere[11]. Low operating temperatures are needed not only because oxygen ion conductivity is

required to be negligible[12] but also to provide a more stable and milder atmosphere for ammonia synthesis. The last important property provided by this material for this work purposes is the chemical compatibility with Mo, Fe, Co multi-doped barium strontium composed perovskites, tested and confirmed by Mahadik et al.[13]

2.3 Perovskite Electrode for Ammonia Synthesis

The 1.4% of all energy consumed by mankind is invested into the Haber-Bosch process for ammonia synthesis[14]. This is what it takes to reach NH_3 formation with a dissociative catalytic path, involving a heterogeneous iron or ruthenium catalyst, at temperatures thermodynamically unfavourable.

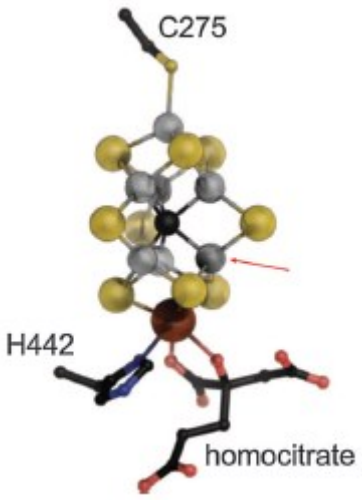

Figure 2-3 Structure of the FeMo cofactor of nitrogenase showing iron centres in metallic, sulphur atoms in gold, molybdenum in red and carbon in black, the arrow shows the postulated binding site of dinitrogen[14].

In order to change this trend is possible to look at nature, where, even if high energy demand remains, the nitrogen fixation occurs through multiple proton and electron transfer steps, without the necessity of high

temperatures or pressures. A natural example of dinitrogen reduction is provided by nitrogenases, a molecular inorganic catalyst which FeMo cofactor is made of two fused iron-sulphur clusters, of which a molybdenum atom takes up one of the atypical positions (*Figure 2-3*).

As described it does not change the process to an energy favourable one, 8 molecules of ATP are required per NH_3 molecule correspondent of 244 kJ/mol, but it is far more favourable than roughly 485 kJ/mol required for the Haber-Bosch.

So far the most successful artificial molecular systems for the reduction of dinitrogen are molybdenum based phosphine complexes[14], which are not favourable complexes for solid oxide cells, but the beneficial effects of Mo for catalytic and electrocatalytic purposes have already been tested and proved in perovskites structures[15,16]. Adding to these considerations the already used transition metal Fe in Haber-Bosch process and considering the ratio present in the substituted cluster of FeMo cofactor, a perovskite presenting a 3:1 ratio between the two B cations seems a promising choice as catalytic centre.

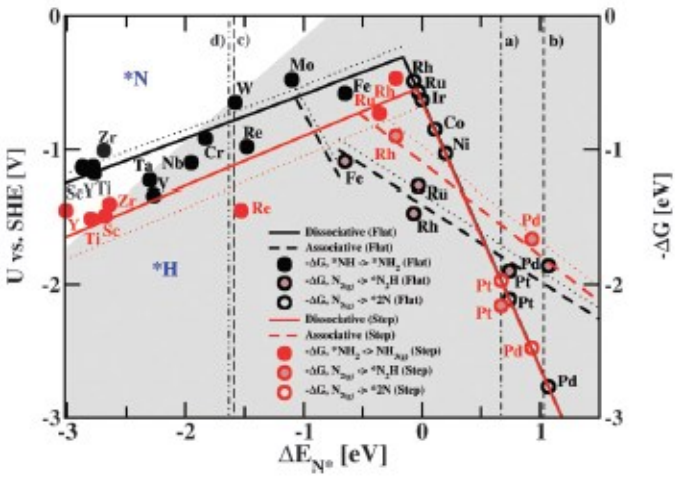

Figure 2-4 Volcanic diagram of N2 adsorption performance of transition metal obtained by DFT calculation[17].

To further support this information, according to the NRR mechanism (*Figure 2-5[B]*), Density Functional Theory (DFT) calculations confirms these two metals as the lowest potential and Gibbs free energy requiring among the environmentally friendly ones[17,18] (*Figure 2-4*).

The second catalytic option considers a molybdenum-based structure cobalt-doped to increase oxygen vacancies with the most used cathode metal for both SOEC and SOFC applications. However, given the high thermal expansion coefficient of this material it has been kept as dopant to prevent delamination and malfunctions of the researched device (*Figure 2-5[A]*).

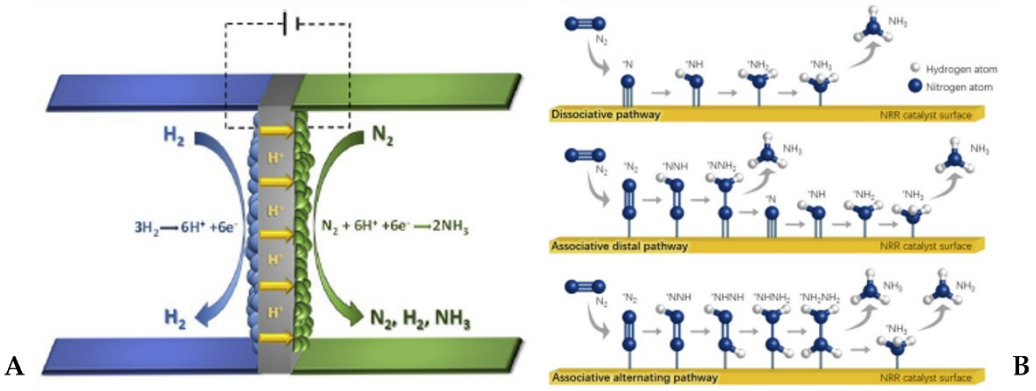

Figure 2-5 [A] Schematic diagram of the H-SOEC ammonia synthesis; [B] schematic representation of NRR mechanism[17,19].

In all the majority of cases reported with this type of device the materials composing cathode were perovskites[19]. So, to achieve a good match with the electrolyte, BCY10, the A cation of the structure has to possibly provide similar cell constant, directly proportional to the ionic radius of the atom. For this reason, half concentration of the A cation was substituted with barium, while the other half with strontium instead, to possibly reach the same orthorhombic distortion as in BCY10 and because strontium doping seems to increase electronic conductivity and

polarization resistance up to 50/60% mol doping percentage[20]. In addition to all these considerations, the final one is an optimization of the disposition of catalytic sites presenting the right B metals ratio, achieved through the ordered double perovskite structures obtained in the following compositions, that became the choice:

$$\boldsymbol{BaSrFe_{1.5}Mo_{0.5}O_{6-\delta}} \qquad \boldsymbol{BaSrCo_{0.2}Mo_{1.8}O_{6-\delta}}$$

BSFM *BSCM*

(2-5)

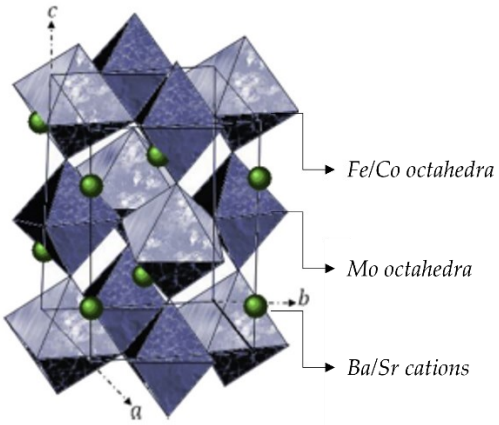

Figure 2-6 Double perovskite orthorhombic distortion[19].

Since the BSFM double perovskite doping is researched also as anode materials with MIEC characteristics[21], to deviate researches from the more common cermets, the resulting device will be tested as reversible symmetric proton conducting cell. The good anodic performances in wet-hydrogen are addressed to the redox couple Fe^{2+}/Fe^{3+} and Mo^{6+}/Mo^{5+} that can provide not only enhanced conductivity but also redox stability both in reducing-wet and oxidizing atmosphere. Such a mixed valence configuration favours an effective charge transport and also facilitates the creation of vacancies[22,23]. The experimental synthetic methods used to obtain the two researched materials will be described as follow.

2.4 References

(1) Peña, M. A.; Fierro, J. L. G. Chemical Structures and Performance of Perovskite Oxides. *Chem. Rev.* **2001**, *101* (7), 1981–2018. https://doi.org/10.1021/cr980129f.

(2) Hwang, J.; Rao, R. R.; Giordano, L.; Katayama, Y.; Yu, Y.; Shao-Horn, Y. Perovskites in Catalysis and Electrocatalysis. *Science* **2017**, *358* (6364), 751–756. https://doi.org/10.1126/science.aam7092.

(3) Moure, C.; Peña, O. Recent Advances in Perovskites: Processing and Properties. *Prog. Solid State Chem.* **2015**, *43* (4), 123–148. https://doi.org/10.1016/j.progsolidstchem.2015.09.001.

(4) Ortega-San Martin, L.; Chapman, J. P.; Lezama, L.; Sánchez-Marcos, J.; Rodríguez-Fernández, J.; Arriortua, M. I.; Rojo, T. Factors Determining the Effect of Co(II) in the Ordered Double Perovskite Structure: Sr $_2$ CoTeO $_6$. *J Mater Chem* **2005**, *15* (1), 183–193. https://doi.org/10.1039/B413341B.

(5) Woodward, P. M. Octahedral Tilting in Perovskites. II. Structure Stabilizing Forces. *Acta Crystallogr. B* **1997**, *53* (1), 44–66. https://doi.org/10.1107/S0108768196012050.

(6) Moritomo, Y.; Xu, Sh.; Machida, A.; Akimoto, T.; Nishibori, E.; Takata, M.; Sakata, M. Electronic Structure of Double-Perovskite Transition-Metal Oxides. *Phys. Rev. B* **2000**, *61* (12), R7827–R7830. https://doi.org/10.1103/PhysRevB.61.R7827.

(7) Norby, T. Proton Conductivity in Perovskite Oxides. In *Perovskite Oxide for Solid Oxide Fuel Cells*; Ishihara, T., Ed.; Fuel Cells and Hydrogen Energy; Springer US: Boston, MA, 2009; pp 217–241. https://doi.org/10.1007/978-0-387-77708-5_11.

(8) Fuller, C. A.; Blom, D. A.; Vogt, T.; Evans, I. R.; Evans, J. S. O. Oxide Ion and Proton Conductivity in a Family of Highly Oxygen-Deficient Perovskite Derivatives. *J. Am. Chem. Soc.* **2022**, *144* (1), 615–624. https://doi.org/10.1021/jacs.1c11966.

(9) Hossain, M. K.; Biswas, M. C.; Chanda, R. K.; Rubel, M. H. K.; Khan, M. I.; Hashizume, K. A Review on Experimental and Theoretical Studies of Perovskite Barium Zirconate Proton Conductors. *Emergent Mater.* **2021**, *4* (4), 999–1027. https://doi.org/10.1007/s42247-021-00230-5.

(10) Lee, K.-R.; Tseng, C.-J.; Jang, S.-C.; Lin, J.-C.; Wang, K.-W.; Chang, J.-K.; Chen, T.-C.; Lee, S.-W. Fabrication of Anode-Supported Thin BCZY Electrolyte Protonic Fuel Cells Using NiO Sintering Aid. *Int. J. Hydrog. Energy* **2019**, *44* (42), 23784–23792. https://doi.org/10.1016/j.ijhydene.2019.07.097.

(11) Doubova, L.; Barison, S.; Boldrini, S.; Fabrizio, M.; Mortalò, C.; Pagura, C. Conductivity Studies of Sol-Gel Prepared $BaCe_{0.85-x}Zr_xY_{0.15}O_{3-\delta}$ Solid Electrolytes Using Impedance Spectroscopy. *J. Appl. Electrochem.* **2009**, *39* (11), 2129–2141. https://doi.org/10.1007/s10800-009-9932-0.

(12) Lefebvre-Joud, F.; Gauthier, G.; Mougin, J. Current Status of Proton-Conducting Solid Oxide Fuel Cells Development. *J. Appl. Electrochem.* **2009**, *39* (4), 535–543. https://doi.org/10.1007/s10800-008-9744-7.

(13) Mahadik, P. S.; Shirsat, A. N.; Saha, B.; Sitapure, N.; Tyagi, D.; Varma, S.; Wani, B. N.; Bharadwaj, S. R. Chemical Compatibility Study of BSCF Cathode Materials with Proton-Conducting BCY/BCZY/BZY Electrolytes. *J. Therm. Anal. Calorim.* **2019**, *137* (6), 1857–1866. https://doi.org/10.1007/s10973-019-08082-2.

(14) Van Der Ham, C. J. M.; Koper, M. T. M.; Hetterscheid, D. G. H. Challenges in Reduction of Dinitrogen by Proton and Electron Transfer. *Chem Soc Rev* **2014**, *43* (15), 5183–5191. https://doi.org/10.1039/C4CS00085D.

(15) Carollo, G.; Garbujo, A.; Mauvy, F.; Glisenti, A. Critical Raw Material-Free Catalysts and Electrocatalysts: Complementary Strategies to Activate Economic, Robust, and Ecofriendly SrTiO 3. *Energy Fuels* **2020**, *34* (9), 11438–11448. https://doi.org/10.1021/acs.energyfuels.0c01678.

(16) Wang, S.; Jiang, H.; Gu, Y.; Yin, B.; Chen, S.; Shen, M.; Zheng, Y.; Ge, L.; Chen, H.; Guo, L. Mo-Doped $La_{0.6}Sr_{0.4}FeO_{3-\delta}$ as an Efficient Fuel Electrode for Direct Electrolysis of CO2 in Solid Oxide Electrolysis Cells. *Electrochimica Acta* **2020**, *337*, 135794. https://doi.org/10.1016/j.electacta.2020.135794.

(17) Skúlason, E.; Bligaard, T.; Gudmundsdóttir, S.; Studt, F.; Rossmeisl, J.; Abild-Pedersen, F.; Vegge, T.; Jónsson, H.; Nørskov, J. K. A Theoretical Evaluation of Possible Transition Metal Electro-Catalysts for N 2 Reduction. *Phys Chem Chem Phys* **2012**, *14* (3), 1235–1245. https://doi.org/10.1039/C1CP22271F.

(18) Du, F.; Sun, W.; Luo, H.; Li, C. M. Recent Progress in Electrochemical Synthesis of Carbon-Free Hydrogen Carrier Ammonia and Ammonia Fuel Cells: A Review. *Mater. Rep. Energy* **2022**, *2* (4), 100163. https://doi.org/10.1016/j.matre.2022.100163.

(19) Kyriakou, V.; Garagounis, I.; Vasileiou, E.; Vourros, A.; Stoukides, M. Progress in the Electrochemical Synthesis of Ammonia. *Catal. Today* **2017**, *286*, 2–13. https://doi.org/10.1016/j.cattod.2016.06.014.

(20) Pajot, M.; Duffort, V.; Capoen, E.; Mamede, A.-S.; Vannier, R.-N. Influence of the Strontium Content on the Performance of $La_{1-x}Sr_xMnO_3/Bi_{1.5}Er_{0.5}O_3$ Composite Electrodes for Low Temperature Solid Oxide Fuel Cells. *J. Power Sources* **2020**, *450*, 227649. https://doi.org/10.1016/j.jpowsour.2019.227649.

(21) Zheng, K.; Lach, J.; Zhao, H.; Huang, X.; Qi, K. Magnesium-Doped $Sr_2(Fe,Mo)O_{6-\delta}$ Double Perovskites with Excellent Redox Stability as Stable Electrode Materials for Symmetrical Solid Oxide Fuel Cells. *Membranes* **2022**, *12* (10), 1006. https://doi.org/10.3390/membranes12101006.

(22) Zheng, K.; Świerczek, K. A- and B-Site Doping Effect on Physicochemical Properties of $Sr_{2-x}Ba_xMMoO_6$ (M = Mg, Mn, Fe) Double Perovskites — Candidate Anode Materials for SOFCs. *Funct. Mater. Lett.* **2016**, *09* (04), 1641002. https://doi.org/10.1142/S1793604716410022.

(23) Skutina, L.; Filonova, E.; Medvedev, D.; Maignan, A. Undoped Sr2MMoO6 Double Perovskite Molybdates (M = Ni, Mg, Fe) as Promising Anode Materials for Solid Oxide Fuel Cells. *Materials* **2021**, *14* (7), 1715. https://doi.org/10.3390/ma14071715.

3. EXPERIMENTAL

3.1 Synthesis Methods

The synthesis of the two perovskite structures, $BaSrFe_{1.5}Mo_{0.5}O_6$ (BSFM) and $BaSrCo_{0.2}Mo_{1.8}O_6$ (BSCM), have been successfully achieved through wet chemistry methodology. The first followed procedure has been the sol-gel route utilizing only citric acid as complexing agent, a route namely defined as Citrate or Marcilly method, that allows to obtain good structural purity minimizing the segregation of secondary phases while allowing good homogeneity[1]. This methodology was subsequently switched with the similar Pechini approach, a method originally popularized by H. Anderson in 1970s to fabricate perovskites powders for magnetohydrodynamic electrodes. This methodology differs from the simple citric acid providing not only chelation of metal cations, but by favouring a subsequent cross-linked esterification to create gel with the aid of polyalcohol (in this case ethylene glycol) in a slightly acid solution[2,3].

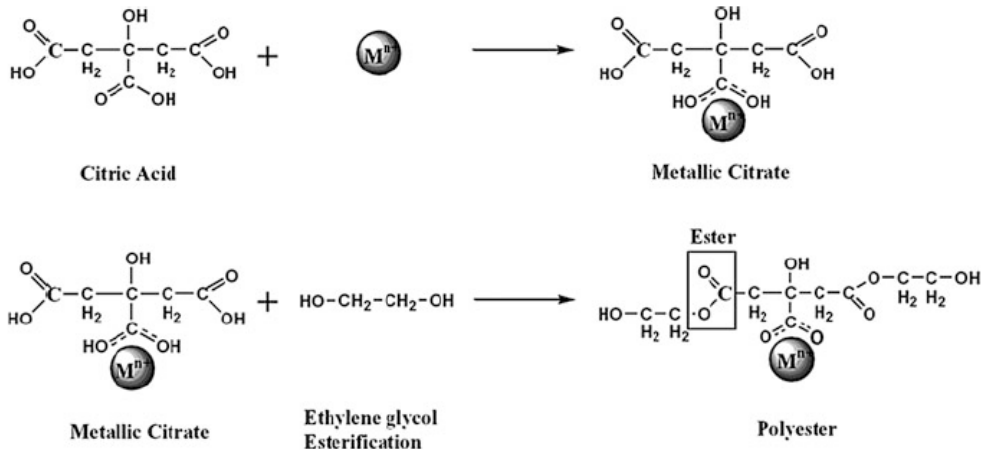

Figure 3-1 Scheme of the Pechini Method reactions[2].

This has the advantage of allowing the use of metals that do not have stable hydroxy species, distributing cations throughout the polymer structure, resulting in what can be seen as a more homogenous ion distribution at the molecular level, optimal properties since ordinated double doped perovskites are researched.

The first step of both synthesis routes is the dissolution of metal precursors in distilled water, heated to optimise solubility. The chosen precursors for both routes were: $Ba(NO_3)_2$, $Sr(NO_3)_2$, $(NH_4)_6Mo_7O_{24}{\cdot}4H_2O$ [ammonium molybdate], $Fe(NO_3)_3$, $C_{10}H_{14}CoO_4$ [Cobalt (II) acetylacetonate]. Each precursor weighted to achieve stoichiometric ratio of the researched formula but the complexing agents. Citric acid and ethylene glycol, when used, where added to the solution after the complete dissolution of each compound, respectively in 5:1 and 40:1 molar ratio following procedure of Zapata-Ramirez et al.[4], and each solution has been kept under stirring and heating until wet gel formation (*Figure 3-2*[5]). Each process has a pH regulation by ammonia addition to a value of low 6, then the temperature increases to 400°C helps the process through the step of dry gel and the final pyrolysis by self-combustion. Before proceeding obtained powders were refined by mortar crushing.

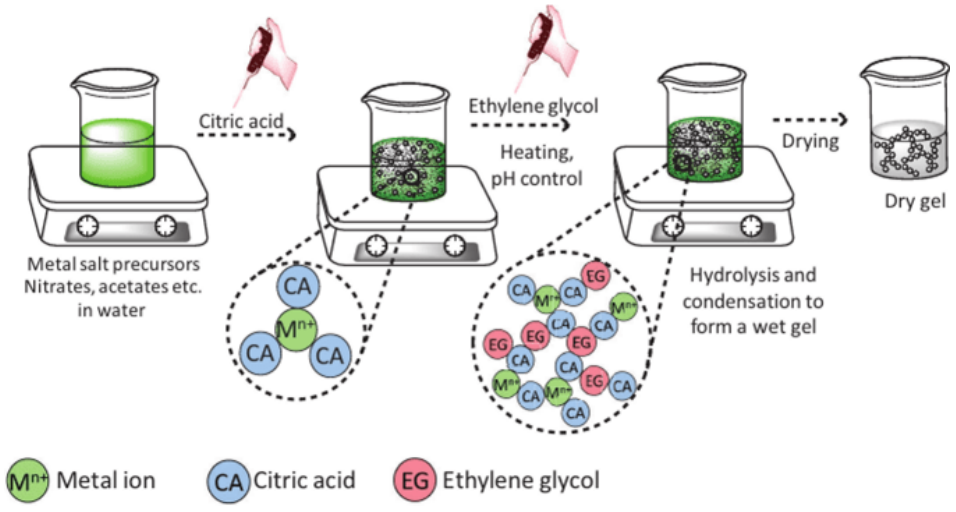

Figure 3-2 Schematic representation of the synthetic process used[4].

Then the crystallization by calcination was performed and analysed with X-Ray Diffraction to evaluate the success of the synthesis procedure. Diffractograms have been carried out through a *Brucker D8 Advance* diffractometer, utilizing a Bragg-Brentano geometry and Cu Kα radiation (λ=0.154 nm, 40 kV, 40 mA). Each diffractogram collected using 0.02°/step and 0.34s/step, in the 2θ range that goes from 20° to 80°. The subsequent identification of crystalline phases was done through a search-match method using the JCPDS database.

3.2 Calcination and Characterization

3.2.1 BSCM - $BaSrCo_{0.2}Mo_{1.8}O_6$

The $BaSrCo_{0.2}Mo_{1.8}O_6$ compound was the first of the two to be synthesized because it presents no literature to be assisted with, so its production process has been considered as a harder one to pursue. Despite poor comparison with literature, its analysis was in any case useful even to describe molybdenum and its probable role in the electrochemical ammonia synthesis, later analysed. Thus, the first synthetic process tested was the less complexing agent draining, the Marcilly method, followed by the calcination of mixed cations at 1000°C in air following the procedure of Moritomo et al.[6]

The main used characterization method is XRD analysis, due to the need of verifying, at first, the crystal structure of the researched material. The reflex pattern expected for BSCM has been carried out calculating mean angle values between two databased references: Ba_2CoMoO_6 and Sr_2CoMoO_6. Considering the same crystallographic structure tabulated

(*pbnm* or *orthorhombic distortion*), the differences has been regarded to ionic radius of the A dopant Ba^{2+}(R^{XII}= 1.61 Å) and Sr^{2+}(R^{XII}= 1.44 Å) that in the two structures generate the same pattern shifted respectively at lower and higher angles. The influence of the metallic ratio discordance with database is instead rather low, considering the same geometric structure expected, because the ionic radius is similar for the redox couple Co^{2+}(R^{VI}= 0.65 Å) and Mo^{6+}(R^{VI}= 0.59 Å) and equal for Co^{3+}(R^{VI}= 0.61 Å) and Mo^{5+}(R^{VI}= 0.61 Å).[7]

The air atmosphere calcinated-sample diffractogram (black line) did not present only the expected pattern, but the presence of the insulant oxide phase $BaMoO_4$ that represents the more thermodynamically stable species, and whose reflexions are predominant in the diffractogram (*Figure 3-3*).

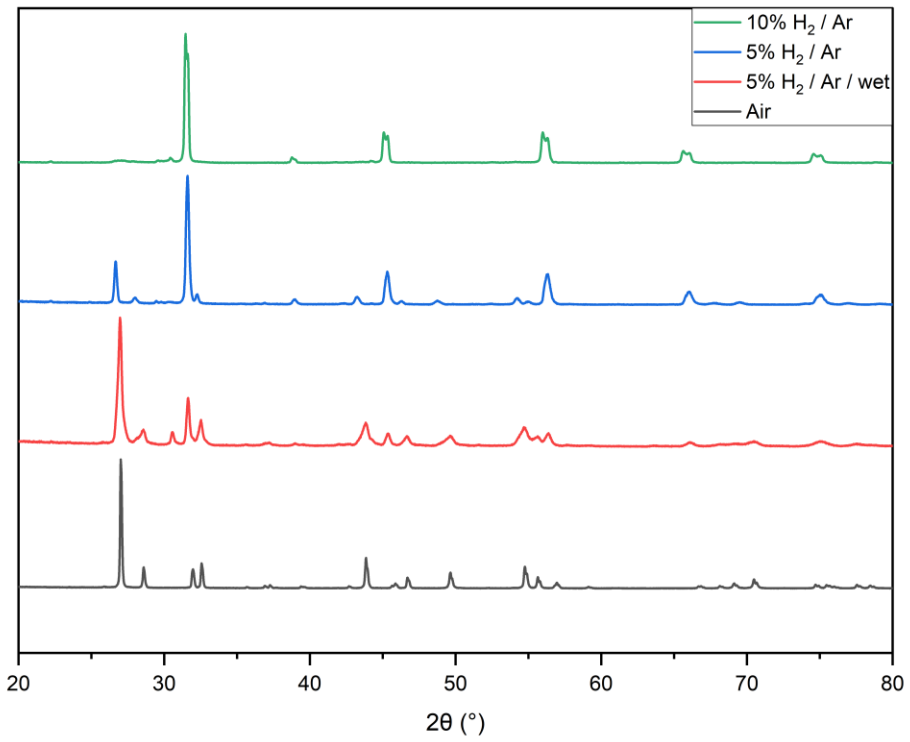

Figure 3-3 Room temperature XRD of $BaSrCo_{0.2}Mo_{1.8}O_6$ (BSCM) in four different calcination condition at 1000°C, 6 hours each.

Once experimentally confirmed the thermodynamical instability of the researched structure in oxidant conditions, three different reducing atmospheres have been tested. The mild reduction atmosphere, a calcination method tested by Carollo et al.[8] for molybdenum compounds, consisting of 5% volumetric percentage of hydrogen in argon carrier fluxed through a distilled water filled bubbler, showed the researched diffraction pattern intensity increase. The subsequent 5% vol and 10 % vol of H_2 dry showed the increase and the purity of BSCM structure recorded to the detection limit threshold, with a minor presence of metallic Co.

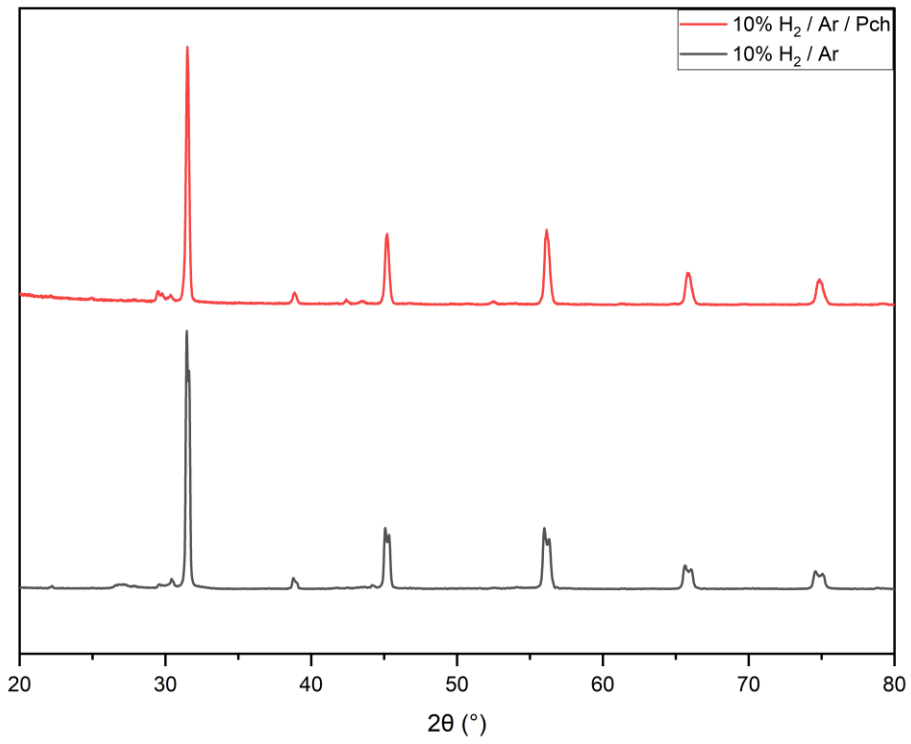

Figure 3-4 Room temperature XRD diffraction comparison between Pechini (above) and Marcilly (under) for BSCM, both at 1000°C for 6 hours in the same atmosphere.

As it is showed in *Figure 3-4* all collected reflexes for the Marcilly synthesis, even if matching the angular position and intensity expectation,

are doubled, phenomena that may be due to several reasons but the most probable one is symmetry reduction of the phase, because planes in different symmetries has different distances that causes different Bragg angles.[9] For this reason the more complexing agent demanding but promising Pechini method for low doping percentage has been used.

Figure 3-4 shows the comparison between the two synthesis methods both without unresearched phases or structures, obtained in the same conditions. The Pechini method assists the synthesis process to a single symmetry phase, consistently with the expected results, so presenting fundamental characteristics since a double perovskite ordered structures comparison is researched and provided in this work.

3.2.2 BSFM - $BaSrFe_{1.5}Mo_{0.5}O_6$

The synthesis of $BaSrFe_{1.5}Mo_{0.5}O_6$ allows more comparisons with literature. Proceeding directly with the more promising tested Pechini method, dissolving stoichiometric amounts of precursors in distilled water, followed ethylene glycol and citric acid to form the sol and the gel after heating. Subsequently to the 400°C treatment, the calcination at 1000°C for 6 hours in air took place following the procedure of J. H. Wright et al.[10] for the synthesis of $Sr_2Fe_{1.5}Mo_{0.5}O_6$. Their XRD trace is reported in *Figure 3-5* and considering a comparison with *Figure 3-6* air treatment, in Wright et al. pattern the impurity of strontium molybdate oxides is very low even if the used quantity of molybdenum is equal. The reason is to be addressed to the higher barium molybdenum oxides ($BaMoO_4$) thermodynamical stability, that, compared to the corresponding strontium molybdenum oxide, has a lower formation enthalpy both at lower and higher temperatures.[11]

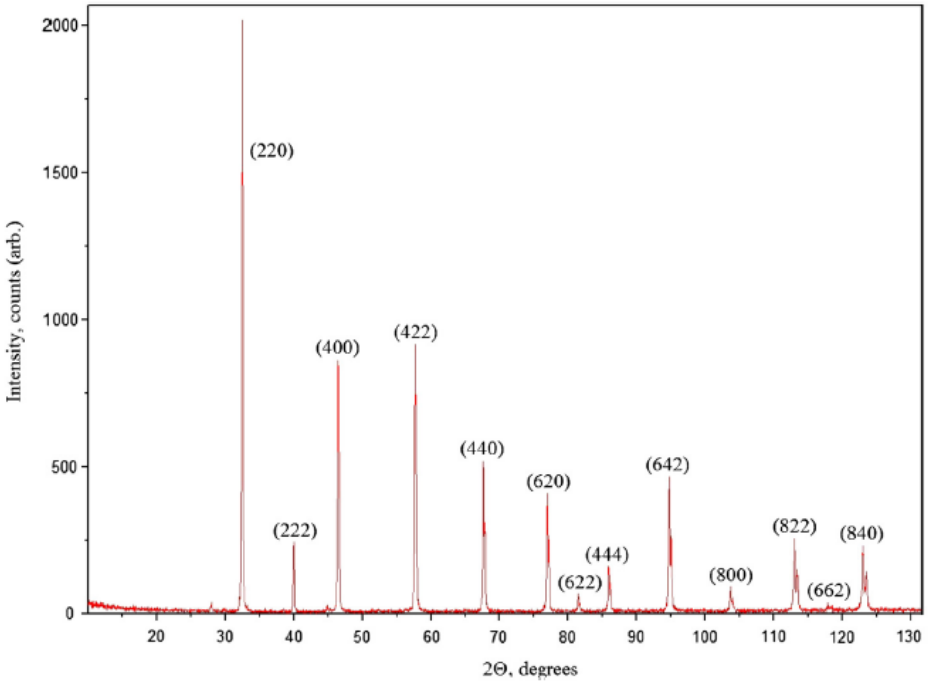

Figure 3-5 XRD trace of Sr2Fe1.5Mo0.5O6 (SFMO) by J.H. Wright et al.[9]

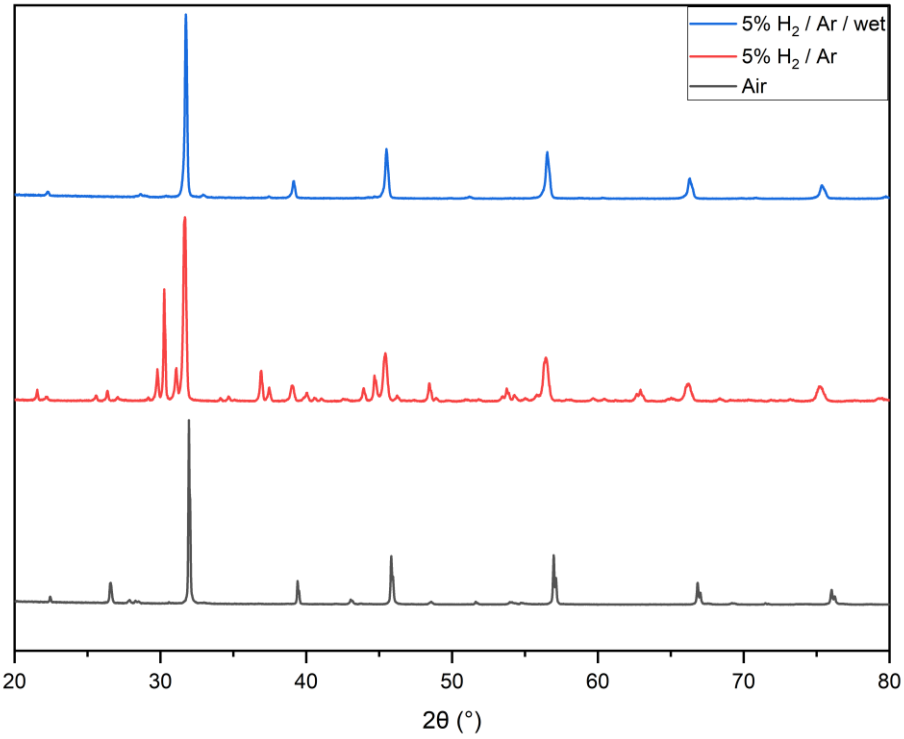

Figure 3-6 Room temperature XRD of $BaSrFe_{1.5}Mo_{0.5}O_6$ (BSFM) in three different calcination condition at 1000°C, 6 hours each.

Having already tested the barium molybdates removal with reducing atmosphere calcination, the treatment has been repeated for both dry and wet (mild conditions) reduction, with the same temperatures and time parameters (1000°C for 6h). As expected for lower molybdenum contents, the mild reduction reported by Carollo et al.[8] resulted in high purity diffraction trace.

The reference signals where again calculated with a mean value between $Sr_2Fe_{1.5}Mo_{0.5}O_6$ and $Ba_2Fe_{1.5}Mo_{0.5}O_6$ database structure of double perovskites. In this case the B metal cations ratio had the correct values in tabulated structures, even if the same characteristic of ionic radius difference presented by BSCM for both redox couples is similar [$Fe^{2+}(R^{VI}$= 0.61 Å)/$Mo^{6+}(R^{VI}$= 0.59 Å); $Fe^{3+}(R^{VI}$= 0.645 Å)/$Mo^{5+}(R^{VI}$= 0.61 Å)][7].

Differently from Mo-rich one, the material result very sensitive to the dry reducing atmosphere, in particular iron forms different oxides structures with both Ba and Sr and a fraction is reduced to in this metallic form Fe^0.[12] Anyway this sensitivity does not result in any drawback if the material is applied to the usual atmosphere of proton conducting SOCs, since water vapour is always present with the hydrogen flux fuel inlet, so pure synthesis condition are matched.

3.3 Temperature-Programmed Reduction (TPR)

Considering the structuration of BSCM and BSFM in a proton conducting solid oxide cell device, the behaviour of both materials under reductive atmosphere must be analysed more in depth, being this one of the possible conditions present at the anodic side of the cell. This process has been carried out through the Temperature-Programmed Reduction (TPR)

performed by *Micromeritics AutoChem II*, equipped with a Thermal Conductivity Detector (TCD).

Measurement have been carried out in an atmosphere of 5% H_2 / Ar from room temperature to 1000°C with a ramp of 5°C/min, letting the flow across the catalyst. The linear heating allows the reduction to be correlated with temperature with a highly sensitive detector that continually analyses the chemical difference in atmospheric concentration at the outlet, producing an accurate peak reduction rate of the analysed material surface. The analysis is provided by the TCD measuring the thermal conductivity of the outlet gas, which depend on the gas composition.

Following the synthesis order, the first powder submitted to this treatment is BSCM (*Figure 3-7*).

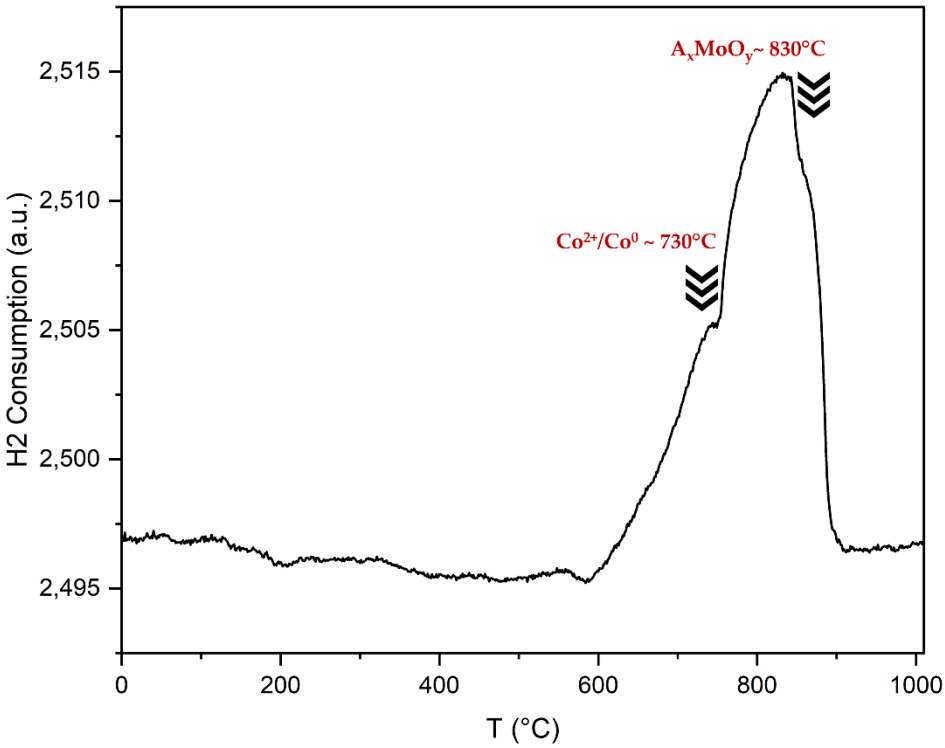

Figure 3-7 TPR curve for the BSCM powder after treatment at 1000°C in Air.

Starting considerations from high temperatures, the displayed TPR profile present the expected maximum responsible for the reduction of structural molybdenum oxides (A_xMoO_y)[13], a signal that is reported to have various contribution depending on the Mo coordination, but terminates before reaching the 1000°C threshold, confirming the complete reduction of molybdates oxides as reported in XRD diffractograms (*Figure 3-3*). The large profile reported can be described, with literature comparison, as an overlay of, at least, another contribution besides the multiple ones due to Mo (around 800 °C); the second one consists in the reduction from Co^{2+} to Co^0, also reported in the X-Ray diffraction pattern. On the other hand, an expected non detected reduction is the Co^{3+}/Co^{2+} at ~400/420°C, phenomenon partially assigned to the sensibility threshold of the used machine at low temperatures.

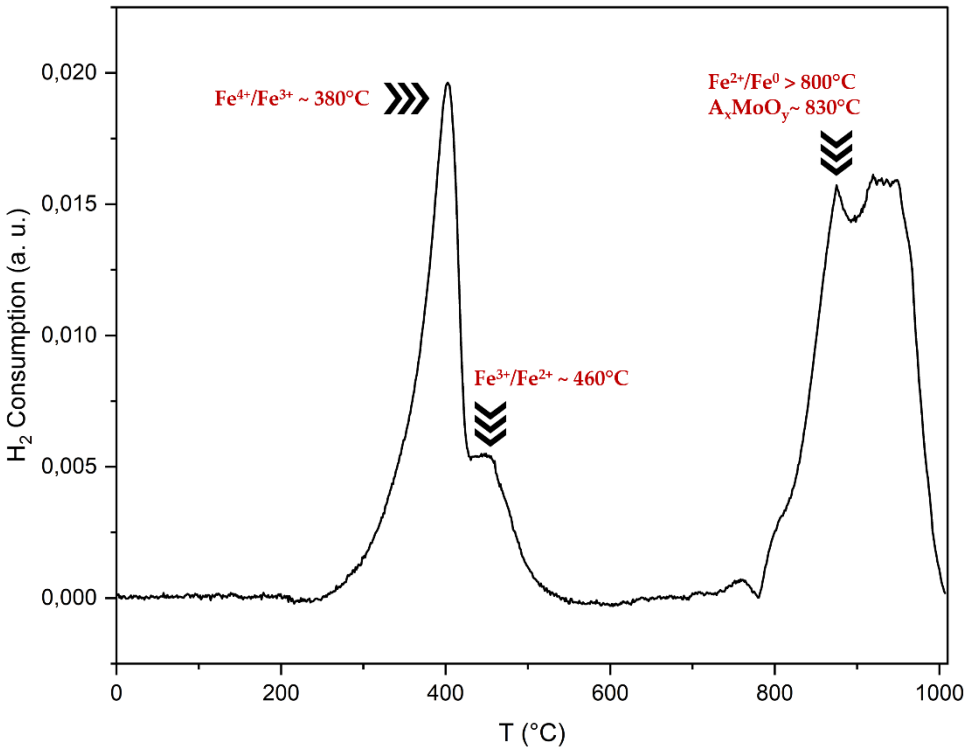

Figure 3-8 TPR curve for the BSFM powder after treatment at 1000°C in Air.

In the case of BSFM (*Figure 3-8*) the hydrogen absorption profile matches expectation and comparison with literature data.[12,14] Starting again from the high temperature maximum, it underlies the already described multiple structural phases A_xMoO_y reduction and the conversion of the easily accessible fraction of Fe^{2+} converted into metallic Fe. At lower temperatures is possible to clearly define at least two contributions in the other adsorption profile, precisely the Fe^{4+}/Fe^{3+} at ~380°C and the Fe^{3+}/Fe^{2+} at ~460°C. All peaks are broadened depending on how strongly the precursor driving the process interacts with its surroundings.

This analysis confirms the stability in hydrogen atmosphere of both compounds in the operating range of a proton conducting SOC (~400-750°C) addressing the H_2 adsorption recorded to modification in oxidation states that does not influence the structural stability of the researched compound.

3.3 Materials Stability for SOCs application

In order to evaluate the behaviour of the synthetised materials during the process of device fabrication and while in working conditions, further temperature and atmosphere assisted treatments have been performed.

Nowadays there are three major challenges to be faced when designing an electrode material for industrial SOCs application. One is the working temperature, generally T > 800°C, faced in this work with the lower temperature activation of the proton conduction. The second one is the high materials costs minimized with the symmetrical design, allowed by designing electrodes capable of both anode and cathode working attitude; this is relevant allowing R-SOC applications. The last one is the degradation

rate of the device due to delamination, and perovskite structure degradation, especially if the electrodes are stable only in predetermined environments[15].

To evaluate the effective in device stability of BSCM and BSFM, some processes have been tested:

- *Structure Recovery*: for both materials the researched XRD trace has been recovered from every atmosphere condition applied: Air, H_2 5% / Ar / wet, H_2 5% / Ar / dry, H_2 10% / Ar / dry.
- *Stability in electrode attachment conditions*: for both materials the researched XRD trace has been recovered rising temperatures to 1200°C for 6 hours with a pretreatment to remove possible carbonates at 800°C in air.
- *Stability in electrical contacts attachment*: for both materials the researched XRD trace has been maintained applying 600°C in air, without the possibility of a secondary retreatment in synthesis conditions.
- *Stability with electrolyte material BCY10*: for BSFM the researched XRD traces have been maintained during the compatibility test. It consists in mixing the two components and mortar pestle the mixture, then apply all the conditions previously described that the two materials must encounter during the production process of the device, ideally maintaining both perovskite structures.

  In *Figure 3-9* the X-Ray diffraction pattern is reported for BSFM/BCY10 and it is possible to appreciate the positive results of the test by simply matching displayed reflexes.

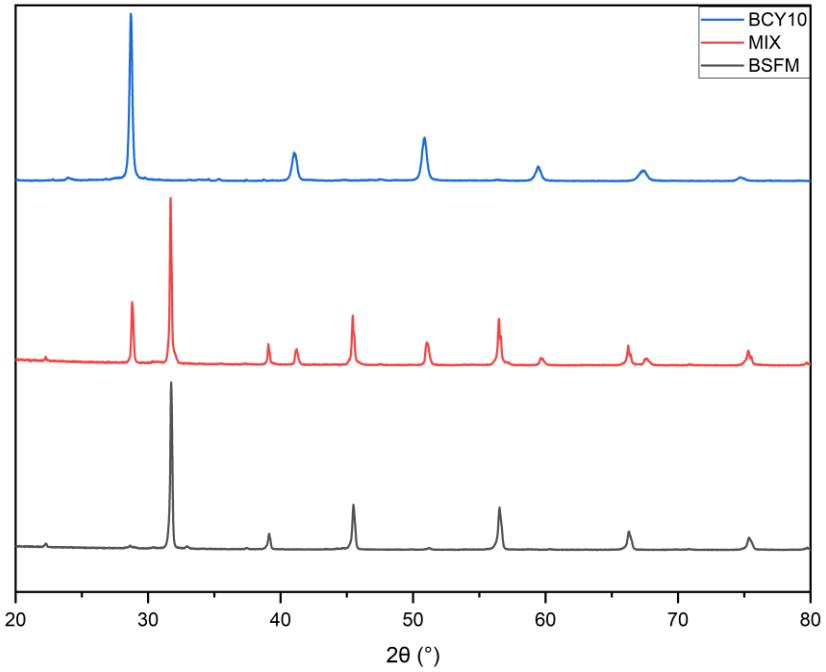

Figure 3-9 XRD Trace comparison of BSFM and BCY10 with the collected diffractogram of the test.

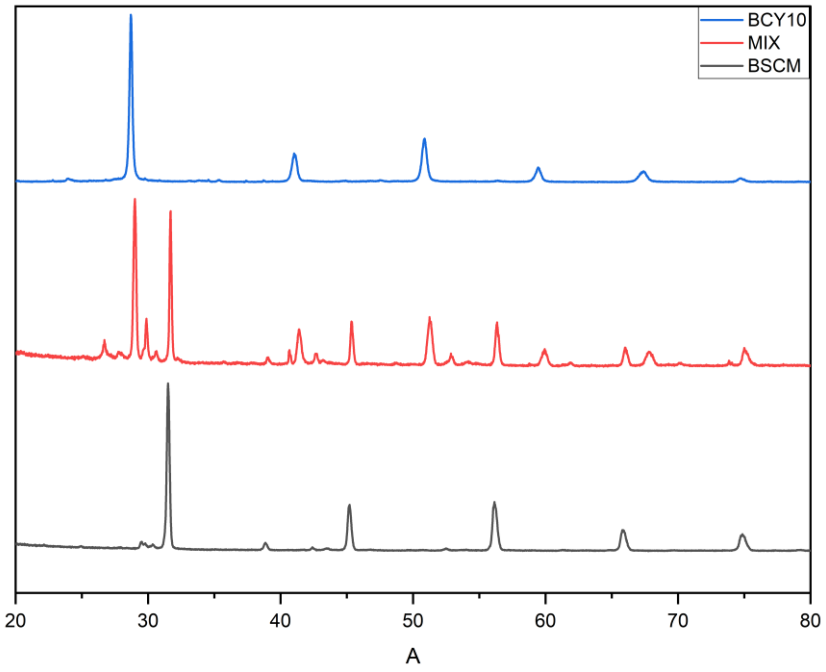

Figure 3-10 XRD Trace comparison of BSCM and BCY10 with the collected diffractogram of the test.

On the other hand, BSCM present a sufficient but not perfect stability with the electrolyte material, demonstrated by the XRD diffractogram presenting reflexes attributed to $BaMoO_x$ oxides. This result is assigned to the more than three times higher molybdenum stoichiometric quantity between the two materials. This difference combined with the high barium presence leads to the formation of these thermodynamically stables oxides[11] during intensive and closely spaced temperature tests. The results are very promising for BSFM which reports properties hard to obtain for a multiple doped double perovskite structure[16], whereas BSCM present a more instable structure, but with tolerable deviations from the ideal case presenting regardless most of the researched properties.

3.4 Scanning Electrons Microscopy (SEM)

To further characterise final device properties, important factors are the porosity and morphology of the two materials. The evaluation of these properties has been carried out through the scanning electrons microscopy technique, with the *Zeiss SUPRA 35VP* device.

The samples powders are compared as follows, and in the case of BSFM literature comparison is presented for a better description. In *Figure 3-11* All images at 5k, 10k and 25k magnifications are reported after the temperature treatment at 1200°C to display the effective morphology once the device is manufactured. Both powders possess strongly connected grains, but different grain boundaries surfaces, a clearer one is presented by BSFM and higher grade of porosity is displayed compared to literature.[17]

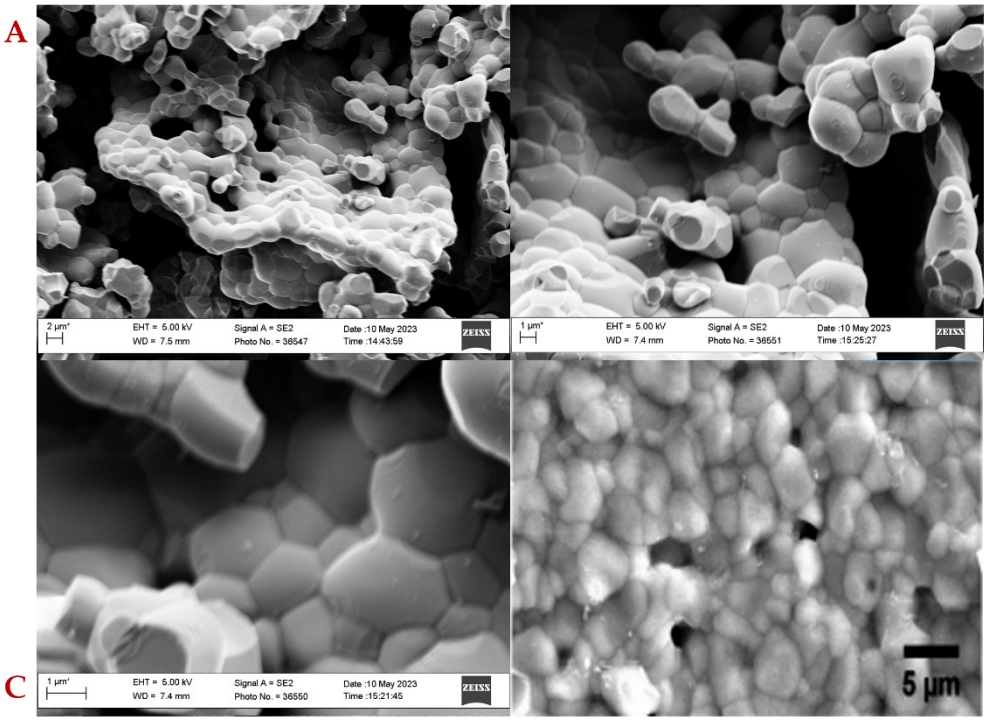

Figure 3-11 SEM images of BSFM (A) 5k magnification, (B) 10k magnification, (C) 25k magnification, (D) literature comparison with $Ba_{1.6}Sr_{0.4}FeMoO_6$.[16]

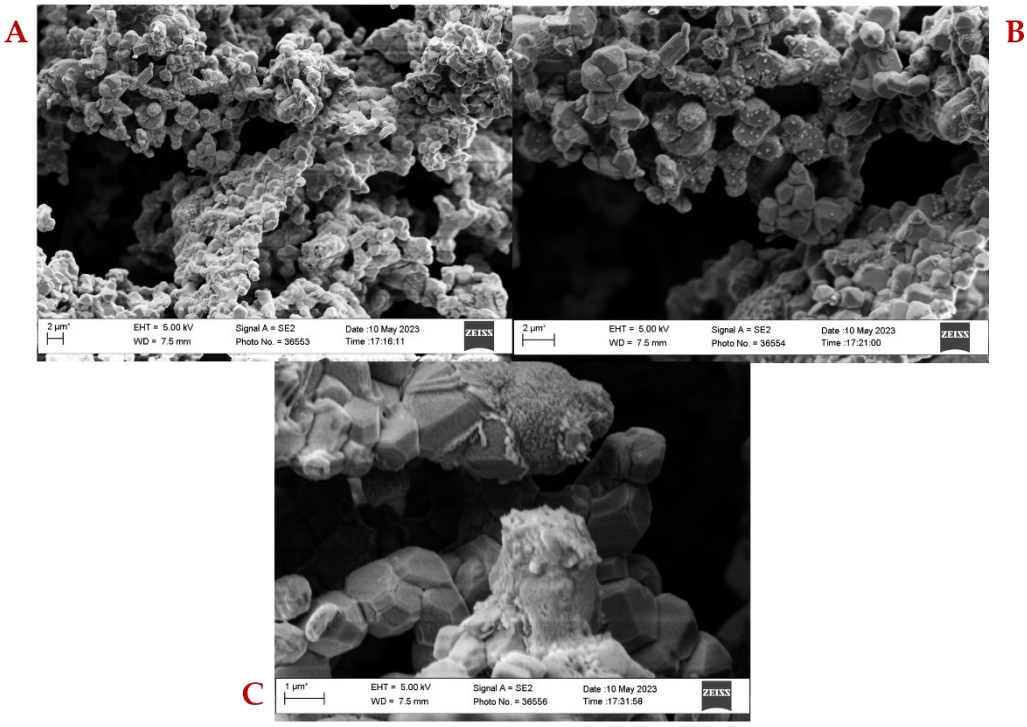

Figure 3-12 SEM images of BSFM (A) 5k magnification, (B) 10k magnification, (C) 25k magnification.

3.5 X-Ray Photoelectron Spectroscopy (XPS)

In order to evaluate composition and surface/bulk differences the X-ray photoelectron spectroscopy has been carried out on both sample's powders. The technique was performed using a monochromatized Al Kα source (hν=1486.68 eV) and a charge compensation gun. Survey spectra were acquired at 100 eV pass energy, 0.5 eV/step and 25 ms/step dwell time. Elemental quantification was carried by the integration of the photopeaks, with the Avantage software after Shirley-type background subtraction.

This technique allows to evaluate composition of the most outer layers of the samples thanks to the photoelectric effect, in which high monoenergetic photons (>1000 eV) are emitted by an X-Ray source stimulating photoemission of electrons from the sample that are collected, measured the kinetic energy (KE) and correlated to the respective binding energy of the atomic orbital from which the electron is emitted (BE) as:

$$KE = h\nu - BE - \varphi_s \qquad (3\text{-}1)$$

Where φ_s is the working function of the spectrometer.

Since not every electron photoemitted by the sample reach the collector, the technique does not analyse the full penetration depth (10 μm) of the X radiation. The fraction of electrons that effectively reach the collector is originating in the rage 1-10 nm, reason why XPS is a surface analysis technique.

Removing negative charged electrons from the sample can lead to the formation of a positively charged surface, which increase the binding energy of subsequent electrons removal, compromising binding energy calculation. For this reason, a reference signal with known binding energy

is needed in every sample, defined as the internal standard, in this case the orbital 1s of carbon situated at 285 eV. This parameter allows the correction of every spectrum to the reference permitting the correct analysis.

In the following paragraphs the technique is first used for a quantitative analysis of the surface, compared with a quantitative analysis of the bulk provided by EDX. The subsequent qualitative analysis is used to describe the catalytic potentiality of the analysed materials, by a comparison made in both paragraph between the sample powders pre and post temperature treatment in SOEC working atmosphere.

3.5.1 Quantitative Analysis

Elemental quantification data reported for surface analysis are calculated by integration of photopeaks analysed from electron emission stimulated by X-rays. Whereas Energy Dispersive X-Ray analysis (EDX) consist of X-Ray emission detection of the elements in the sample after stimulation by high energy electron beam, so XPS and EDX are regarded as complementary techniques. Considering that each element possesses its own X-Ray spectrum, is possible to identify elements in the sample by kinetic energy measurement and quantify them by number of counts, but the investigation penetration depth is different because for EDX it is widened from the 1-10 nm of XPS to the micrometre range. In *Table 3-1* atomic composition are presented, allowing to evaluate segregation phenomena and surface changes pre and post a temperature programmed test, in which the powder samples have been exposed to a 30% H_2 / 70% N_2 atmosphere for one hour every 50°C, in a range from 300 to 600°C,

replicating the expected working conditions for SOEC mode. The post treatment samples are, for this reason, named PT.

BSCM		**Ba**	**Sr**	**Co**	**Fe**	**Mo**	**O**
Complete	Nominal	10	10	2	-	18	60
	EDX	9.00	7.24	1.99	-	13.55	68.24
	XPS	7.46	7.33	0.94	-	9.06	75.21
Cations	Nominal	25	25	5	-	45	-
	EDX	28.32	22.77	6.26	-	42.64	-
	XPS	30.09	29.57	3.79	-	36.55	-
BSCM_PT							
Complete	Nominal	10	10	2	-	18	60
	XPS	9.38	9.02	0.56	-	7.76	73.18
Cations	Nominal	25	25	5	-	45	-
	XPS	34.98	33.64	2.08	-	29.3	-
BSFM							
Complete	Nominal	10	10	-	15	5	60
	EDX	10.27	8.25	-	15.20	4.06	62.22
	XPS	5.72	6.63	-	6.79	3.93	76.93
Cations	Nominal	25	25	-	37.5	12.5	-
	EDX	27.19	21.85	-	40.23	10.74	-
	XPS	24.80	28.74	-	29.42	17.05	-
BSFM_PT							
Complete	Nominal	10	10	-	15	5	60
	XPS	8.92	5.4	-	5.9	5.11	74.67
Cations	Nominal	25	25	-	37.5	12.5	-
	XPS	35.22	21.30	-	23.3	20.18	-

Table 3-1 Reported atomic % composition for each element in both samples, pre and post treatment (PT). All compositions are reported in complete structure percentage and only cations percentage for further comparisons.

The Nominal/EDX/XPS comparison are reported for both samples before the atmosphere temperature treatment, whereas for post treatment only the XPS resulted of interest since no bulk modification are reported in the range of temperatures applied during the process.

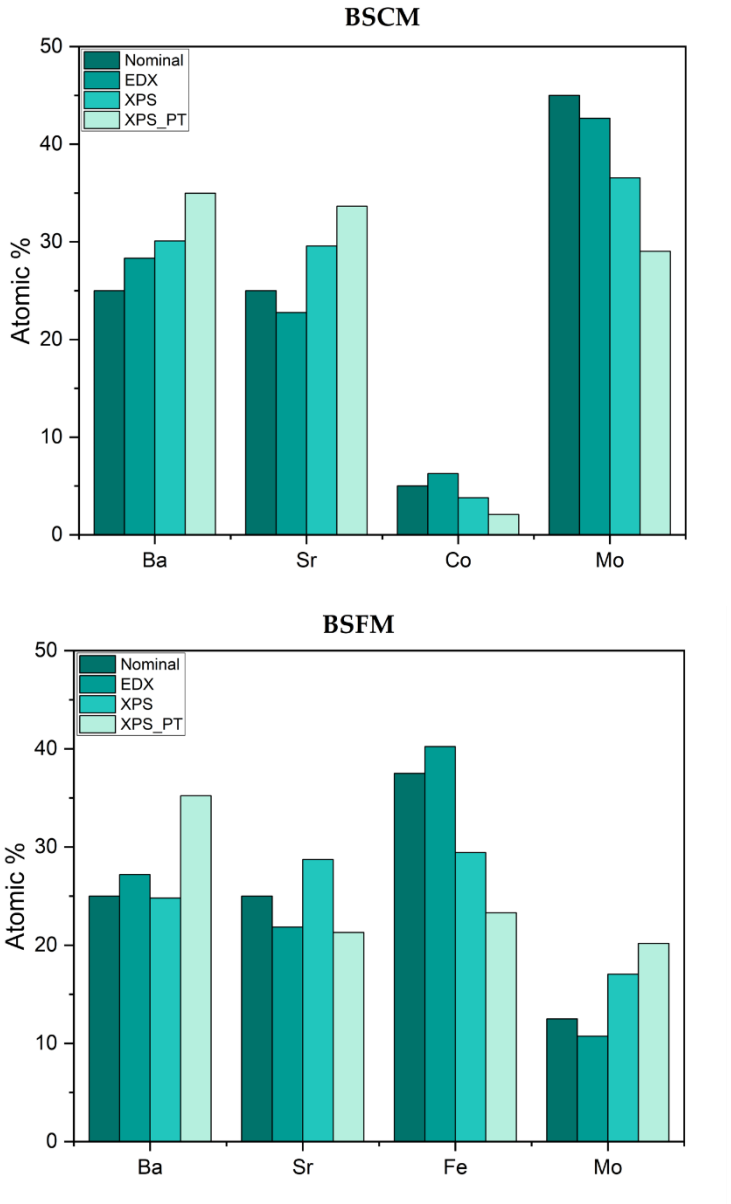

Figure 3-13 Histograms of cationic percentage composition pre and post treatment.

Cationic percentages histograms are also reported for an easier visual comparison in *Figure 3-13*. Oxygen exclusion allows a more precise

structure composition comparison, because it gives higher values in surface quantifications both for surface adsorption and its presence in adventitious carbon. The limitations for the determination of the low-Z elements in EDX analysis, takes place mainly because the beryllium window in an energy-dispersive detector hinders the detection of the characteristic X-rays from light elements.[18]

It is possible to appreciate as EDX percentage values are similar to the nominal ones, differing by values correspondent to a tolerable error, for both BSCM and BSFM powders. Similar are also the quantitative XPS analysis, presenting considerable percentage differences mainly for the stoichiometric higher B metal in both cases, which, as expected, is less measured in surface, due to larger A cations segregation. This phenomenon has been frequently observed in perovskites-based oxides and is considered an atomic rearrangement due to larger ionic radius of A cations also described as surface termination (*Figure 3-14*)[19].

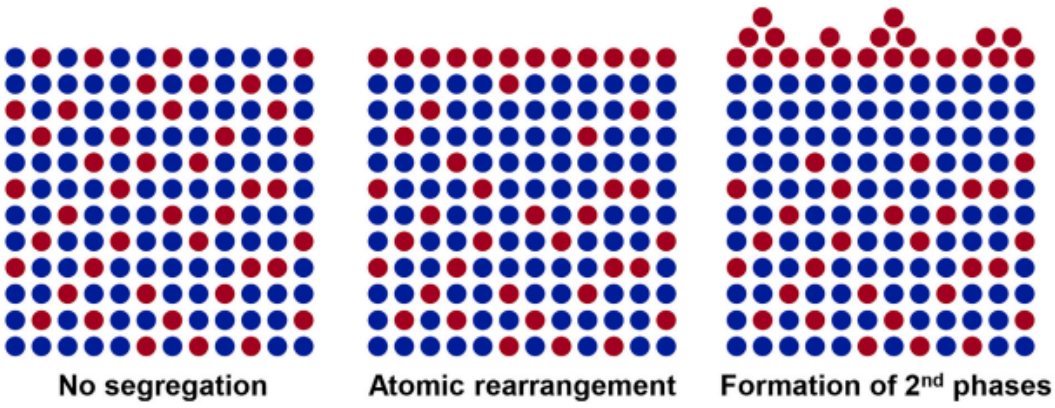

Figure 3-14 Schematic images of surface cation segregation processes[19].

For the same reason the temperature treatment results in a further surface annealing causing the competition between A-site cation and B-site cation and the A cation accumulates over the solubility limit causing phase

separation with consequent cluster creation of secondary phases (Figure 3-14).[19]

These secondary phases are supposed to be different between the two powders. In BSCM the probable secondary phase is a mixture of Sr and Ba oxides since both A cations increment and B cations decrement is measured. Co quantification has been carried out with the Co3s (102 eV) photopeak because the standard one (Co2p) possesses a strong overlap with Ba3d.[20]

On the other hand, BSFM presents percentage increases in Ba and Mo and lower values of Fe and Sr. For this reason, even if the phase separation takes place in both cases, for BSFM the secondary phase created is supposed to be a $BaMoO_x$ mixture since, as already described, they are the most thermodynamically stable phases once the precursor elements separate from the synthetized structure. In fact, the TPR analysis, as well as the XRD pattern of the sample prepared through the synthesis carried out with dry hydrogen atmosphere, underlines that the overall perovskite structure undergoes a degradation process, probably due to Fe reduction. This reduction may lead to a migration of iron cations inside the bulk, leaving behind the Ba and Mo cations which perform phase transition as just described.

3.5.2 Qualitative Analysis of N_2 Adsorption

The photopeaks measured in X-ray photoelectron spectroscopy have also been used for an initial characterization of the produced powders as catalyst for ammonia synthesis.

The just described measurement has been carried out through comparisons considerations between pre and post treatment powders, and

following in a critic way the assumptions that Fe metal is responsible for the absorption of nitrogen on the catalyst surface, considering its catalytic function in Haber Bosch process and its prevalence in the FeMo cofactor of the nitrogenase enzyme.

At first BSCM has been analysed, expecting no N_2 presence if the metal responsible for the nitrogen adsorption is Fe.

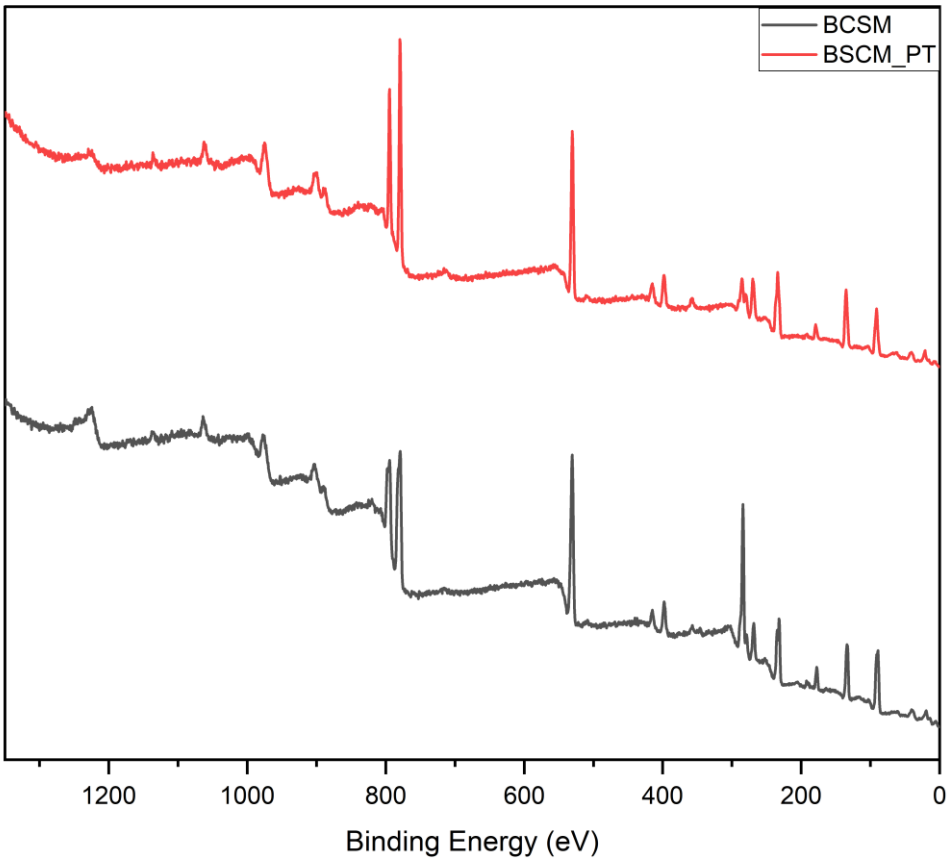

Figure 3-15 Extended XPS spectra for pre and post treatment BSCM.

In Figure 3-11 the XPS survey spectra (wide range) are displayed and the main peaks for each element have been highlighted. Due to the spin-orbital coupling, if the atomic levels possess a quantic number $l > 0$, it is

possible to observe the appearance of doublets in the XPS spectra, like for example the Ba peaks at 780 eV.

The photopeak responsible for nitrogen quantification comes from electrons extraction at binding energies of ~397 eV, but the detection and especially the quantification of adsorption resulted harder than expected because a complete overlap is measured with Mo3p peak.

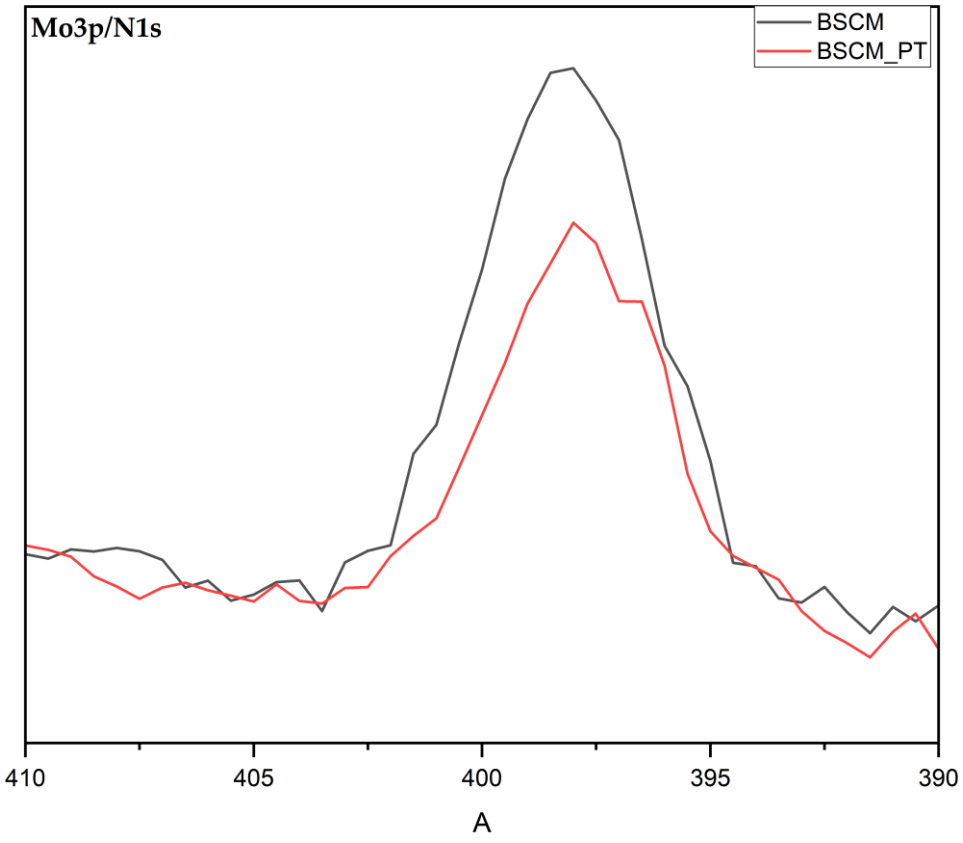

Figure 3-16 BSCM XPS Multiplex spectra of Mo3p/N1s compared pre and post treatment (PT).

As shown in Figure *3-16*, BSCM reports the opposite of the researched results for N_2 adsorption, because the reported peak decreases after atmosphere/temperature treatment (H_2 / N_2 / dry). This is coherent with the

described assumption of Fe being the responsible for the process but retrieves rather unpromising results for the ammonia synthesis process.

These results are anyway useful to further support the different behaviour of BSFM.

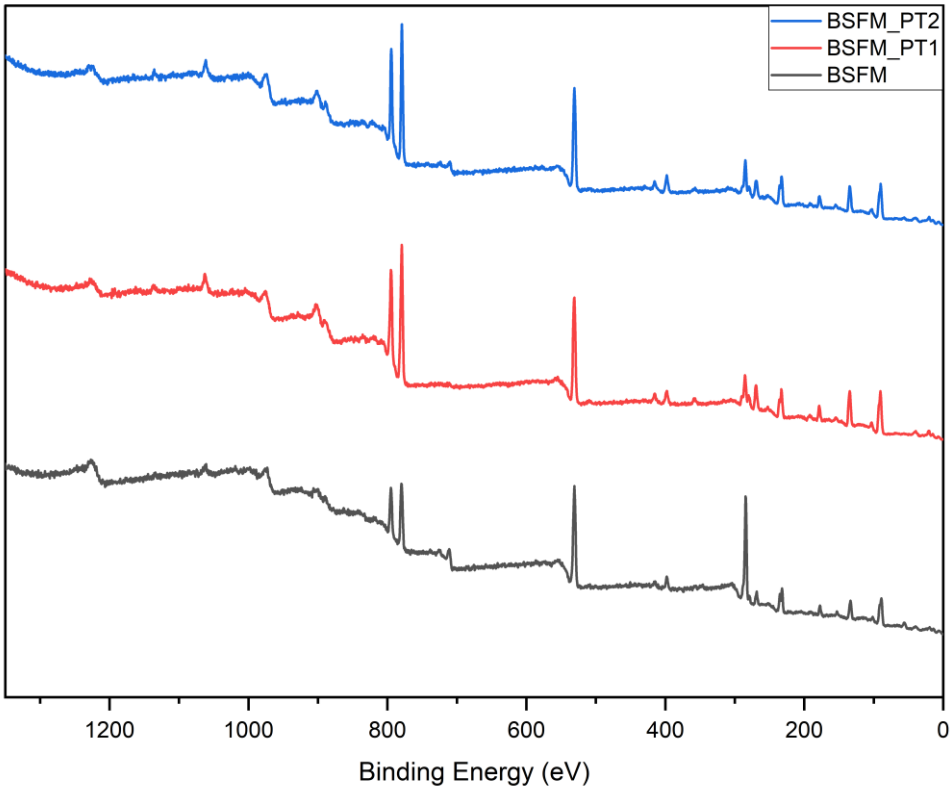

Figure 3-17 Extended XPS spectra of BSFM pre-treatment (black) and two times repeated post treatment (red-blue).

In this case the post treatment XPS analysis has been repeated because the Fe cation was not detected in the first measure. The absence of the primary photopeak of iron (*Figure 3-18*) after treatment may be due to the process of from surface to bulk migration, as described in the previous paragraph. In the second collected spectra the Fe, even if in low percentages,

has been detected and this discrepancy between the two surveys led to a probable phenomenon explanation regarding nitrogen adsorption.

Considering the XPS differences in the multiplex peaks of the composition elements:

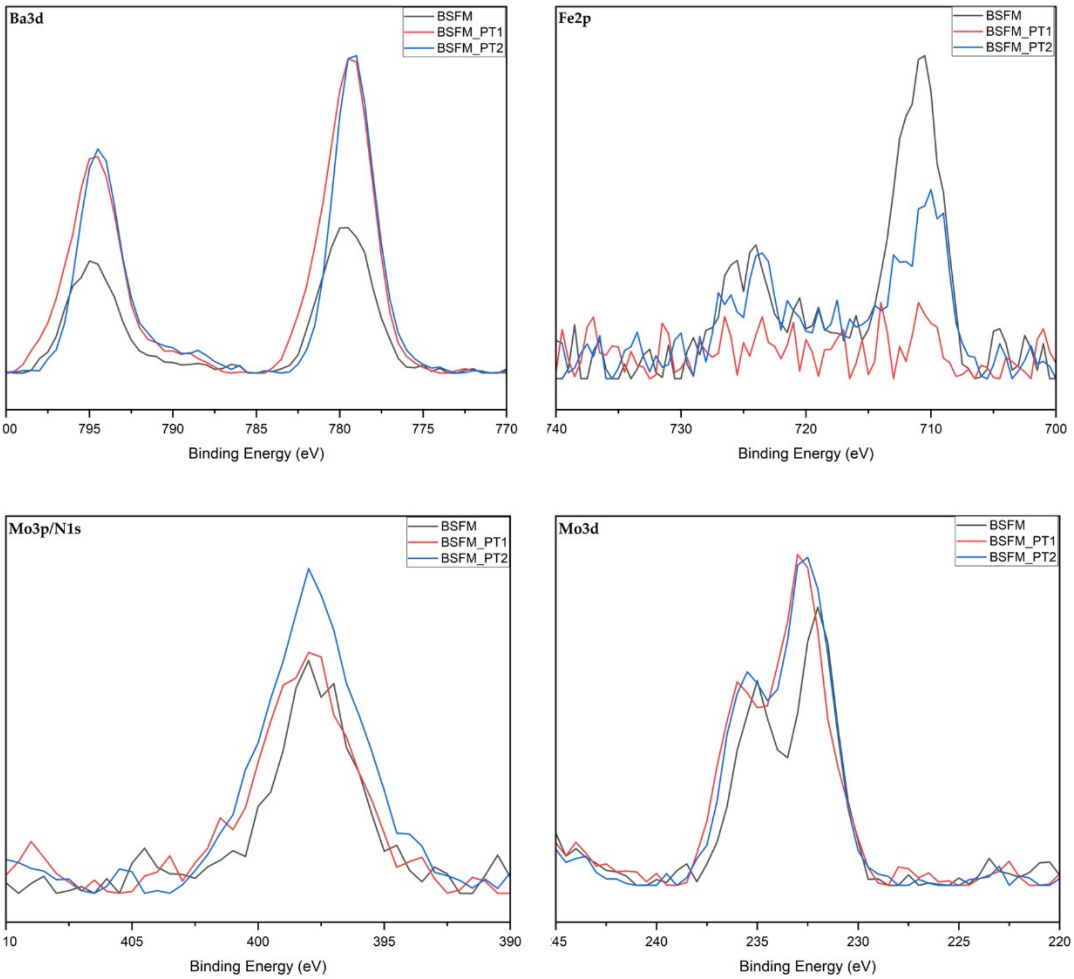

Figure 3-18 BSFM multiplex comparison between main elements peaks of pre and two post treatment analysis.

The Fe2p peak in Figure 3-18 shows the iron peak clearly missing in the red line. But, as it emerges from a comparison between the red and blue line (i.e., the post treatment ones); the peak position is in agreement with Fe(III) in oxides. Ba is in the position characteristic of Ba(II) in oxides whereas Mo 3d peaks shift toward higher Binding Energies after the

treatment; this shift suggests that a more oxygen rich environment is generated by the thermal process. In both cases it is possible to observe the process consisting of Ba and Mo surface segregation by thermodynamic secondary phase cluster formation; in fact, both the Ba3d and Mo3d peaks increase subsequently to the treatment. On the other hand, interesting considerations emerge by looking at the Mo3p peak, which overlaps with the N1s one. It is possible to observe a small area percentage increase in the red line, coherently with the increase in the Mo3d region, but a much higher area increment in the blue line, the one with the recorded presence of surficial Fe. The N1s peak position suggests the presence of ammonia-like nitrogen.

To sum up:

- The area increment of Mo in the 3d region is the same in both post reaction samples.
- Within the possible elements in the sample no other peaks retrieve a signal inside that binding energy range, besides N1s tabulated from metal nitrides.
- The only other measured difference between red and blue line is superficial iron.

For these reasons it is safe to assume that the 22% area increase in the Mo3p/N1s peak can be assigned to nitrogen adsorbed on the surface, probably thanks to the Fe presence on the sample, as stated previously.

With these considerations in mind, it is possible to effectively define this material as a suitable catalyst for ammonia synthesis.

3.5 References

(1) *IMPACT - Wet chemistry procedures for oxide deposition*. https://wwwdisc.chimica.unipd.it/impact/wetchemistry.html.

(2) Dimesso, L. Pechini Processes: An Alternate Approach of the Sol-Gel Method, Preparation, Properties, and Applications. In *Handbook of Sol-Gel Science and Technology*; Klein, L., Aparicio, M., Jitianu, A., Eds.; Springer International Publishing: Cham, 2018; pp 1067–1088. https://doi.org/10.1007/978-3-319-32101-1_123.

(3) Huízar-Félix, A. M.; Hernández, T.; De La Parra, S.; Ibarra, J.; Kharisov, B. Sol–Gel Based Pechini Method Synthesis and Characterization of $Sm_{1-x}Ca_xFeO_3$ Perovskite $0.1 \leq x \leq 0.5$. *Powder Technol.* **2012**, *229*, 290–293. https://doi.org/10.1016/j.powtec.2012.06.057.

(4) Zapata-Ramírez, V.; Mather, G. C.; Azcondo, M. T.; Amador, U.; Pérez-Coll, D. Electrical and Electrochemical Properties of the $Sr(Fe,Co,Mo)O_{3-\delta}$ System as Air Electrode for Reversible Solid Oxide Cells. *J. Power Sources* **2019**, *437*, 226895. https://doi.org/10.1016/j.jpowsour.2019.226895.

(5) *Sol–Gel Processing*. Ebrary. https://ebrary.net/191957/engineering/sol_gel_processing.

(6) Moritomo, Y.; Xu, Sh.; Machida, A.; Akimoto, T.; Nishibori, E.; Takata, M.; Sakata, M. Electronic Structure of Double-Perovskite Transition-Metal Oxides. *Phys. Rev. B* **2000**, *61* (12), R7827–R7830. https://doi.org/10.1103/PhysRevB.61.R7827.

(7) *Shannon Radii*. http://abulafia.mt.ic.ac.uk/shannon/ptable.php

(8) Carollo, G.; Garbujo, A.; Mauvy, F.; Glisenti, A. Critical Raw Material-Free Catalysts and Electrocatalysts: Complementary Strategies to

Activate Economic, Robust, and Ecofriendly $SrTiO_3$. *Energy Fuels* **2020**, *34* (9), 11438–11448. https://doi.org/10.1021/acs.energyfuels.0c01678.

(9) Nolze, D. G. PowderCell: A Mixture between Crystal Structure Visualizer, Simulation and Refinement Tool.

(10) Wright, J. H.; Virkar, A. V.; Liu, Q.; Chen, F. Electrical Characterization and Water Sensitivity of $Sr_2Fe_{1.5}Mo_{0.5}O_{6-\delta}$ as a Possible Solid Oxide Fuel Cell Electrode. *J. Power Sources* **2013**, *237*, 13–18. https://doi.org/10.1016/j.jpowsour.2013.02.079.

(11) N. K. Shukla; Rajendra Prasad; D. D. Sood. The Standard Molar Enthalpies of Formation at the Temperature T=298.15 K of Barium Molybdate and Strontium Molybdate, 1993.

(12) Xiao, G.; Liu, Q.; Wang, S.; Komvokis, V. G.; Amiridis, M. D.; Heyden, A.; Ma, S.; Chen, F. Synthesis and Characterization of Mo-Doped $SrFeO_{3-\delta}$ as Cathode Materials for Solid Oxide Fuel Cells. *J. Power Sources* **2012**, *202*, 63–69. https://doi.org/10.1016/j.jpowsour.2011.11.021.

(13) Tavizón-Pozos, J. A.; Santolalla-Vargas, C. E.; Valdés-Martínez, O. U.; De Los Reyes Heredia, J. A. Effect of Metal Loading in Unpromoted and Promoted $CoMo/Al_2O_3–TiO_2$ Catalysts for the Hydrodeoxygenation of Phenol. *Catalysts* **2019**, *9* (6), 550. https://doi.org/10.3390/catal9060550.

(14) Xi, X.; Liu, J.; Fan, Y.; Wang, L.; Li, J.; Li, M.; Luo, J.-L.; Fu, X.-Z. Reducing D-p Band Coupling to Enhance CO_2 Electrocatalytic Activity by Mg-Doping in $Sr_2FeMoO_{6-\delta}$ Double Perovskite for High Performance Solid Oxide Electrolysis Cells. *Nano Energy* **2021**, *82*, 105707. https://doi.org/10.1016/j.nanoen.2020.105707.

(15) Mohd Affandi, N. S.; Osman, N. Short Review on Global Trends in SOFC Scenario and Future Perspective. *Mater. Today Proc.* **2022**, *66*, 3981–3984. https://doi.org/10.1016/j.matpr.2022.04.824.

(16) Wolf, S. E.; Winterhalder, F. E.; Vibhu, V.; De Haart, L. G. J. (Bert); Guillon, O.; Eichel, R.-A.; Menzler, N. H. Solid Oxide Electrolysis Cells – Current Material Development and Industrial Application. *J. Mater. Chem. A* **2023**, *11* (34), 17977–18028. https://doi.org/10.1039/D3TA02161K.

(17) Hussain, I.; Anwar, M. S.; Khan, S. N.; Shahee, A.; Ur Rehman, Z.; Heun Koo, B. Magnetocaloric Effect and Magnetic Properties of the Isovalent Sr^{2+} Substituted Ba_2FeMoO_6 Double Perovskite. *Ceram. Int.* **2017**, *43* (13), 10080–10088. https://doi.org/10.1016/j.ceramint.2017.05.027.

(18) Ro, C.-U.; Osán, J.; Van Grieken, R. Determination of Low- *Z* Elements in Individual Environmental Particles Using Windowless EPMA. *Anal. Chem.* **1999**, *71* (8), 1521–1528. https://doi.org/10.1021/ac981070f.

(19) Koo, B.; Kim, K.; Kim, J. K.; Kwon, H.; Han, J. W.; Jung, W. Sr Segregation in Perovskite Oxides: Why It Happens and How It Exists. *Joule* **2018**, *2* (8), 1476–1499. https://doi.org/10.1016/j.joule.2018.07.016.

(20) *Cobalt | Periodic Table - IT*. https://www.thermofisher.com/uk/en/home/materials-science/learning-center/periodic-table/transition-metal/cobalt.html.

4. CELLs DESIGN AND PERFORMANCE

This chapter delineates the essential methodologies employed for manufacturing a planar design of a solid oxide cell. Subsequently, the performance evaluation of symmetrical cells is discussed, culminating in the examination of electrochemical effectiveness in ammonia synthesis.

4.1 Cells Manufacturing Process

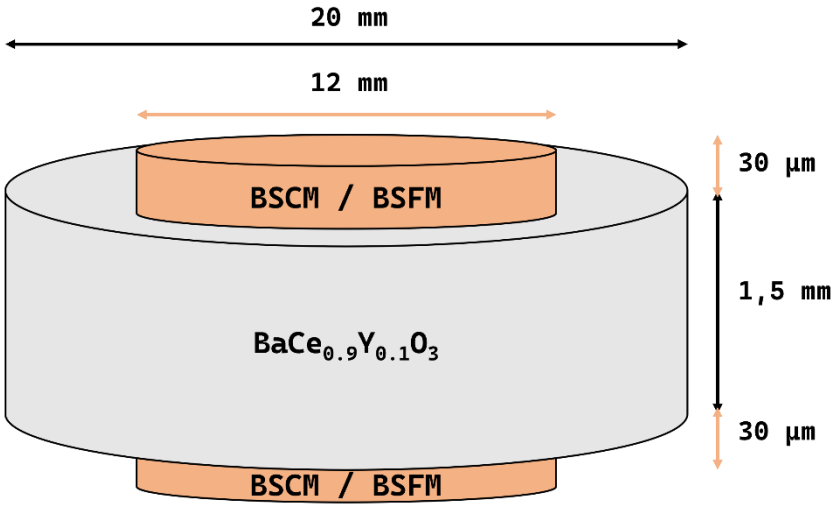

Figure 4-1 Symmetric cell design of the used button cells.

The chosen design for the planar cells tested is the button electrolyte supported (*Figure 4-1*), realized due to the simplicity of the crafting process and to have a mechanically stable device able to fit in the used setup for electrocatalytic measurement.

The first step for the crafting process is the electrolyte preparation. 2.0 g of BCY10 powder are compressed with manual pressing to 4.5 tons for 5

minutes. The so created pellet is then thermally treated at 1500°C for 6 hours to obtain a denser component by the sintering effect, therefore more resistant and with closed porosities blocking gas diffusion through it.

With this procedure the button is crafted allowing the last step of surface polishing with grid sandpaper, with subsequent ethanol washing in ultrasonic bath. Electrolyte surfaces optimization is one of the main characteristics influencing the proton conductivity since the area of superficial interaction with the electrode is one of the limiting parameters of the process.[1] Following this path the manufactured button electrolyte presents the dimensions of 20mm diameter and 1.5mm thickness.

Electrode deposition over the electrolyte have been carried out through tape casting. Being well known that SOCs performance is affected by the structure of the electrode, is very important to provide a good overall porosity and structure of the pores using carbon-based pyrolyzable pore formers.[2] To achieve the porosity with good and malleable fluid for depositions, an ink has been prepared for both BSCM and BSFM materials. A good ink deposition composition is achieved with a powder mixture of 60% BSCM/BSFM and 40% of BCY10, the weight of this mixture is then used to balance the carbon polymers addition. In a mortar the powders have been pestled with 3% wt carbon-soot to regulate porosity, then these solid phases are dispersed in a liquid medium, and the viscosity is controlled by incorporating two α-terpineol polymers (50% wt).

Both materials' ink so prepared are deposited via tape casting on the electrolyte button, with masks of 12 mm diameter and ~30 μm thickness. The so attached component must now face a temperature treatment to 1200°C, ideally air to remove the carbon components in a single step. Because both BSCM and BSFM does not retrieve the researched structure in

air, a pretreatment to remove carbons has been carried out at 800°C air, followed by the structure recovery and attachment treatment at 1200°C for 6 hours in 10% H_2 / Ar / dry for BSCM and 5% H_2 / Ar / wet for BSFM, technique effectiveness already tested with X-Ray diffractograms.

Electronic contacts are attached with a gold paste thin film covering the whole electrode, to help electron collection and supply all over the catalytic area. These covering thin films are then linked with a gold wire to the *PGSTAT 302 Autolab Frequency Response Analyser*, device providing cells electronic measurements. Results are displayed in *Figure 4-2* only for BSFM since visually identical.

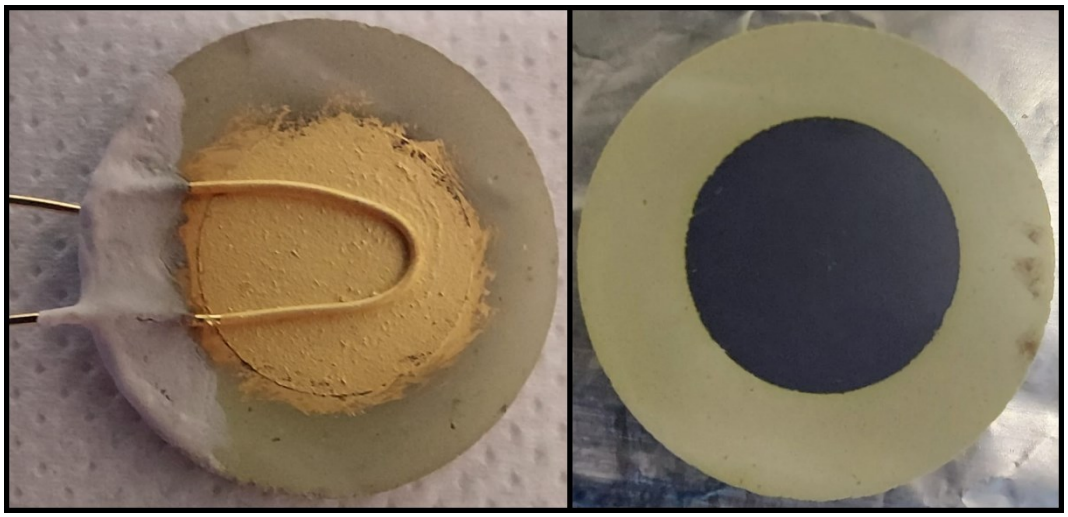

Figure 4-2 Electrolyte supported button cell with electrical contacts (left) and without (right).

4.1.1 Symmetrical and Complete Cell Chamber Setups

For both symmetrical and complete cells, *AISI 316* oven has been employed, a molybdenum alloy with austenitic steel. This oven presents an internal cavity where the chamber and a K-type thermocouple for temperature control are situated.

To perform the two different device mode tests, the setups employed are different. Focussing on the symmetrical chamber configuration, the cell was supported by an *α-alumina DEGUSSIT AL23* tube, enclosed by a quartz tube to isolate the chamber. Fuel injection occurred at the bottom of the chamber, exiting from the top. Platinum wires on the ceramic tube were connected to the golden wires on the cell to establish the current flow pathway (*Figure 4-3(A)*).

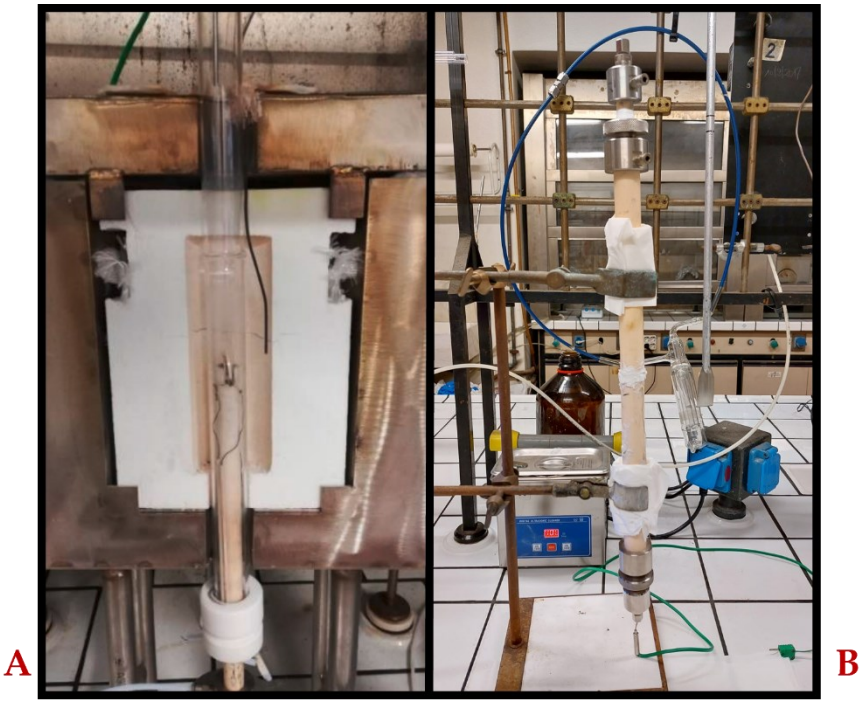

Figure 4-3 (A) Single chamber for symmetrical tests (B) complete chamber for complete cell tests.

In the second configuration, for the complete cell test, a double chamber setup was adopted. From below the cell was supported by concentrical tubes ceramic structure and sealed using alumina-based cement. This sealing step is crucial to separate gas flows for different electrodes and to keep the exhaust inside the chamber for synthesis measurements. Nitrogen atmosphere was introduced internally by the

inner ceramic tube, which also contained a second thermocouple for precise temperature monitoring. Above the cell, particularly above the anode, another concentrical tubes structure was positioned, also sealed on top of the button device, allowing the flow of H_2 / H_2O fuel to the anode side of the cell completing the SOEC device setup requirements (*Figure 4-3 (B)*).

4.2 EIS Theory[3]

Electrochemical Impedance Spectroscopy (EIS) stands out as a widely employed method for defining the electrochemical behaviour of Solid Oxide Fuel Cells (SOFCs). Nevertheless, its complexity arises from its sensitivity to both the cell's configuration and manufacturing processes.

To understand the functioning of Electrochemical Impedance Spectroscopy EIS, it is crucial to revisit the concept of electrical resistance. Electrical resistance is circuit's capacity to impede the passage of electrical current, as defined by Ohm's law (*Equation 4-1*), expressing the ratio between voltage (E) and current (I).

$$R \equiv \frac{E}{I} \tag{4-1}$$

However, this correlation is restricted to ideal resistors. An ideal resistor exhibits several simplifying properties:

- It adheres to Ohm's law irrespective of current and voltage levels.
- It remains independent of frequency variations.
- Voltage and AC current signals are in phase with each other when passing through a resistor.

These limitations are not consistently confirmed; as a result, it is possible to substitute them with a more general circuit parameter, i.e.,

impedance. Impedance can be defined in a manner analogous to electrical resistance but is not constrained by the just listed simplifying properties.

The measurement of Electrochemical Impedance involves applying an AC potential to a cell and subsequently collecting and measuring the current flowing through it. Typically, it is assumed that the excitation potential is sinusoidal, resulting in an AC current signal. The excitation signal is usually small, enabling the cell's response to be treated as pseudo-linear. This pseudo-linear response permits the consideration of the current as a sinusoid at the identical frequency as the sinusoidal potential but with a phase shift (*Figure 4-4*).

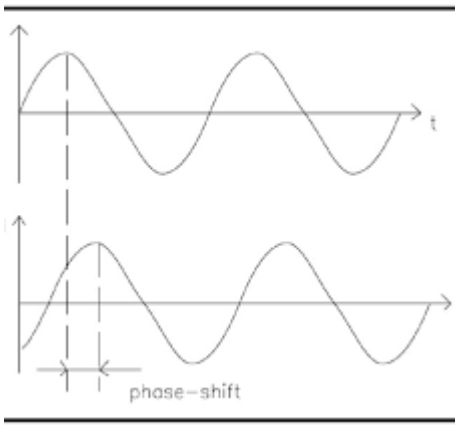

Figure 4-4: Sinusoidal Current Response in a linear system.

It is possible to express the excitation signal as a function of time as:

$$E_t = E_0 sin\,(\omega t)$$

(4-2)

where E_t is the potential at the time t, E_0 is the signal's amplitude, and the radial frequency ω [radians/s] is dependent on the frequency [Hz] as:

$$\omega = 2\pi f$$

(4-3)

In a linear system, the response signal I_t can be expressed as:

$$I_t = I_0 sin\,(\omega t + \phi)$$

(4-4)

where I_0 is its amplitude and ϕ the phase shift. The ratio of the excitation signal to the response signal, in analogy to the Ohm's law, enables the determination of the system's impedance Z:

$$Z = \frac{E_t}{I_t} = \frac{E_0 sin\,(\omega t)}{I_0 sin\,(\omega t + \phi)} = Z_0 \frac{sin\,(\omega t)}{sin\,(\omega t + \phi)}$$

(4-5)

Here, Z_0 denotes the magnitude and ϕ the phase shift.

Graphing the sinusoidal applied signal against the sinusoidal response signal allows the generation of the widely recognized 'Lissajous Figure', shown in *Figure 4-5*. This figure takes the form of an oval and analysing it on the oscilloscope screen has traditionally served as the established approach for impedance calculation before the advent of modern Electrochemical Impedance Spectroscopy (EIS) instrumentation.

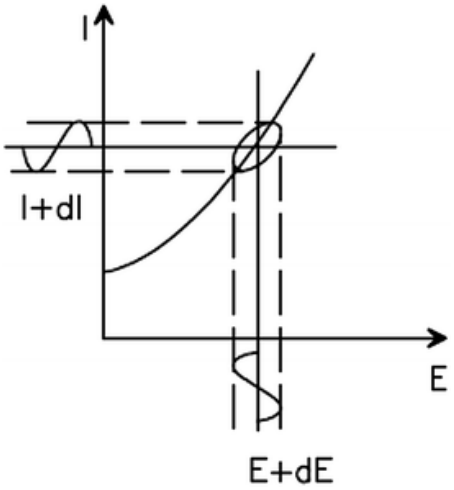

Figure 4-5: Typical Lissajous Figure.

Considering the Euler's relationship:

$$exp\,(j\phi) = cos\phi + jsin\phi$$

(4-6)

it is possible to express the impedance as a complex function, whom potential and current response can be described as:

$$E_t = E_0 exp(j\omega t) \tag{4-7}$$

$$I_t = I_0 exp(j\omega t - \phi) \tag{4-8}$$

The impedance is then a complex number, given by:

$$Z(\omega) = Z_0 exp(j\phi) = Z_0(cos\phi + jsin\phi) \tag{4-9}$$

The Equation 5.9 reveals that the impedance is made by both a real and an imaginary component. Plotting the real part against the imaginary part results in what is known as Nyquist Plot. Each point on this plot represents the impedance at a specific frequency, with data from lower frequencies positioned to the right and data from higher frequencies positioned to the left. *Figure 4-6*[4] below illustrates the characteristic shape of a Nyquist plot.

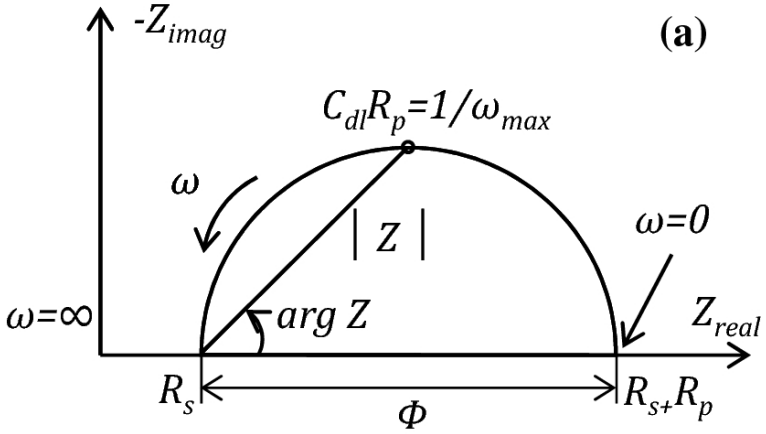

Figure 4-6: Schematic representation of the Nyquist plot[4] *|Z| is the length of the vector that represents the impedance and arg Z represents the phase angle.*

Nonetheless, the frequencies are not readily apparent from this singular plot, and smaller impedances may be hidden by larger ones. As a

result, another plot, known as the Bode plot (*Figure 4-7*), is frequently employed as a data presentation technique. In the Bode plot, impedance is graphed with logarithmic frequency on the X-axis and both the absolute value of the impedance ($|Z| = Z_0$) and the phase shift on the Y-axis. This approach facilitates the resolution of individual charge transfer processes at specific frequencies, and it is particularly effective in distinguishing small impedances even in the presence of larger ones.

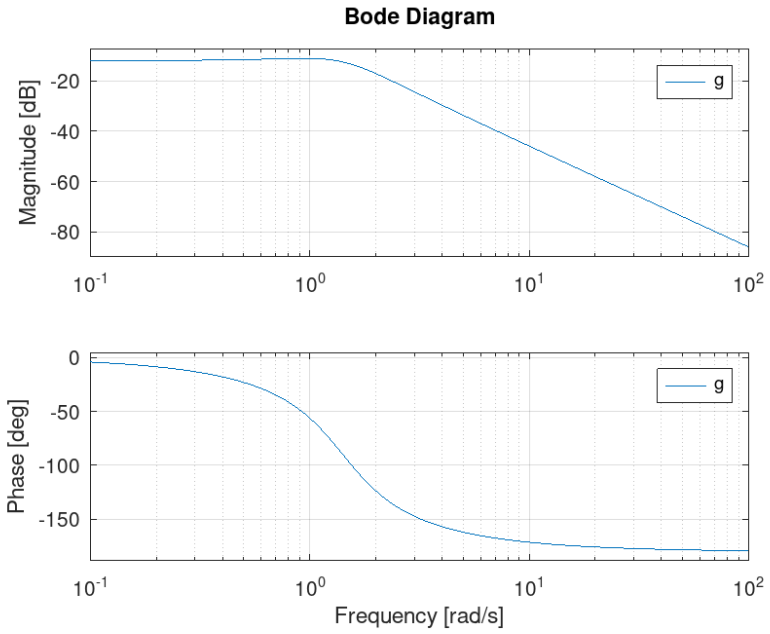

Figure 4-7: Bode plots: impedance magnitude vs frequency (above) and phase angle vs frequency (below)

4.3 Symmetrical cells

EIS results were acquired using the *PGSTAT 302 Autolab Frequency Response Analyzer*. The tests were conducted under steady-state conditions, meaning there was no DC current, within the frequency range of 10^0 to 10^6 Hz, with a signal amplitude of 20 mV.

The Electrochemical Impedance Spectroscopy (EIS) was employed to explore the electrochemical behaviour of the electrode materials under

various operational conditions. Specifically, variations in temperature and fuel type were investigated. The fuels utilized included:

- Hydrogen, to showcase the potential application of these materials as anodic electrodes.
- Ammonia, to illustrate the feasibility of using the same materials in an R-SOC (Reversible Solid Oxide Cell) configuration.
- Nitrogen to validate that these materials are well-suited for cathode applications in an SOEC configuration for ammonia production.

4.3.1 Fitting and modelling

All EIS data were subjected to fitting and analysis using *ZView 4* software. The fitting process allows to distinguish all the various mechanisms and to quantify their resistances through the application of equivalent circuits.

Initially, the first step involved identifying the number of processes by examining both the Nyquist and Bode plots. Once the processes were identified, a circuit was constructed using a resistor (simulating the ohmic resistance of the cell) connected in series with R-CPE subcircuits. The number of R-CPEs corresponds to the number of processes observed in the plots. The decision to use the Constant Phase Element (CPE) instead of a conventional capacitor was based on the fact that capacitors in EIS experiments often deviate from ideal behaviour.[5] Moreover, at low frequencies, it was possible to observe a linear relationship on the log of the Bode plot with a slope value of -1/2. This is the typical behaviour of

diffusion processes, and it is fitted in the equivalent electrical circuit through the use of a component known as the Warburg diffusion element W_s. In general, it is possible to see W_s as a constant phase element (CPE) with a fixed phase of 45° (independent of frequency) and a magnitude which is inversely proportional to the square root of the frequency.

In the following *Figure 4-8* the equivalent circuit used to fit the data in the impedance spectra is reported:

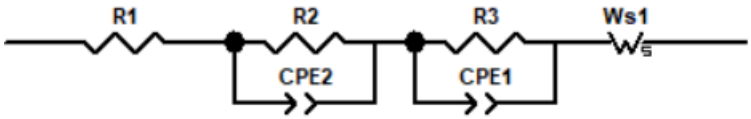

Figure 4-8 Equivalent circuit used in EIS fittings.

The fitting process allowed to obtain resistance values for each individual process, along with the total resistance. To get a comparison with literature results, the area specific resistance (ASR) [$\Omega \cdot cm^2$] was computed for each process using the formula:

$$ASR = \frac{R \cdot A_{electrode}}{2} \tag{4-10}$$

Here, $A_{electrode}$ denotes the area of the circular electrode, calculated from the electrode radius (0.6 mm). The factor of ½ is applied due to the symmetrical cell configuration, where the contributions to resistances originate from both electrodes. Consequently, dividing the ASR value by two accounts for just a single electrode.

Additionally, the fitting process enabled the calculation of capacitance for each process using the formula:

$$C_i = \frac{(R_i \cdot CPET_i)^{CPEP_i}}{R_i} \tag{4-11}$$

Here, R_i signifies the resistance associated with the *i-th* process, while $CPET_i$ and $CPEP_i$ are two parameters obtained from the fit related to the Constant Phase Element. The knowledge of capacitance values facilitates the correlation of each process with the underlying phenomenon responsible for it[6].

Capacitance (F)	Phenomenon Responsible
10^{-12}	Bulk
10^{-11}	Minor, Second phase
$10^{-11} – 10^{-8}$	Grain-boundary
$10^{-10} – 10^{-9}$	Bulk ferroelectric
$10^{-9} – 10^{-7}$	Surface layer
$10^{-7} – 10^{-5}$	Sample-electrode interface
10^{-4}	Electrochemical reaction

Figure 4-9: Suggested phenomenon interpretation from Capacitance values associated to the process.[6]

Finally, the activation energy linked to the overall process for each fuel has been determined. Starting with the conductivity (σ) equation as a function of temperature, and recognizing that ASR = 1/σ, a linear equation can be derived:

$$ln\,(ASR) = \frac{E_a}{k_B T} - ln\,(k_O)$$

(4-12)

Here, T represents the temperature in Kelvin, E_a is the activation energy, and k_B is the Boltzmann constant. Constructing a typical Arrhenius plot by plotting $ln\,(ASR)$ against *1000/T [1/K]* permits to simplify the equation to a linear relationship. By calculating the slope (m) of the line associated with the fitting, the activation energy can be determined through:

$$E_a = m \cdot R \cdot 0.010341$$

(4-13)

In this equation, R is the product of the Avogadro Number and the Boltzmann constant, and the numeric factor is applied to convert the obtained value to electron volts [eV], the most commonly used notation in literature.

4.3.2 BSCM electrochemical characterization

In this section, the performance of BSCM as electrode material will be examined and discussed. As mentioned above, the symmetrical cell tests were conducted in three different atmospheres to explore the influence of different operating conditions. For each gas inlet, the Electrochemical Impedance Spectroscopy spectra were acquired at temperatures ranging from 400°C to 750°C.

The first test consisted utilizing hydrogen as fuel with a flux of 10% wet H_2/Ar 100sccm. The following Figure shows the EIS spectra obtained:

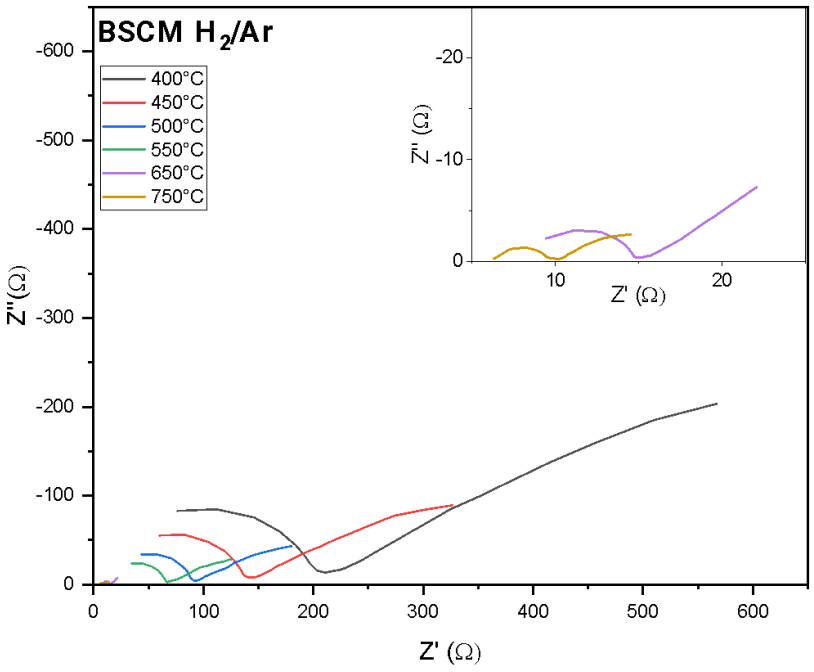

Figure 4-10: EIS cell performance in 10% wet H_2/Ar at various temperatures.

The point where the curve intersects the X-axis at high frequency (left) provides the Ohmic resistance value, representing the resistance of the electrolyte. As expected, the value of it diminishes raising the operating temperature. Moreover, it is clear that the process at lower frequencies attributed to gas-diffusion (the straight line shown on the right) does not close, i.e., it does not intercept with the X-axis. This behaviour is typical of materials containing Mo in high quantities with BCY as electrolyte[1] and its resistance related to the diffusion process is not considered in the overall resistance value.[7] The two processes found at higher frequencies have relative capacities that are in the order of 10^{-8} F and 10^{-3} F; comparing the acquired valued with those in *Figure 4-10* enables the correlation of the first process with the resistance at the surface layer, while the second process seems attributable to electrochemical reactions. More specifically the second process can be linked to charge-transfer reactions, hydrogen oxidation, or the adsorption and desorption of the fuel on the surface.[8,9]

What is clear to see is a big difference in the EIS spectra obtained at 650°C and 750°C in comparison with the ones obtained at lower temperatures. This is probably due to the reduction of the MoO_x, suggested by the data obtained through the H_2-TPR measurement. However, as ammonia synthesis occurs at lower temperatures, the decision was made not to investigate this result. Nonetheless, exploring this further could be intriguing to comprehend the potential suitability of BSCM as an anodic material in SOFC configurations.

Examining the EIS spectra generated using ammonia as a fuel reveals that they exhibit identical processes at the same frequencies as those previously discussed for H_2. The Nyquist plot for the EIS data obtained at the same temperature range is presented in the following *Figure 4-11*:

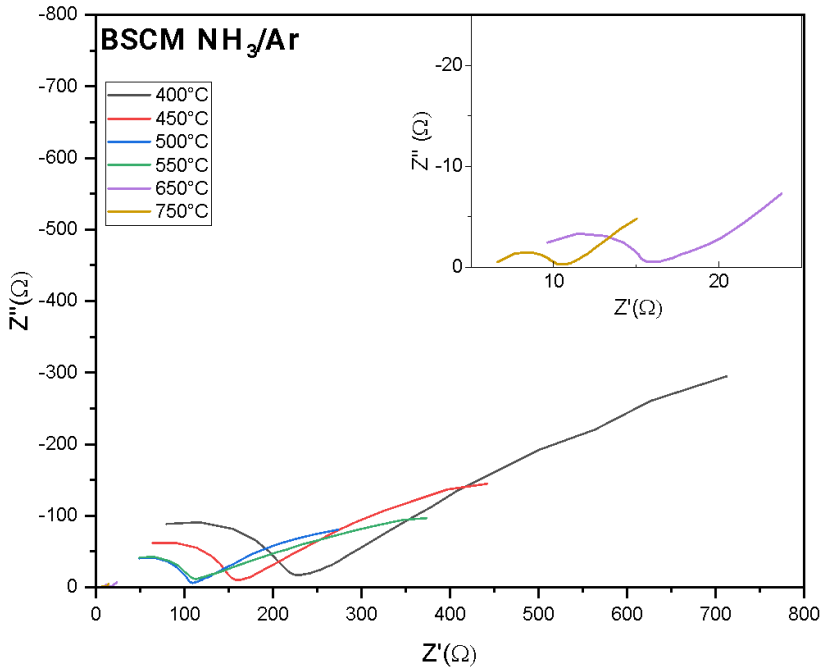

Figure 4-11: EIS cell performance in 10% wet NH_3/Ar at various temperatures.

The behaviour of the cell fuelled with ammonia closely resembles its behaviour when fuelled with hydrogen. Again, what is evident is a significant contrast in the EIS spectra obtained at 650°C and 750°C when compared to those acquired at lower temperatures. The same considerations outlined earlier with hydrogen can be extended to the use of ammonia as fuel. Nevertheless, this opens up the prospect of employing NH_3 as fuel in SOFC configurations.

Finally, BSCM has been tested as a possible candidate for applications as cathode for H-SOEC in ammonia production. In the following *Figure 4-12* the EIS spectra obtained are reported in the temperature range of 450-750°C, since it was not possible to fit the spectra obtained at 400°C, due to the values deriving from the gas-diffusion processes being too high.

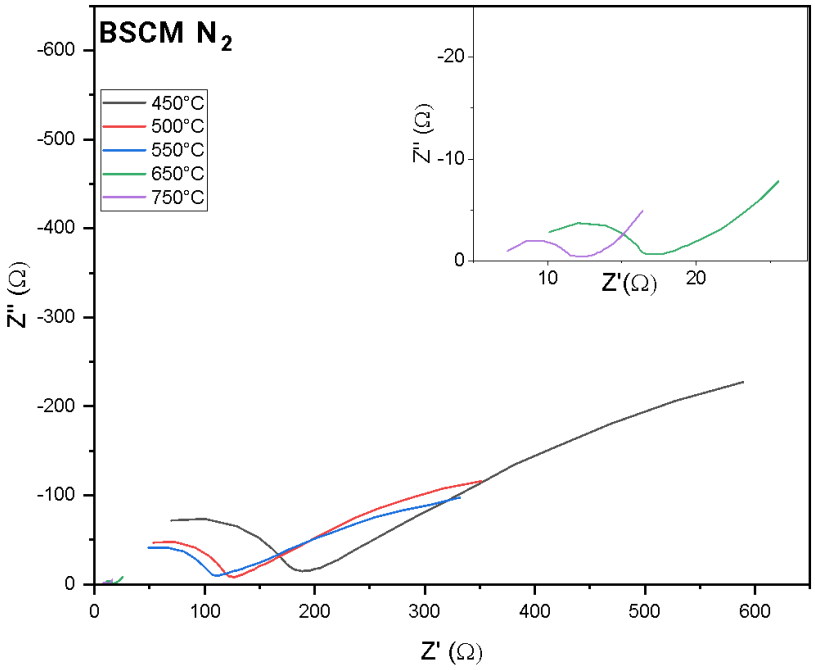

Figure 4-12: EIS cell performance in 100% dry N_2 at various temperatures.

Once more, there is a notable distinction in the EIS spectra recorded at temperature values above 650°C compared to those obtained at lower temperatures. The high values of resistances in the temperature range of ammonia synthesis, however, suggest that this material is not a viable solution for ammonia synthesis via electrochemistry route in H-SOEC mode.

The comprehensive Area Specific Resistance (ASR) has been computed for the three fuels at each temperature, and the outcomes are summed up in *Table 4-1*. The ASR values for all fuels considered decrease with increasing temperature, indicating that the present processes are thermally activated. Furthermore, the ASR values obtained with ammonia compared to those obtained with hydrogen are slightly higher, and this is probably due to decomposition of NH_3, which results in the formation of nitrogen and hydrogen, with N_2 acting as a diluent of the fuel.

Temperature [°C]	750	650	550	500	450	400
ASR [$\Omega \cdot cm^2$] 10% wet H_2/Ar	2.76	4.92	55.34	68.98	134.10	517.21
ASR [$\Omega \cdot cm^2$] 10% wet NH_3/Ar	3.96	8.92	60.65	71.95	157.45	620.76
ASR [$\Omega \cdot cm^2$] 100% dry N_2/Ar	5.49	13.59	83.80	108.95	301.98	-

Table 4-1 ASR calculations for each fuel at each temperature.

As emphasized repeatedly, the only ASR values that have an acceptable significance are the ones obtained at T higher than 650°C. For this reason, it has been determined that this material is not suitable for ammonia synthesis, yet more studies can be done in order to evaluate the possibility of using it as anodic material in H-SOFC.

4.3.3 BSFM Electrochemical Characterization

Following the approach used for BSCM, the electrochemical characterization of BSFM has been assessed for the three distinct fuel gases. The EIS spectra were acquired across the same temperature range of 400°C to 750°C. The initial test involved the use of hydrogen as fuel with a 10% wet H_2/Ar flux at 100sccm. The following *Figure 4-13* displays the obtained EIS spectra.

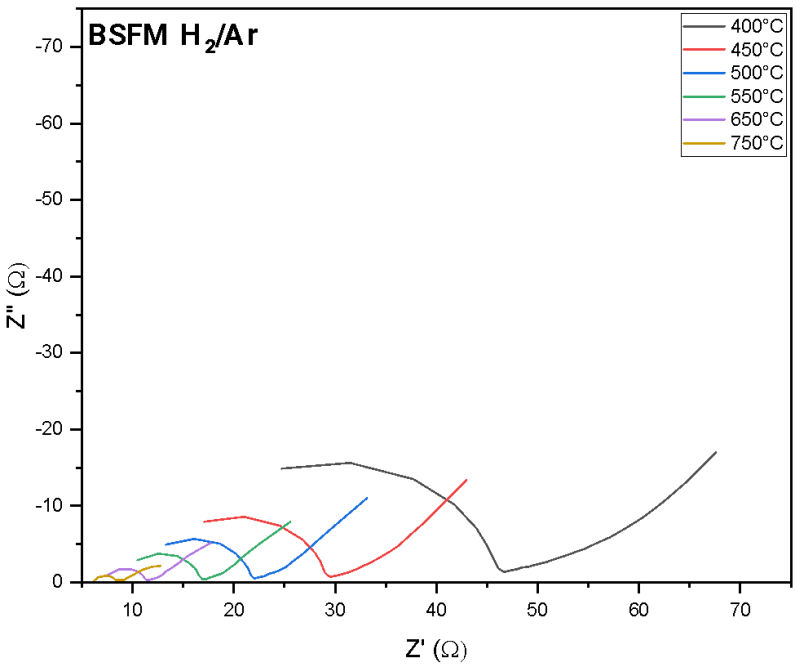

Figure 4-13: Nyquist plot for BSFM using a gas inlet of 10% wet H_2/Ar for different temperatures.

From a comparison with BSCM, it is already clear that the values at T higher than 650°C do not differ as much from the ones observed in the lower temperature range. Furthermore, it is noticeable that the values on the X-axis, corresponding to the real part of impedance, are considerably lower than those pertaining to BSCM. To analyse the EIS spectra, the fitting circuit is the one shown earlier in the *Figure 4-8*. The first process occurring at frequencies of 10^5 Hz exhibits a capacitance of 10^{-8} F, and it can be associated to phenomena happening at the electrode surface. The second process, at lower frequencies, in the order of kHz, has an associated capacitance of 10^4 F. Similar to BSCM, this can be attributed to electrochemical reactions, such as hydrogen oxidation. Lastly, at lower frequencies, the EIS reveals a process describable by semi-finite gas diffusion, fitted with the Warburg Element. [10]

Examining the EIS spectra generated using ammonia as fuel, it can be seen that they exhibit identical processes at the same frequencies as those just discussed for H_2. The Nyquist plot for the EIS data obtained at with NH_3 will be presented in *Figure 4-14*:

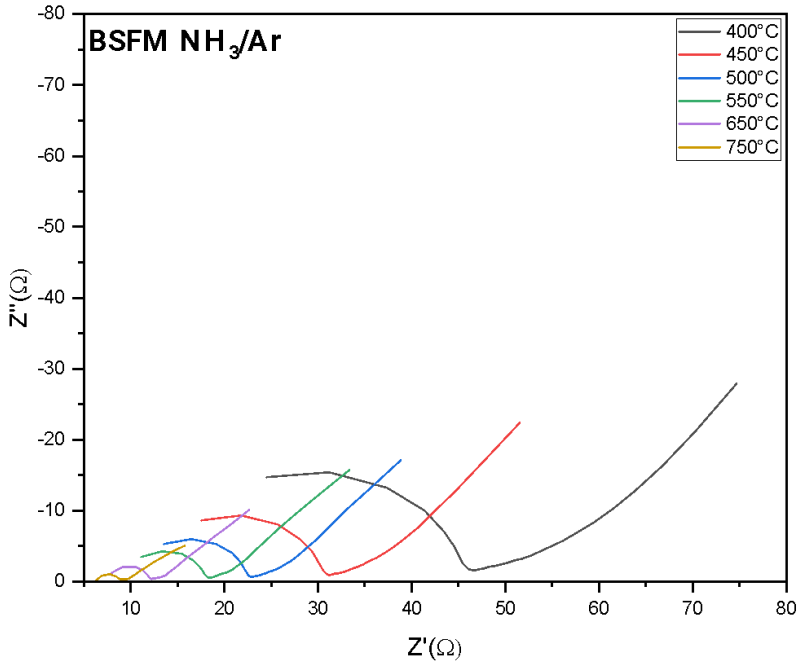

Figure 4-14: Nyquist plot for BSFM using a gas inlet of 10% wet NH_3/Ar for different temperatures.

As mentioned, the cell fuelled with ammonia again exhibits behaviour very similar to that observed when fuelled with hydrogen. The primary distinction between the two fuels lies in slightly higher ASR values, as indicated in *Table 4-2*. Nevertheless, it can be asserted that BSFM could indeed be a suitable candidate as an anodic component for H-SOFC, given that the resistance values for H_2, even at lower temperatures, are quite favourable. Furthermore, it can be affirmed that BSFM operates efficiently even when transitioning to ammonia as a fuel, rendering it a suitable material as an anode for H-rSOC.

Finally, BSFM has been examined as a potential candidate to use as a cathode in H-SOEC for ammonia production. For this reason, the material has been tested in 100% dry N_2 100 sccm in the temperature range of 400-750°C. As shown in *Figure 4-15*, unlike the behaviour observed in BSCM, there is no significant difference in the material's response in nitrogen at higher temperatures. The primary variance in behaviour occurs between 400°C and 450°C, but for temperatures exceeding this value, the resistance values indicate that the electrode indeed functions appropriately.

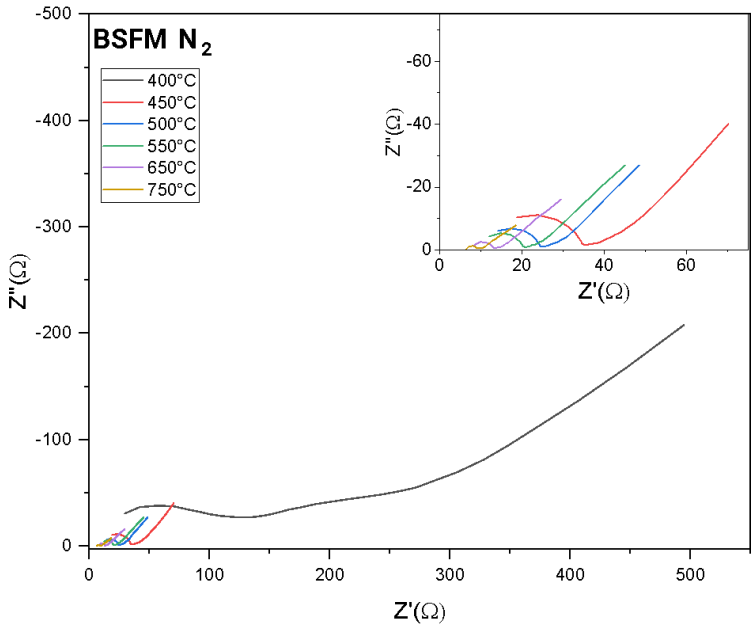

Figure 4-15: Nyquist plot for BSFM using a gas inlet of 100% dry N_2 for different temperatures.

As done previously, the overall Area Specific Resistance (ASR) has been computed for all the three fuels at each temperature, and the findings are summarized in *Table 4-2*. As for BSCM, the ASR values for all considered fuels exhibit a decrease with rising temperature, indicating that the ongoing processes are thermally activated. Additionally, the ASR values obtained

with ammonia, when compared to those obtained with hydrogen, are slightly higher.

Temperature [°C]	**750**	**650**	**550**	**500**	**450**	**400**
ASR [$\Omega \cdot cm^2$] 10% wet H_2/Ar	2.22	3.63	6.49	8.17	11.73	23.78
ASR [$\Omega \cdot cm^2$] 10% wet NH_3/Ar	2.46	3.88	6.78	8.85	13.90	24.53
ASR [$\Omega \cdot cm^2$] 100% dry N_2/Ar	2.39	4.19	9.87	13.60	23.86	192.32

Table 4-2 ASR calculations for each fuel at each temperature.

In contrary to BSCM, however, not just the ASR values obtained at temperatures higher than 650°C hold acceptable significance. In fact, the values obtained in all the temperature range make BSFM a suitable material at the anodic side for H-SOC. Moreover, the result with higher significance is the one obtained fluxing nitrogen at 100sccm as fuel. The resistance value is a very good one even for the lower temperatures and consequently, it has been concluded that this material is a suitable for ammonia synthesis. For this reason, it has been decided that in the test shown in the next paragraph for ammonia production, only the complete cell made by BSFM is going to be tested.

Using the Arrhenius plot, the activation energy for all the processes contributing to the polarization resistance has been computed and is presented in *Figure 4-16* and summarized *in Table 4-3*:

BSCF	*Ea (eV) 10% H_2/Ar*	0.42 eV
	Ea (eV) 10% NH_3/Ar	0.43 eV
	Ea (eV) 100% N_2	0.51 eV

Table 4-3 Activation energy for polarization resistance contributing processes.

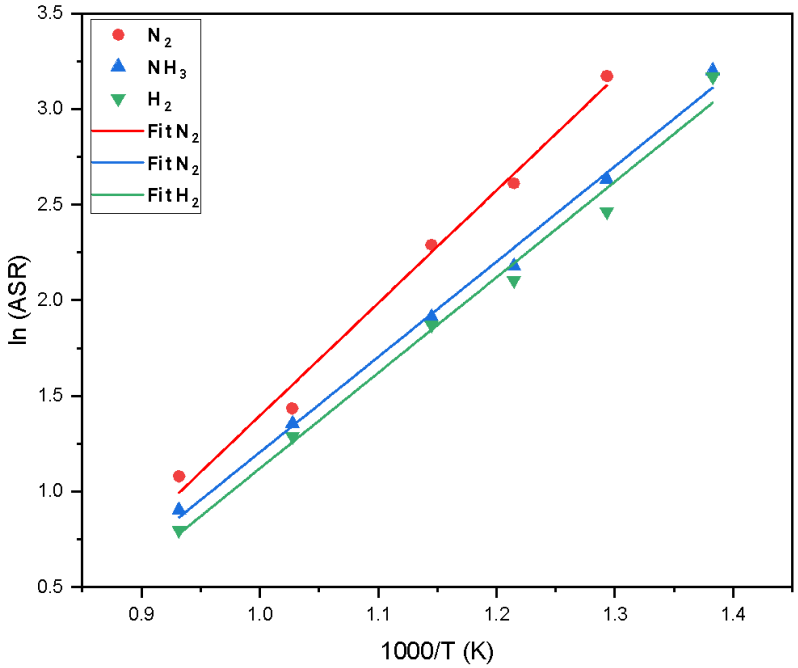

Figure 4-16: Arrhenius Plot ln (ASR) vs 1000/T for the three different gases used.

The activation energy obtained with hydrogen is essentially the same as the one acquired with ammonia, while the activation energy for nitrogen is higher than both. The obtained activation energy values align with those reported in the literature for protonic conductive devices (E_a = 0.4-0.5 eV).[11,12]

4.4 Complete Cell Ammonia Synthesis

Considering the tests made in the symmetrical chamber, the crafting preparations and effective analysis of ammonia synthesis have been made for BSFM. The planar button cell structure remains the same, because with the anodic capabilities esteemed in symmetric mode the cell can be considered reversible and the effective ammonia synthesis can be tested and revealed through gas chromatography. The former analysis has been

carried out with *Agilent 990 MicroGC* with Ar / He carrier, with a sampling of 20 s and sampling injections of 150 ms.

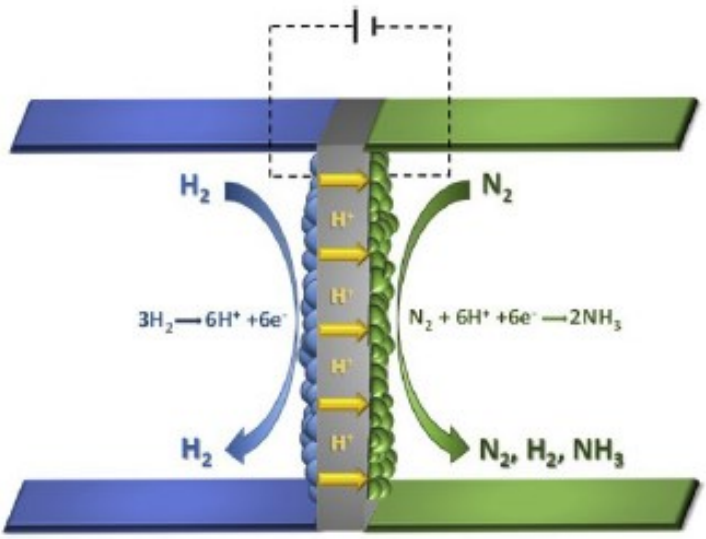

Figure 4-17 Schematic representation of the complete cell process researched.

The external voltage applied to provide electrical potential for protonic ion mobility applied is 1.7 V over the Open Circuit Voltage (OCV) value, choice based on reported research data.[13–15] No other voltage variation has been made during the ammonia synthesis process, since the NH_3 formation is considered a heterogeneous catalytical reaction that occurs on the cathode surface of the cell and depends on the suitable exposed area for nitrogen adsorption.[14]

The rate of ammonia formation r_{NH3} (mol cm^{-2} s^{-1}) was calculated converting the measured NH_3 to moles per second per unit area of the electrodes (electrode's active area = 1,12 cm^2). The rate of ammonia formation was evaluated using the following equation:[14]

$$r_{NH_3} = [NH_3] \cdot \left[\frac{V}{tAM}\right]$$

(4-14)

With [NH_3] the concentration measured through *MicroGC* analysis, *V* is the total sampling volume of the gas inlet, *t* is the sampling time in seconds, *A* is the area of the electrode in cm^2 and *M* is the molecular weight of NH_3. The ammonia formation rate values are reported in *Table 4-4*.

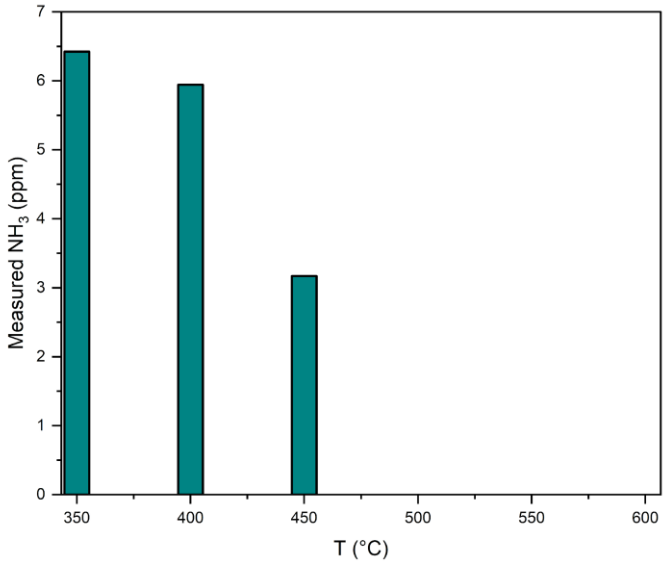

(4-15) Measured ammonia ppm through gas chromatography.

T (°C)	350	400	450
rNH3 (mol cm-2 s-1)	$1.79 \cdot 10^{-9}$	$1.66 \cdot 10^{-9}$	$8.84 \cdot 10^{-10}$

Table 4-4 Ammonia formations rate at low temperatures.

The ammonia formation rates are in the same order of magnitude of the ones reported in literature[13], with a max obtained at atmospheric pressure and at a temperature of 350°C with a value of $1.79x10^{-9}$ mol cm^{-2} s^{-1}. At temperature higher than 500°C no ammonia formation has been observed; however, it is necessary to point out that the instrumentation is in its sensibility limit for values close to the ppm. Therefore, it is not certain that there is no ammonia synthesised at those temperatures, most likely the production is so low that it can not be detected by the Micro-GC.

Along with the ammonia production rate, the current density of the cell has been measured in the temperature range of 350-550°C. The results are shown in the following *Figure 4-18*:

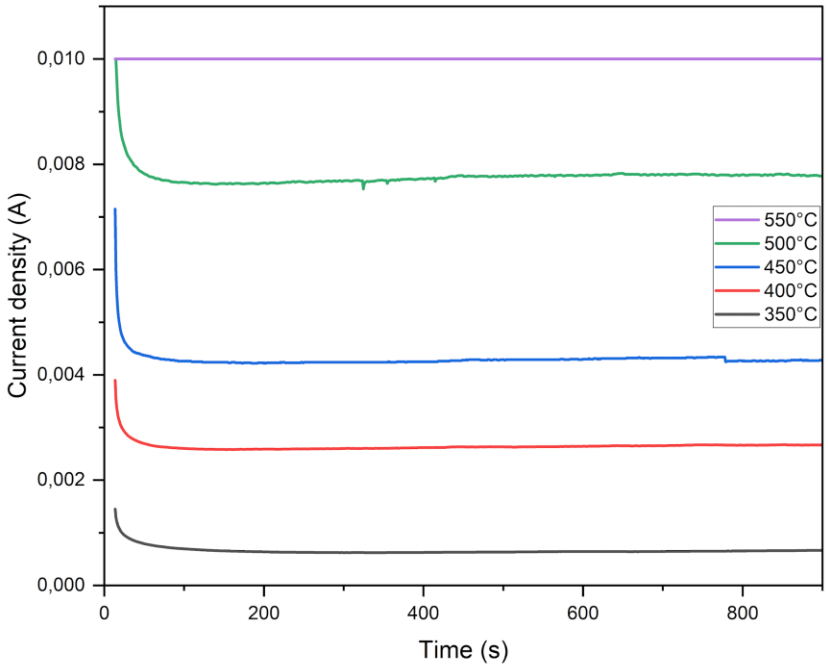

Figure 4-18 The relationship of current density as a function of NH3 formation duration under an applied voltage of 1.7V at different temperatures.

At 550°C (purple line in *Figure 4-18*) the current density is saturated at 10 mA cm^{-2} due to the BCY10 electrolyte resistance and the limited supply of protons produced at the anodic side.

The Faraday efficiency (FE) with an applied potential of 1.7V as a has been calculated for each temperature considered through the following equation:

$$Faraday\ efficiency\ (\%) = \frac{3F \times r_{NH_3}}{I} \tag{4-16}$$

Here, r_{NH_3} represents the rate of ammonia formation, I is the corresponding current density of the applied voltage, and F is the Faraday constant. In the following *Table 4-5* the NH_3 Faraday Efficiency is reported:

T (°C)	**350**	**400**	**450**
NH_3 Faraday Efficiency (%)	0.91	0.17	0.06

Table 4-5 Calculated percentage Faraday efficiency of the Electrochemical process.

The Faraday Efficiency is in accordance with literature data using a ceramic electrolyte.[16] The low value, below 1%, can be attributed to the fact that most of the protons are converted back into hydrogen rather than reacting with nitrogen to produce ammonia.[17]

To sum up, BSFM allowed the production of ammonia at the temperatures from 350 to 450°C; above those temperatures, no ammonia formation has been detected, however it is not possible to exclude its synthesis since at low ppm the instrumentation is at its revelation limits. In fact, the current density measurements suggest that the SOEC device is actually working even at 500 and 550°C.

4.5 References

(1) Pergolesi, D.; Fabbri, E.; D'Epifanio, A.; Di Bartolomeo, E.; Tebano, A.; Sanna, S.; Licoccia, S.; Balestrino, G.; Traversa, E. High Proton Conduction in Grain-Boundary-Free Yttrium-Doped Barium Zirconate Films Grown by Pulsed Laser Deposition. *Nat. Mater.* **2010**, *9* (10), 846–852. https://doi.org/10.1038/nmat2837.

(2) Boaro, M.; Vohs, J. M.; Gorte, R. J. Synthesis of Highly Porous Yttria-Stabilized Zirconia by Tape-Casting Methods. *J. Am. Ceram. Soc.* **2003**, *86* (3), 395–400. https://doi.org/10.1111/j.1151-2916.2003.tb03311.x.

(3) *Basics of EIS: Electrochemical Research-Impedance Gamry Instruments*. https://www.gamry.com/application-notes/EIS/basics-of-electrochemical-impedance-spectroscopy/.

(4) Han, W.; Fang, F. Investigation of Electrochemical Properties of Electropolishing Co–Cr Dental Alloy. *J. Appl. Electrochem.* **2020**, *50* (3), 367–381. https://doi.org/10.1007/s10800-019-01390-3.

(5) Holm, S.; Holm, T.; Martinsen, Ø. G. Simple Circuit Equivalents for the Constant Phase Element. *PLoS ONE* **2021**, *16* (3), e0248786. https://doi.org/10.1371/journal.pone.0248786.

(6) Irvine, J. T. S.; Sinclair, D. C.; West, A. R. Electroceramics: Characterization by Impedance Spectroscopy. *Adv. Mater.* **1990**, *2* (3), 132–138. https://doi.org/10.1002/adma.19900020304.

(7) Sumi, H.; Shimada, H.; Yamaguchi, Y.; Mizutani, Y.; Okuyama, Y.; Amezawa, K. Comparison of Electrochemical Impedance Spectra for Electrolyte-Supported Solid Oxide Fuel Cells (SOFCs) and Protonic Ceramic Fuel Cells (PCFCs). *Sci. Rep.* **2021**, *11* (1), 10622. https://doi.org/10.1038/s41598-021-90211-9.

(8) Wuillemin, Z.; Antonetti, Y.; Beetschen, C.; Millioud, O.; Ceschini, S.; Madi, H.; Van herle, J. Local Activation and Degradation of Electrochemical Processes in a SOFC. *ECS Trans.* **2013**, *57* (1), 561–570. https://doi.org/10.1149/05701.0561ecst.

(9) Metrohm; Autolab. EIS Data Fitting - How to Obtain Good Starting Values of Equivalent Circuit Elements, 2019.

(10) William, J. J.; Balakrishnan, S.; Murugesan, M.; Gopalan, M.; Britten, A. J.; Mkandawire, M. Mesoporous β-Ag_2MoO_4 Nanopotatoes as Supercapacitor Electrodes. *Mater. Adv.* **2022**, *3* (22), 8288–8297. https://doi.org/10.1039/D2MA00708H.

(11) Basbus, J.; Arce, M.; Troiani, H.; Su, Q.; Wang, H.; Caneiro, A.; Mogni, L. Study of $BaCe_{0.4}Zr_{0.4}Y_{0.2}O_{3-\delta}$/$BaCe_{0.8}Pr_{0.2}O_{3-\delta}$ (BCZY/BCP) Bilayer Membrane for Protonic Conductor Solid Oxide Fuel Cells (PC-SOFC). *Int. J. Hydrog. Energy* **2020**, *45* (8), 5481–5490. https://doi.org/10.1016/j.ijhydene.2019.06.164.

(12) Baral, A. K.; Choi, S.; Kim, B. K.; Lee, J.-H. Processing and Characterizations of a Novel Proton-Conducting $BaCe_{0.35}Zr_{0.50}Y_{0.15}O_{3-\delta}$ Electrolyte and Its Nickel-Based Anode Composite for Anode-Supported IT-SOFC. *Mater. Renew. Sustain. Energy* **2014**, *3* (4), 35. https://doi.org/10.1007/s40243-014-0035-4.

(13) Li, R.; Liu, X.; He, G.; Hu, P.; Zhen, Q.; Liu, J. L.; Bashir, S. Green Catalytic Synthesis of Ammonia Using Solid Oxide Electrolysis Cells Composed of Multicomponent Materials. *Catal. Today* **2021**, *374*, 102–116. https://doi.org/10.1016/j.cattod.2021.03.029.

(14) Goldstein, V.; Rath, M. K.; Kossenko, A.; Litvak, N.; Kalashnikov, A.; Zinigrad, M. Solid Oxide Fuel Cells for Ammonia Synthesis and Energy

Conversion. *Sustain. Energy Fuels* **2022**, *6* (20), 4706–4715. https://doi.org/10.1039/D2SE00954D.

(15) Lan, R.; Alkhazmi, K. A.; Amar, I. A.; Tao, S. Synthesis of Ammonia Directly from Wet Air at Intermediate Temperature. *Appl. Catal. B Environ.* **2014**, *152–153*, 212–217. https://doi.org/10.1016/j.apcatb.2014.01.037.

(16) Yun, D. S.; Joo, J. H.; Yu, J. H.; Yoon, H. C.; Kim, J.-N.; Yoo, C.-Y. Electrochemical Ammonia Synthesis from Steam and Nitrogen Using Proton Conducting Yttrium Doped Barium Zirconate Electrolyte with Silver, Platinum, and Lanthanum Strontium Cobalt Ferrite Electrocatalyst. *J. Power Sources* **2015**, *284*, 245–251. https://doi.org/10.1016/j.jpowsour.2015.03.002.

(17) Howalt, J. G.; Bligaard, T.; Rossmeisl, J.; Vegge, T. DFT Based Study of Transition Metal Nano-Clusters for Electrochemical NH_3 Production. *Phys. Chem. Chem. Phys.* **2013**, *15* (20), 7785–7795. https://doi.org/10.1039/C3CP44641G.

5. CONCLUSIONS

In this work has been successfully synthetised, characterised, manufactured and tested a material capable of synthetising ammonia through the nitrogen reduction reaction (NRR) in an electrochemical pathway with a SOEC device.

This project has been carried out following the nowadays key challenges that needs to be addressed in realizing the "green ammonia synthesis". Even though the use of ammonia as potential fuel or hydrogen carrier is still receiving limited attentions compared to e.g., the complex metal hydrides or other direct hydrogen storage methods, its technology seems to be significantly closer to the market. Its use has been compared with other conventional fuels, liquefied petroleum gas as well as hydrogen from the points of energy storage density per unit of volume and of mass, costs and facilities in transportation, reporting outstanding data considering the carbon-free composition of these energy carrier.

Moreover, the electrochemical production of NH_3 is gaining more and more interest, to provide a completely carbon free footprint to the process, allowing a more decentralised, sustainable ammonia supply on the basis of photo-voltaic cells or wind power. The development of more advanced catalysts is the constant theme in this field, reason why two critical-raw free materials have been adopted to build a proton conducting cell, to overcome any possible drawbacks of nitrogen oxides pollutants by-products of the synthesis process (possible with anion conducting based devices). The proton conduction, active with a lower potential demand, was achieved in a solid oxide device to adopt the suitability to work in a reversible way and

with low temperatures range, favouring the thermodynamic of the ammonia synthesis process.

In order to catalyse the former process, the materials must be able to adsorb nitrogen and promote its reduction in an associative pathway, rather than the far more energy demanding dissociative one, used in the Haber-Bosch Process. This peculiarity has been researched and achieved following the nature cluster structure of the FeMo cofactor of the nitrogenase enzyme, channeling the choice of these two metals into an ordered double perovskite structure, to provide a homogeneous distribution of catalytic centres in the device and showing promising characteristic as SOEC component. The A metals components of the $AA'BB'O_{6-\delta}$ perovskite must produce a structure similar to the electrolyte one (BCY10) and provide good conduction properties for the electrode material designed. All these considerations led to the research and application of $BaSrFe_{1.5}Mo_{0.5}O_{6-\delta}$ (BSFM) and $BaSrCo_{0.2}Mo_{1.8}O_{6-\delta}$ (BSCM).

These perovskites have been synthesized successfully and characterized mainly through X-Ray diffraction spectrometry, researching and defining stability at various ambient atmospheres, the possibility to recover the synthetised structures simply by temperature treatment, and their compatibility with the proton conducting electrolyte of choice. To further comprehend reducing atmosphere behaviours, being hydrogen the fuel for the synthesis process, Temperature Programmed Reduction analysis have been executed and the powders morphology, SEM acquired, are compared with literature showing far better porosity, for this reason allowing the fuel to flow deeper in the catalyst.

The correct compositions of the synthesized electrodes have been determined by EDX quantitative measurements, and the surface atomic

composition by X-Ray Photoelectron Spectroscopy. The catalytic activity of the two powders was tested with a temperature increasing H_2 30% / N_2 70% atmosphere treatment and then the surface of the samples pre and postreaction has been measured again by XPS, which displayed really interesting signals from the BSFM powder, showing ammonia-like nitrogen on the N1s peak position.

Both materials where finally used to produce a planar button solid oxide cell device, crafted by tape casting with a mixed ink, analysed both in Fuel and Electrolysis mode to test reversibility. The first fuel cell mode capability has been tested with the Electrochemical Impedance Spectroscopy (EIS) investigating the performances at different temperatures, with different inlet fuels in a symmetrical chamber setup. BSCM showed acceptable ASR (area specific resistance) only at higher temperatures, not suitable for ammonia synthesis, instead BSFM showed very promising results both at high and low temperatures, showing suitable anodic performances in all the temperature range (400-750°C) with a maximum ASR value of 23.78 Ω cm^2 at 400°C, and an activation energy of the process of 0.4 eV, considerably good results literature compared with same purpose materials.[1] With these results a complete cell chamber setup was manufactured and consequent tests performed.

The BSFM material correctly achieved the researched purposes, allowing a maximum measurement of an ammonia formation rate of $1.79 \cdot 10^{-9}$ mol cm^{-2} s^{-1} at 350 °C, so in the same order of magnitude of the ones reported in literature, with the highest values recorded for SOEC ammonia synthesis approximately of $8 \cdot 10^{-9}$ mol cm^{-2} s^{-1} at 400°C with comparable Faraday efficiency.[1–7]Despite the obtained results, the possible advantages

and researches on this materials are not yet to be defined as closed, neither for BSCM nor BSFM.

5.1 Future Perspectives

Both materials showed the capability to work as anode in SOFC device. The performances and results of BSCM can be further enhanced, probably with optimizations such as a surface pre-treatment to prepare the device to work in its optimal condition as well as the electrode/electrolyte interface optimization; a different planar cell configuration (electrode supported, as an example) could also be a useful strategy.

These improvements can also be applied to BSFM. However, in alignment with the objective of this study, there are additional performances, more challengingly obtainable, shown by this material that may be enhanced. Since it showed particularly good performances as a catalyst for ammonia synthesis, this peculiarity should be further researched. As shown by XPS analysis, the probable adsorption active sites (iron based) on the surface are rather low: exsolutions methodologies or impregnation coating can be tested to increase the amount of surface iron and thus improve the adsorption, with the aim of limiting one of the rate limiting steps.

More studies on how the involved mechanisms, can also improve the research on this catalytic material, for example in situ characterization of the device can outline possible improvements or can help building up more valid theoretical models and deeper understanding of the reaction pathways.

Finally, another sensitive field of development is on the device working condition and designs. Besides what already outlined for BSCM greater advancements can be performed optimising the gas flows injected to the catalyst and even more optimising the ammonia-containing gas extraction from the chamber reducing the possibility NH_3 contamination on adsorption sites. More effective low temperatures proton conducting electrolytes will also improve the working condition of the device itself and the performance evaluation urgently requires developing more selective, precise, and in situ method for ammonia determination.

To sum up, production of green ammonia via electrochemical routes offers a pathway with great potential to achieve carbon neutrality for 2050, and the research field of proton conduction, moreover of SOEC ammonia synthesis, leave open significant research opportunities in terms of material development (electrode/electrolyte/catalyst), optimization of device designs, geometries and occurring phenomena theories, enabling a wide range of potential applications to safeguard our planet.

5.2 References

(1) Yun, D. S.; Joo, J. H.; Yu, J. H.; Yoon, H. C.; Kim, J.-N.; Yoo, C.-Y. Electrochemical Ammonia Synthesis from Steam and Nitrogen Using Proton Conducting Yttrium Doped Barium Zirconate Electrolyte with Silver, Platinum, and Lanthanum Strontium Cobalt Ferrite Electrocatalyst. *J. Power Sources* **2015**, *284*, 245–251. https://doi.org/10.1016/j.jpowsour.2015.03.002.

(2) Wang, B.; Li, T.; Gong, F.; Othman, M. H. D.; Xiao, R. Ammonia as a Green Energy Carrier: Electrochemical Synthesis and Direct Ammonia Fuel Cell - a Comprehensive Review. *Fuel Process. Technol.* **2022**, *235*, 107380. https://doi.org/10.1016/j.fuproc.2022.107380.

(3) Wolf, S. E.; Winterhalder, F. E.; Vibhu, V.; De Haart, L. G. J. (Bert); Guillon, O.; Eichel, R.-A.; Menzler, N. H. Solid Oxide Electrolysis Cells – Current Material Development and Industrial Application. *J. Mater. Chem. A* **2023**, *11* (34), 17977–18028. https://doi.org/10.1039/D3TA02161K.

(4) Vasileiou, E.; Kyriakou, V.; Garagounis, I.; Vourros, A.; Manerbino, A.; Coors, W. G.; Stoukides, M. Electrochemical Enhancement of Ammonia Synthesis in a $BaZr_{0.7}Ce_{0.2}Y_{0.1}O_{2.9}$ Solid Electrolyte Cell. *Solid State Ion.* **2016**, *288*, 357–362. https://doi.org/10.1016/j.ssi.2015.12.022.

(5) Lan, R.; Alkhazmi, K. A.; Amar, I. A.; Tao, S. Synthesis of Ammonia Directly from Wet Air at Intermediate Temperature. *Appl. Catal. B Environ.* **2014**, *152–153*, 212–217. https://doi.org/10.1016/j.apcatb.2014.01.037.

(6) Li, R.; Liu, X.; He, G.; Hu, P.; Zhen, Q.; Liu, J. L.; Bashir, S. Green Catalytic Synthesis of Ammonia Using Solid Oxide Electrolysis Cells

Composed of Multicomponent Materials. *Catal. Today* **2021**, *374*, 102–116. https://doi.org/10.1016/j.cattod.2021.03.029.

(7) Goldstein, V.; Rath, M. K.; Kossenko, A.; Litvak, N.; Kalashnikov, A.; Zinigrad, M. Solid Oxide Fuel Cells for Ammonia Synthesis and Energy Conversion. *Sustain. Energy Fuels* **2022**, *6* (20), 4706–4715. https://doi.org/10.1039/D2SE00954D.

Acknowledgments

Arrivato alla fine di questo lungo percorso ci tengo a ringraziare alcune delle persone che mi sono state a fianco, specialmente in questo ultimo periodo. Prima tra tutti la professoressa Antonella Glisenti per avermi accolto, guidato e incoraggiato durante tutto il progetto di tesi, aiutandomi, essendo paziente e disponibile, in qualsiasi momento con il sorriso, per chiarimenti, correzioni e confronti.

Vorrei ringraziare anche i miei genitori e famiglia, sia di sangue che estesa, per avermi supportato, aiutandomi qualsiasi fosse la mia richiesta senza chiedere nulla in cambio, ma soprattutto per aver avuto piena fiducia in me, nonostante non fosse sempre così facile.

Un saluto e ringraziamento anche ai ragazzi e ragazze del gruppo IMPACT con i quali ho condiviso questi mesi tra saluti, risate, scherzi e ogni tanto anche lavoro. In particolar modo un grazie a Jonathan per i preziosi insegnamenti di vita accademica e non.

Un saluto con poco ringraziamento va anche agli amici di una vita, i formalmente detti gajardi e le amiche formalmente dette gajarde per avermi aiutato a non studiare anche quando serviva farlo, caratteristica per la quale ringrazio dal cuore anche Jimmy che, nonostante la distanza, si prodiga sempre affinché ciò avvenga.

Un ringraziamento speciale va infine a Pietro, ormai il quarto fratello, che qualsiasi fosse il motivo per divertirsi o il problema da risolvere lui c'è sempre stato, quarantena o meno, felici o meno. Grazie veramente. Spero che tu abbia sempre un Jonny a supervisorarti.